

Dissertation zur Erlangung des Doktorgrades
der Fakultät für Chemie und Pharmazie
der Ludwig-Maximilians-Universität München

Hydrothermal synthesis of layered iron-chalcogenide superconductors and related compounds

Ursula Elisabeth Pachmayr

aus

München, Deutschland

2017

Erklärung

Diese Dissertation wurde im Sinne von § 7 der Promotionsordnung vom 28. November 2011 von Herrn Prof. Dr. Dirk Johrendt betreut.

Eidesstattliche Versicherung

Diese Dissertation wurde eigenständig und ohne unerlaubte Hilfe erarbeitet.

München,

Ursula Pachmayr

Dissertation eingereicht am

03.03.2017

1. Gutachter:

Prof. Dr. Dirk Johrendt

2. Gutachter:

Prof. Dr. Wolfgang Schnick

Mündliche Prüfung am

06.04.2017

Danksagung

Mein besonderer Dank gilt Herrn Prof. Dr. Dirk Johrendt für die Möglichkeit meine Doktorarbeit in seiner Arbeitsgruppe anzufertigen. Ohne die Freiheit bei der Bearbeitung des Themas, die konstruktiven Diskussionen und stets offenen Türen wäre die Arbeit in dieser Weise nicht möglich gewesen.

Herrn Prof. Dr. Wolfgang Schnick danke ich herzlich für die Übernahme des Koreferats.

Darüberhinaus danke ich Herrn Prof. Dr. Oliver Oeckler, Herrn Prof. Dr. Konstantin Karaghiosoff, Herrn Prof. Dr. Achim Hartschuh und Herrn Prof. Dr. Hans-Christian Böttcher dafür, dass sie sich als Prüfer für mein Rigorosum zur Verfügung gestellt haben.

Danke auch an alle aktuellen und ehemaligen Arbeitskreismitglieder, Frau Beatrix Fischer, Herrn Rainer Frankovsky, Frau Gina Friederichs, Herrn Arthur Haffner, Frau Franziska Hummel, Frau Catrin Löhnert, Herrn Fabian Nitsche, Herrn Simon Peschke, Herrn Roman Pobel, Herrn Tobias Rackl, Herrn Rudolf Schönmann, Frau Juliane Stahl, Frau Christine Stürzer, Herrn Tobias Stürzer und Herrn Erwin Wiesenmayer. Vielen Dank für die Hilfsbereitschaft, zahlreichen Messungen, interessanten Diskussionen und das gute Arbeitsklima.

Danke Fabian für die 1000 Wörter am Tag und deine ansteckende Begeisterung, Simon und Roman für die zahlreichen trockeneisbeladenen Fahrten nach Garching, danke Juliane für die gute Autoklaven-Partnerschaft und danke Catrin für deine unterhaltsamen Bergtour-Berichte und die Hilfe bei allen organisatorischen Dingen.

Vielen Dank auch allen Kollegen der Arbeitskreise Schnick, Lotsch, Hoch und Oeckler für die gute Zusammenarbeit.

Für ihre tolle, engagierte Arbeit möchte ich mich bei meinen Praktikanten Herrn Patrick Hirschle, Frau Carolin Rehermann, Frau Natalie Fehn, Frau Eugenia Elzer und Frau Christina Geiger ganz herzlich bedanken.

Herrn Sirko Kamusella, Rajib Sarkar und Herrn Prof. Dr. Hans-Henning Klauss von der TU Dresden ein Dankeschön für die zahlreichen Mößbauer- bzw. NMR-Messungen. Ebenso danke ich Herrn Stefan Holenstein und Herrn Dr. Hubertus Luetkens vom PSI für die Durchführung und Auswertung der μ SR-Messungen und Herrn PD Dr. Rudi Hackl sowie Herrn Dr. Matthias Opel vom WMI für die Möglichkeit und Unterstützung bei den

feldabhängigen Leitfähigkeitsmessungen. Herrn Jonathan Wright vom ESRF danke ich für die Unterstützung bei den Synchrotron-Messungen und Herrn Prof. Dr. Oliver Oeckler für die Hilfe bei kristallographischen Problemen jeder Art. Ein herzliches Dankeschön auch an Herrn Stefan Datz für die diversen Raman-Messungen und an Herrn Lukas Neudert für die Untersuchungen am TEM.

Meiner Familie, im Besonderen meinen Eltern, Großeltern und meinen Geschwistern danke ich von Herzen, dass ihr mich immer unterstützt und für mich da seid.

Danke Simon für deine Geduld, deine Unterstützung und die schöne gemeinsame Zeit.

Das Schönste, was wir erleben können,
ist das Geheimnisvolle.

(Albert Einstein)

Table of Contents

| | | |
|-------|-----------------------------------------------------------------------------------------------------------------|----|
| 1 | Introduction | 1 |
| 2 | Methods..... | 8 |
| 2.1 | Synthetic methods..... | 8 |
| 2.1.1 | Starting materials..... | 8 |
| 2.1.2 | Equipment and conditions | 8 |
| 2.2 | Analytical methods | 10 |
| 2.3 | References | 13 |
| 3 | Hydrothermally prepared FeX (X = Se, S) | 14 |
| 3.1 | Influence of synthesis parameters on the hydrothermal synthesis of FeSe... 14 | |
| 3.1.1 | Introduction | 14 |
| 3.1.2 | Experimental details | 15 |
| 3.1.3 | Results and discussion..... | 16 |
| 3.1.4 | Conclusion..... | 23 |
| 3.1.5 | References..... | 23 |
| 3.2 | Structural transition and superconductivity in hydrothermally synthesized FeX (X = S, Se)..... | 25 |
| 3.2.1 | Introduction | 25 |
| 3.2.2 | Experimental details | 26 |
| 3.2.3 | Results and discussion..... | 27 |
| 3.2.4 | Conclusion..... | 33 |
| 3.2.5 | References..... | 33 |
| 3.3 | The solid-solution FeSe _{1-x} S _x prepared via hydrothermal synthesis | 36 |
| 3.3.1 | Introduction | 36 |
| 3.3.2 | Experimental details | 36 |
| 3.3.3 | Results and discussion..... | 37 |
| 3.3.4 | Conclusion..... | 42 |
| 3.3.5 | References..... | 42 |
| 4 | The layered lithium iron chalcogenide hydroxide [(Li _{0.8} Fe _{0.2})OH]FeX (X = Se, S) | 44 |
| 4.1 | Coexistence of 3d-ferromagnetism and superconductivity in [(Li _{0.8} Fe _{0.2})OH]FeSe..... | 44 |
| 4.1.1 | Introduction | 45 |
| 4.1.2 | Experimental details | 46 |
| 4.1.3 | Results and discussion..... | 46 |
| 4.1.4 | Conclusion..... | 54 |
| 4.1.5 | References..... | 54 |
| 4.2 | Upper critical field of [(Li _{0.8} Fe _{0.2})OH]FeSe | 57 |
| 4.2.1 | Introduction | 57 |
| 4.2.2 | Experimental details | 57 |
| 4.2.3 | Results and discussion..... | 58 |
| 4.2.4 | Conclusion..... | 61 |

| | | |
|-------|----------------------------------------------------------------------------------------------------------------------------------------------------------------------|-----|
| 4.2.5 | References..... | 61 |
| 4.3 | Investigations on the real structure of $[(\text{Li}_{0.8}\text{Fe}_{0.2})\text{OH}]\text{FeX}$ ($X = \text{Se}, \text{S}$)..... | 63 |
| 4.3.1 | Introduction | 63 |
| 4.3.2 | Experimental details..... | 65 |
| 4.3.3 | Results and discussion..... | 65 |
| 4.3.4 | Conclusion..... | 71 |
| 4.3.5 | References..... | 71 |
| 4.4 | Crystal growing of large $[(\text{Li}_{0.8}\text{Fe}_{0.2})\text{OH}]\text{FeSe}$ crystals | 73 |
| 4.4.1 | Introduction | 73 |
| 4.4.2 | Experimental details..... | 74 |
| 4.4.3 | Results and discussion..... | 75 |
| 4.4.4 | Conclusion..... | 81 |
| 4.4.5 | References..... | 81 |
| 4.5 | $[(\text{Li}_{0.8}\text{Fe}_{0.2})\text{OH}]\text{FeS}$ and the ferromagnetic superconductors | |
| | $[(\text{Li}_{0.8}\text{Fe}_{0.2})\text{OH}]\text{Fe}(\text{S}_{1-x}\text{Se}_x)$ | 83 |
| 4.5.1 | Introduction | 83 |
| 4.5.2 | Experimental details..... | 84 |
| 4.5.3 | Results and discussion..... | 84 |
| 4.5.4 | Conclusion..... | 92 |
| 4.5.5 | References..... | 92 |
| 4.6 | Effect of cobalt substitution in the ferromagnetic superconductor | |
| | $[(\text{Li}_{0.8}\text{Fe}_{0.2})\text{OH}]\text{FeSe}$ | 94 |
| 4.6.1 | Introduction | 95 |
| 4.6.2 | Experimental details..... | 95 |
| 4.6.3 | Results and discussion..... | 96 |
| 4.6.4 | Conclusion..... | 98 |
| 4.6.5 | References..... | 99 |
| 5 | Hydrothermal synthesis of $\text{Na}_6(\text{H}_2\text{O})_{18}\text{Fe}_4\text{Se}_8$ and $A_2\text{Fe}_4\text{Se}_6$ ($A = \text{K}, \text{Rb}, \text{Cs}$)..... | 100 |
| 5.1 | Introduction..... | 100 |
| 5.2 | Experimental details | 101 |
| 5.3 | Results and discussion | 101 |
| 5.4 | Conclusion..... | 108 |
| 5.5 | References..... | 109 |
| 6 | Summary..... | 111 |
| 7 | Conclusion..... | 117 |
| 8 | Appendix..... | 119 |
| 8.1 | Crystallographic data of FeS | 119 |
| 8.2 | Supplementary information of $[(\text{Li}_{0.8}\text{Fe}_{0.2})\text{OH}]\text{FeSe}$ | 120 |
| 8.2.1 | Crystallographic data of $[(\text{Li}_{0.8}\text{Fe}_{0.2})\text{OH}]\text{FeSe}$ | 120 |
| 8.2.2 | Mössbauer spectroscopy..... | 121 |
| 8.2.3 | μSR | 122 |
| 8.3 | Crystallographic data of $[(\text{Li}_{0.8}\text{Fe}_{0.2})\text{OH}]\text{FeS}$ | 126 |

| | | |
|------|-------------------------------|-----|
| 9 | Abbreviations..... | 127 |
| 10 | Scientific contributions..... | 131 |
| 10.1 | Publications..... | 131 |
| 10.2 | Conference contributions..... | 134 |
| 11 | Curriculum Vitae | 137 |

1 Introduction

In the modern energy technology, superconducting materials become more and more important as they enable a significant enhancement of efficiency for many facilities and a loss-free transport of electric current. They rank among the greatest challenges of modern solid state research, both concerning the still incomplete understanding of the underlying mechanisms and the technical application. Nevertheless, the application increases steadily especially due to the successful development of superconducting second-generation wires (2G-HTS wires). A superconducting 2G-HTS wire carries about 20 times more electric current without heat generation compared to a copper conductor. Thereby, the energy efficiency for example of electromotors or generators for electricity generation can be considerably improved^[1, 2] and loss-free transport of electric current is possible over long distances.^[3, 4] In our days, a future 10 MW wind generator is expected to be realizable by application of superconducting materials.^[5, 6] Currently, 2G-HTS wires however are still distinctly more expensive than conventional copper conductors. Most commonly they are based on the copper oxide high-temperature superconductor $\text{YBa}_2\text{Cu}_3\text{O}_{7-x}$ which can be cost-effectively cooled by liquid nitrogen owing to the high critical temperature (T_c) of 93 K. However, this advantage is counterbalanced by a large anisotropy of the superconducting properties. Exclusively optimal textured materials in wires or tapes can bear large currents, which is the main reason for the complex and thus expensive production of corresponding copper oxide conductors.

Since 2008, another class of high-temperature superconductors is known.^[7, 8] Iron-arsenides and iron-selenides with layered structures and critical temperatures up to 58 K^[9] have attracted considerable interest and are explored internationally by numerous groups.^[10] In iron-based superconductors, superconductivity arises in quasi two-dimensional layers of edge-sharing $\text{FeAs}_{4/4}$ or $\text{FeSe}_{4/4}$ tetrahedra. Magnetic fluctuations are considered essential for the emergence of superconductivity. Hence, the formation of Cooper pairs is probably based on an unconventional mechanism,^[11] i.e. not (only) on electron-phonon coupling as for conventional metallic superconductors. This applies for the copper oxides as well and presumably is the reason why higher critical temperatures occur in these systems.^[12] Beside this similarity a fundamental difference exists. The superconducting wavefunction in copper oxides has d -symmetry (d -wave) and is thus intrinsically anisotropic. In contrast, isotropic s -symmetry (s -wave) is present in many iron-based superconductors. The d -symmetry is the reason for the strong anisotropy of superconductivity in copper oxides, whereas s -symmetry in iron-based superconductors is responsible for a considerably lower

anisotropy despite the layered structure. Furthermore, superconductivity in iron-based superconductors is highly robust against external magnetic field. First investigations on critical currents in round wires of iron-based superconductors give values up to 0.1 MA/cm² and clearly prove the large potential for applications especially with respect to round superconducting wires.^[13]

The highest critical temperature of 58 K for iron-based superconductors is rather low in comparison to the one of copper oxides. It falls below the boiling point of liquid nitrogen (77 K) and thus requires the more expensive cooling with helium. Therefore it is not surprising that the search for new iron-based superconductors with higher critical temperatures is intensively pursued. However, the crucial factors concerning this purpose are still unclear. What is known is that superconductivity arises in the FeAs/FeSe layers and depends on distinct electronic conditions. In iron-arsenides the layer bears a negative charge ([FeAs]¹⁻), which is compensated by various spacing layers. Examples are LaOFeAs or BaFe₂As₂.^[8, 14] Superconductivity emerges when this charge is enhanced ('electron doping') or lowered ('hole doping') for about 10–20 %. Both can be realized by suitable substitutions, for example the partial exchange of oxygen by fluorine in LaO_{1-x}F_xFeAs (*T_c* up to 26 K)^[8] or of barium by potassium in Ba_{1-x}K_xFe₂As₂ (*T_c* up to 38 K)^[15].

The iron selenide β -FeSe (*anti*-PbO type structure, in the following denoted as FeSe) consists of uncharged FeSe-layers (Fig. 1) and is superconducting below 8 K.^[16] It adopts the simplest crystal structure of any known iron-based superconductor. FeSe has often no ideal 1:1 stoichiometry which leads to a slight charge shifting. This intrinsic doping is discussed as a possible origin for the emergence of superconductivity.^[17-19]

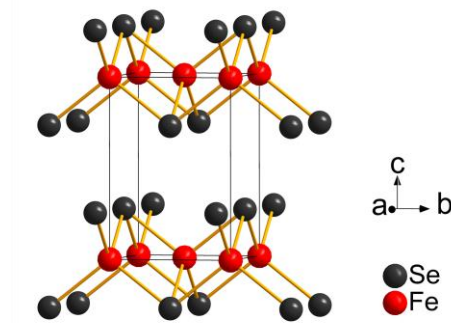


Fig. 1: Crystal structure of FeSe.

It has been shown that FeSe exhibits the potential for much higher critical temperatures. Under high pressure of 9 GPa, T_c increases to 37 K^[20] whereas intercalation of Li-amide for example yields 43 K.^[21] Resistivity measurements on single-layer FeSe films grown on Nb-doped SrTiO₃ (001) surfaces even reveal superconducting transition temperatures as high as 109 K.^[22] This emergence of superconductivity in FeSe layers well above the 77 K necessary for liquid nitrogen cooling illustrates the huge potential of this compound. Furthermore, the relatively weak interactions between the layers should facilitate the incorporation of appropriate interlayers for new superconducting compounds. It seems possible that such an insertion of convenient spacer layers might lead to an increase of T_c , comparable to the one of single-layer FeSe.

For the synthesis of iron-based superconductors, conventional solid-state reactions at high temperatures have been mainly employed so far and already yielded a class of superconducting iron-arsenides. For the modification of FeSe they have been less successful though. The synthesis of superconducting phases with nominal composition $A_x\text{Fe}_{2-y}\text{Se}_2$ ($A = \text{K, Rb, Cs}$) and critical temperatures of up to 45 K can be indeed achieved, however these materials are microscopically phase separated. It is still under discussion which constituent is superconducting. Most indications are that small volume fractions of the superconducting phase $A_x\text{Fe}_2\text{Se}_2$ are coherently intergrown with the stable, non-superconducting main phase $A_2\text{Fe}_4\text{Se}_5$, which shows a superstructure of Fe vacancies.^[23-27]

As only relatively weak van-der-Waals interactions act between the layers, FeSe is also a convenient host for intercalation reactions at low temperatures. It has already been shown that reactions in liquid ammonia are successful and yield compounds like $A_x(\text{NH}_2)_y(\text{NH}_3)_{1-y}\text{Fe}_2\text{Se}_2$ ($A = \text{Li-Cs, Ca-Ba, Eu and Yb}$) or $A_x(\text{NH}_3)_y\text{Fe}_2\text{Se}_2$ with T_c up to 46 K.^[21, 28-31] When pyridine, ethylenediamine, hexamethylenediamine or phenethylamine are used as solvents, the respective compounds $A_x(\text{C}_5\text{H}_5\text{N})_y\text{Fe}_{2-z}\text{Se}_2$ ($A = \text{Li-Rb}$),^[32] $\text{Li}_x(\text{C}_2\text{H}_8\text{N}_2)_y\text{Fe}_{2-z}\text{Se}_2$,^[33] $\text{Li}_x(\text{C}_6\text{H}_{16}\text{N}_2)_y\text{Fe}_{2-z}\text{Se}_2$ ^[34] and $A_x(\text{C}_8\text{H}_{11}\text{N})_y\text{Fe}_{1-z}\text{Se}$ ($A = \text{Li, Na}$)^[35] are formed, respectively. However, most of these compounds show a distinct sensibility to hydrolysis which impedes the operability with regard to further physical measurements.

A promising but so far hardly applied approach for the synthesis of new compounds containing FeSe layers is hydrothermal synthesis. β -FeSe only exists in a small stability region below about 450 °C,^[36] thus low-temperature hydrothermal synthesis where metastable compounds and low-temperature phases are accessible^[37] seems especially promising. Nitsche *et al.* showed that iron-selenide can be precipitated from aqueous solutions as metastable phase and recrystallized under hydrothermal conditions.^[18] This

metastable, stoichiometric phase of tetragonal FeSe is non-superconducting. The authors discuss that the nonappearance of superconductivity is due to the absence of intrinsic doping. Lu *et al.* reported the hydrothermal synthesis of $\text{LiFeO}_2(\text{FeSe})_2$.^[38] The as-reported compound is superconducting below 43 K and consists of layers of edge-sharing $\text{FeSe}_{4/4}$ tetrahedra which are separated by layers of $\text{Li}_{0.5}\text{Fe}_{0.5}\text{O}$. Later on it was shown that the compound is a hydroxide instead of an oxide, namely $[(\text{Li}_{0.8}\text{Fe}_{0.2})\text{OH}]\text{FeSe}$.^[39, 40] It is the first and so far only example where FeSe-layers alternate with hydroxide-layers and the results of Lu *et al.* indicate that hydrothermal synthesis is well suited for the formation of new FeSe-based superconductors.

In this thesis, the new approach for the synthesis of layered iron-chalcogenide superconductors via hydrothermal synthesis is further developed. Beside this preparative aspect, the structural and physical properties of the obtained compounds are in the focus of interest.

Chapter 3 concerns the binary compounds FeX ($X = \text{Se}, \text{S}$). A hydrothermal synthesis of *anti*- PbO type FeSe is developed and the influence of several synthesis parameters investigated (Chapter 3.1). An insight into the critical parameters of the hydrothermal synthesis of these compounds is gained and the optimal conditions are determined. In Chapter 3.2 the structural and physical properties of the as-prepared FeSe are investigated and compared with the ones of conventionally prepared FeSe as well as hydrothermally prepared FeS. The solid-solution $\text{FeSe}_{1-x}\text{S}_x$ ($0 \leq x \leq 1$) was prepared and characterized in Chapter 3.3. In contrast to solid-state reactions where a solubility limit is observed for $x = 0.3$, the whole solid-solution is accessible via hydrothermal synthesis. The effect of sulfur substitution upon the structural and superconducting properties of the compounds is discussed.

In Chapter 4 the layered lithium iron chalcogenide hydroxides $[(\text{Li}_{0.8}\text{Fe}_{0.2})\text{OH}]\text{FeX}$ ($X = \text{Se}, \text{S}$) are prepared and examined in detail. Chapter 4.1 concerns the structure determination and reveals that $[(\text{Li}_{0.8}\text{Fe}_{0.2})\text{OH}]\text{FeSe}$ is a ferromagnetic superconductor, where the antagonistic phenomena ferromagnetism and superconductivity coexist. The following Chapter 4.2 describes the determination of the upper critical field of this compound. Structure determination in Chapter 4.1 as well as further reports in literature left an unsettled issue concerning the strongly elongated displacement ellipsoid of the Li/Fe site in the magnetic $(\text{Li}_{0.8}\text{Fe}_{0.2})\text{OH}$ layer. Therefore, Chapter 4.3 is devoted to the investigation of the real structure of $[(\text{Li}_{0.8}\text{Fe}_{0.2})\text{OH}]\text{FeX}$ ($X = \text{Se}, \text{S}$) in terms of this structural ambiguity. To better

measure and understand physical properties, large crystals are often of great interest. In Chapter 4.4 large $[(\text{Li}_{0.8}\text{Fe}_{0.2})\text{OH}]\text{FeSe}$ crystals are prepared via hydrothermal ion-exchange synthesis and characterized with regard to structural and superconducting properties. In the following two Chapters 4.5 and 4.6, the effect of sulfur respectively cobalt substitution is investigated with regard to the coexistence of superconductivity and ferromagnetism.

Finally, the alkaline metal in the synthesis of $[(\text{Li}_{0.8}\text{Fe}_{0.2})\text{OH}]\text{FeSe}$ is varied from Li to Na, K, Rb and Cs in Chapter 5. Beside $\text{A}_2\text{Fe}_4\text{Se}_6$ ($\text{A} = \text{K}, \text{Rb}, \text{Cs}$) which is known in literature,^[41, 42] a new compound $\text{Na}_6(\text{H}_2\text{O})_{18}\text{Fe}_4\text{Se}_8$ is obtained. The structural and physical properties of the latter are examined in detail.

References

- [1] W. Nick, M. Frank, P. Kummeth, J. J. Rabbers, M. Wilke, K. Schleicher, *Journal of Physics: Conference Series* **2010**, 234, 032040.
- [2] N. Shigehiro, E. Steven, M. Adela, C. Kyeongdal, K. Woo Seok, T. Motoaki, D. Zigang, Z. Jun, W. Jiasu, U. Katsuya, D. Jia, F. Pascal, K. Shane, M. Oleg, D. C. Lance, P. F. Cathy, V. H. William, I. Mitsuru, *Superconductor Science and Technology* **2013**, 26, 113001.
- [3] L. Xiao, S. Dai, L. Lin, Z. Zhang, J. Zhang, *IEEE Transactions on Applied Superconductivity* **2013**, 23, 5401506-5401506.
- [4] J. Milton, *Nature News* **2010**, doi:10.1038/news.2010.527.
- [5] A. B. Abrahamsen, B. B. Jensen, E. Seiler, N. Mijatovic, V. M. Rodriguez-Zermeno, N. H. Andersen, J. Østergård, *Physica C: Superconductivity* **2011**, 471, 1464-1469.
- [6] H. Ohsaki, Y. Terao, M. Sekino, *Journal of Physics: Conference Series* **2010**, 234, 032043.
- [7] D. Johrendt, R. Pöttgen, *Angewandte Chemie International Edition* **2008**, 47, 4782-4784.
- [8] Y. Kamihara, T. Watanabe, M. Hirano, H. Hosono, *Journal of the American Chemical Society* **2008**, 130, 3296-3297.
- [9] M. Fujioka, S. J. Denholme, T. Ozaki, H. Okazaki, K. Deguchi, S. Demura, H. Hara, T. Watanabe, H. Takeya, T. Yamaguchi, H. Kumakura, Y. Takano, *Superconductor Science and Technology* **2013**, 26, 085023.
- [10] G. Stewart, *Reviews of Modern Physics* **2011**, 83, 1589-1652.

- [11] A. D. Christianson, E. A. Goremychkin, R. Osborn, S. Rosenkranz, M. D. Lumsden, C. D. Malliakas, I. S. Todorov, H. Claus, D. Y. Chung, M. G. Kanatzidis, R. I. Bewley, T. Guidi, *Nature* **2008**, *456*, 930-932.
- [12] D. J. Scalapino, *Reviews of Modern Physics* **2012**, *84*, 1383-1417.
- [13] J. D. Weiss, C. Tarantini, J. Jiang, F. Kametani, A. A. Polyanskii, D. C. Larbalestier, E. E. Hellstrom, *Nature Materials* **2012**, *11*, 682-685.
- [14] M. Rotter, M. Tegel, D. Johrendt, I. Schellenberg, W. Hermes, R. Pöttgen, *Physical Review B* **2008**, *78*, 020503.
- [15] M. Rotter, M. Tegel, D. Johrendt, *Physical Review Letters* **2008**, *101*, 107006.
- [16] F.-C. Hsu, J.-Y. Luo, K.-W. Yeh, T.-K. Chen, T.-W. Huang, P. M. Wu, Y.-C. Lee, Y.-L. Huang, Y.-Y. Chu, D.-C. Yan, M.-K. Wu, *Proceedings of the National Academy of Sciences* **2008**, *105*, 14262-14264.
- [17] T. M. McQueen, Q. Huang, V. Ksenofontov, C. Felser, Q. Xu, H. Zandbergen, Y. S. Hor, J. Allred, A. J. Williams, D. Qu, J. Checkelsky, N. P. Ong, R. J. Cava, *Physical Review B* **2009**, *79*, 014522.
- [18] F. Nitsche, T. Goltz, H. H. Klauss, A. Isaeva, U. Müller, W. Schnelle, P. Simon, T. Doert, M. Ruck, *Inorganic Chemistry* **2012**, *51*, 7370-7376.
- [19] A. J. Williams, T. M. McQueen, R. J. Cava, *Solid State Communications* **2009**, *149*, 1507-1509.
- [20] S. Medvedev, T. M. McQueen, I. A. Troyan, T. Palasyuk, M. I. Eremets, R. J. Cava, S. Naghavi, F. Casper, V. Ksenofontov, G. Wortmann, C. Felser, *Nature Materials* **2009**, *8*, 630-633.
- [21] M. Burrard-Lucas, D. G. Free, S. J. Sedlmaier, J. D. Wright, S. J. Cassidy, Y. Hara, A. J. Corkett, T. Lancaster, P. J. Baker, S. J. Blundell, S. J. Clarke, *Nature Materials* **2013**, *12*, 15-19.
- [22] J.-F. Ge, Z.-L. Liu, C. Liu, C.-L. Gao, D. Qian, Q.-K. Xue, Y. Liu, J.-F. Jia, *Nature Materials* **2015**, *14*, 285-289.
- [23] X. Ding, D. Fang, Z. Wang, H. Yang, J. Liu, Q. Deng, G. Ma, C. Meng, Y. Hu, H.-H. Wen, *Nature Communications* **2013**, *4*, 1897.
- [24] V. Ksenofontov, G. Wortmann, S. A. Medvedev, V. Tsurkan, J. Deisenhofer, A. Loidl, C. Felser, *Physical Review B* **2011**, *84*, 180508.
- [25] W. Li, H. Ding, P. Deng, K. Chang, C. Song, K. He, L. Wang, X. Ma, J.-P. Hu, X. Chen, Q.-K. Xue, *Nature Physics* **2012**, *8*, 126-130.
- [26] Z. Shermadini, A. Krzton-Maziopa, M. Bendele, R. Khasanov, H. Luetkens, K. Conder, E. Pomjakushina, S. Weyeneth, V. Pomjakushin, O. Bossen, A. Amato, *Physical Review Letters* **2011**, *106*, 117602.

- [27] S. C. Speller, T. B. Britton, G. M. Hughes, A. Krzton-Maziopa, E. Pomjakushina, K. Conder, A. T. Boothroyd, C. R. M. Grovenor, *Superconductor Science and Technology* **2012**, *25*, 084023.
- [28] F. R. Foronda, S. Ghannadzadeh, S. J. Sedlmaier, J. D. Wright, K. Burns, S. J. Cassidy, P. A. Goddard, T. Lancaster, S. J. Clarke, S. J. Blundell, *Physical Review B* **2015**, *92*, 134517.
- [29] E.-W. Scheidt, V. R. Hathwar, D. Schmitz, A. Dunbar, W. Scherer, F. Mayr, V. Tsurkan, J. Deisenhofer, A. Loidl, *The European Physical Journal B* **2012**, *85*, 1-5.
- [30] S. J. Sedlmaier, S. J. Cassidy, R. G. Morris, M. Drakopoulos, C. Reinhard, S. J. Moorhouse, D. O'Hare, P. Manuel, D. Khalyavin, S. J. Clarke, *Journal of the American Chemical Society* **2014**, *136*, 630-633.
- [31] T. P. Ying, X. L. Chen, G. Wang, S. F. Jin, T. T. Zhou, X. F. Lai, H. Zhang, W. Y. Wang, *Scientific Reports* **2012**, *2*, 426.
- [32] A. Krzton-Maziopa, E. V. Pomjakushina, V. Y. Pomjakushin, F. v. Rohr, A. Schilling, K. Conder, *Journal of Physics: Condensed Matter* **2012**, *24*, 382202.
- [33] T. Hatakeda, T. Noji, T. Kawamata, M. Kato, Y. Koike, *Journal of the Physical Society of Japan* **2013**, *82*, 123705.
- [34] S. Hosono, T. Noji, T. Hatakeda, T. Kawamata, M. Kato, Y. Koike, *Journal of the Physical Society of Japan* **2014**, *83*, 113704.
- [35] T. Hatakeda, T. Noji, K. Sato, T. Kawamata, M. Kato, Y. Koike, *Journal of the Physical Society of Japan* **2016**, *85*, 103702.
- [36] H. J. Okamoto, *Journal of Phase Equilibria* **1991**, *12*, 383-389.
- [37] A. Rabenau, *Angewandte Chemie International Edition in English* **1985**, *24*, 1026-1040.
- [38] X. F. Lu, N. Z. Wang, G. H. Zhang, X. G. Luo, Z. M. Ma, B. Lei, F. Q. Huang, X. H. Chen, *Physical Review B* **2014**, *89*, 020507.
- [39] X. F. Lu, N. Z. Wang, H. Wu, Y. P. Wu, D. Zhao, X. Z. Zeng, X. G. Luo, T. Wu, W. Bao, G. H. Zhang, F. Q. Huang, Q. Z. Huang, X. H. Chen, *Nature Materials* **2015**, *14*, 325-329.
- [40] U. Pachmayr, F. Nitsche, H. Luetkens, S. Kamusella, F. Brückner, R. Sarkar, H.-H. Klauss, D. Johrendt, *Angewandte Chemie International Edition* **2015**, *54*, 293-297.
- [41] J. M. Caron, J. R. Neilson, D. C. Miller, K. Arpino, A. Llobet, T. M. McQueen, *Physical Review B* **2012**, *85*, 180405.
- [42] F. Du, K. Ohgushi, Y. Nambu, T. Kawakami, M. Avdeev, Y. Hirata, Y. Watanabe, T. J. Sato, Y. Ueda, *Physical Review B* **2012**, *85*, 214436.

2 Methods

2.1 Synthetic methods

2.1.1 Starting materials

Tab. 1 lists the starting materials used in this work, including their constitution, supplier and purity.

Tab. 1: Starting materials used in this work.

| <i>Substance</i> | <i>Constitution</i> | <i>Supplier</i> | <i>Purity (%)</i> |
|----------------------------------------|-------------------------|-------------------|-------------------|
| Co | powder | SIGMA-ALDRICH | 99.9 |
| CsOH | 50 wt% aqueous solution | ABCR | 99.9 |
| Fe | powder | CHEMPUR | 99.9 |
| K | ingot | SIGMA-ALDRICH | 99.95 |
| KOH | platelets | APPLICHEM | 85 |
| LiOH·H ₂ O | powder | FISHER SCIENTIFIC | 99 |
| Na ₂ S · 9 H ₂ O | platelets | SIGMA-ALDRICH | 98 |
| NaBH ₄ | powder | ACROS | 98 |
| NaOH | pellets | GRÜSSING | 99 |
| RbOH·H ₂ O | fused solid | ABCR | 99.8 |
| SCN ₂ H ₄ | crystals | GRÜSSING | 99 |
| Se | granules | CHEMPUR | 99.999 |
| SeCN ₂ H ₄ | crystals | ALFA AESAR | 99 |

Air-sensitive materials were handled and stored in a glove box (MBRAUN, MB150-GL with H₂O and O₂ < 1 ppm and UNILAB Plus with H₂O and O₂ < 0.1 ppm) under an atmosphere of purified argon (99.999 %, AIR LIQUIDE).

2.1.2 Equipment and conditions

This chapter describes the general synthetic conditions. Detailed information on the individual synthesis processes are given in the experimental section of the corresponding chapter.

Hydrothermal synthesis

Hydrothermal synthesis was performed in BERGHOF DAB-2 pressure vessels of 50 mL filling capacity (Fig. 1). The pressure vessels with moveable base plate and bayonet-like quick-lock

device are made of an alloyed CrNiMo stainless steel. Inside the pressure vessel an exchangeable PTFE-liner with lid forms a dense system. The maximum heating temperature of 250 °C is limited by the heat stability of PTFE. The pressure vessel is secured against too high pressure (the maximum pressure is 200 bar) by means of a rupture disc.

In Fig. 1 the components of a BERGHOF DAB-2 pressure vessel are depicted. For hydrothermal synthesis, the educts were loaded in the PTFE-liner with lid under argon atmosphere. The latter was placed in the cylindrical base body with base plate and sealed with the pressing plate and the bayonet-like head piece. A locking force of 25 Nm was applied. To protect the rupture disc against aggressive fumes, an aluminium foil was placed between the PTFE-lid and the pressing plate.

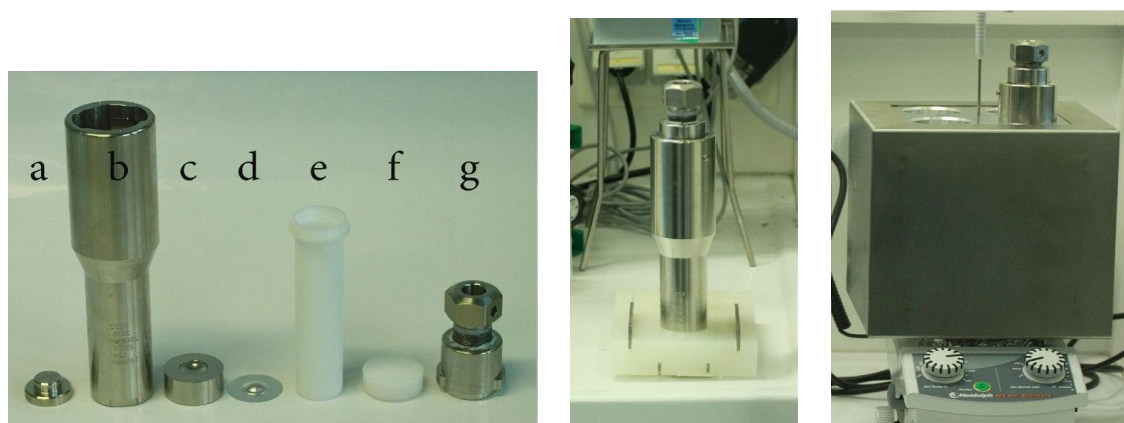


Fig. 1: Left: components of a BERGHOF DAB-2 pressure vessel: a) base plate, b) cylindrical base body, c) pressing plate with rupture disc, d) aluminium foil, e) PTFE-liner, f) PTFE-lid, g) bayonet-like head piece; center: assembled pressure vessel; right: pressure vessel in heating device.

For heating of the pressure vessels, an in-house made heater block mount made of aluminium with thermo-insulating safety hood was employed (Fig. 1, right). The mount was heated by a HEIDOLPH MR Hei-Standard laboratory heating plate with HEIDOLPH EKT Hei-Con temperature regulator.

For the investigation of the influence of pressure on the hydrothermal synthesis, a BERGHOF BR-100 high pressure reactor was used (Fig. 2), which allows a permanent survey of pressure and temperature inside the reactor. The reactor is constructed of Hastelloy and a PTFE lining is used for optimal corrosion protection of the reactor vessel. For the hydrothermal synthesis, PTFE linings of 150 mL filling volume were used. The constraint of

maximal heating temperature and pressure is identical to the BERGHOF DAB-2 pressure vessels.

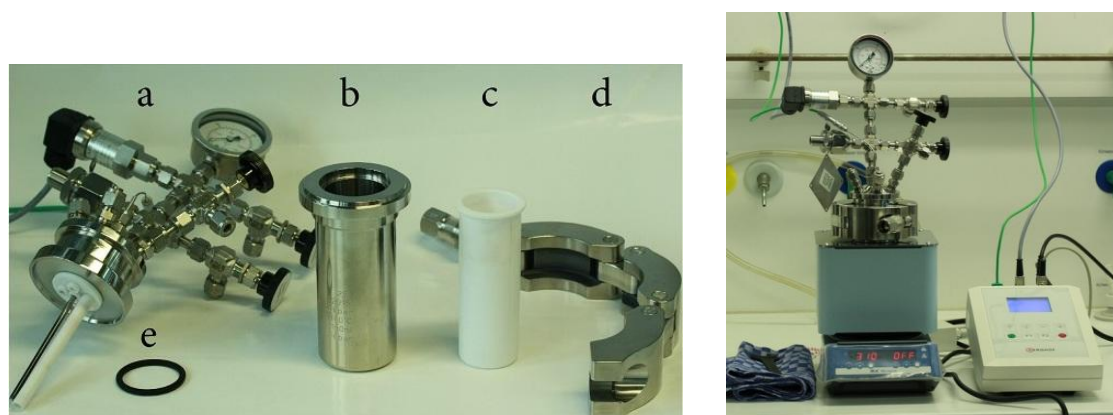


Fig. 2: Left: components of a BERGHOF BR-100 high pressure reactor: a) reactor lid with pressure measurement, dip tube for temperature sensor and liquid sample extraction, rupture disc and vent valve, b) base body, c) PTFE-liner, d) quick clamping chain, e) O-ring of FMP to seal the reactor; right: assembled high pressure reactor in heating device.

Conventional solid-state synthesis

Conventional solid state syntheses were performed in alumina crucibles (FRIATEC). The crucibles containing the educts were transferred into pre-dried silica ampoules (VOGELSBERGER, HSQ 300) and sealed under argon atmosphere. The reactions were performed in tubular resistance furnaces with Pt/PtRh thermocouples and PID temperature controllers (EUROTHERM, model 2408).

2.2 Analytical methods

X-ray powder diffraction

Powder X-ray diffraction was carried out using a HUBER G670 diffractometer with Cu- $K\alpha_1$ radiation ($\lambda = 154.05$ pm) at room temperature. For low temperatures, Co- $K\alpha_1$ radiation ($\lambda = 179.02$ pm) and a close-cycle He-cryostat was employed. Structural parameters were obtained by Rietveld refinement using the software package TOPAS^[1].

X-ray single crystal diffraction

Single-crystal analysis was performed on a BRUKER D8 Quest diffractometer (Mo-K α_1 , $\lambda = 71.073$ pm). For low-temperature single-crystal analysis, a BRUKER D8 Venture diffractometer (Mo-K α_1 , $\lambda = 71.073$ pm) was used. The temperature-dependent measurements were recorded between 300 and 100 K using the KRYOFLEX low-temperature attachment (BRUKER AXS).

Intensities were integrated with the BRUKER APEX2 software package and absorption correction was performed with the multiscan method SADABS.^[2, 3] The structure was solved and refined against F^2 with the JANA2006 program package.^[4]

Some single crystals were additionally examined using synchrotron radiation ($\lambda = 18.9722$ pm) at beamline ID11 in the EUROPEAN SYNCHROTRON RADIATION FACILITY (ESRF), Grenoble.

Transmission electron microscopy measurements

Transmission electron microscopy (TEM) was performed by L. Neudert, LMU Munich, on a Cs-corrected transmission electron microscope FEI TITAN THEMIS with field emission cathode and CMOS camera FEI CETA. EDX measurements were recorded with a windowless four-quadrant SUPERX detector and evaluated with the program ESVISION.^[5] For simulations of SAED (selected area electron diffraction) patterns the program JEMS was applied.^[6]

Magnetic measurements

Magnetic measurements were carried out at a SQUID magnetometer (MPMS-XL5, QUANTUM DESIGN, Inc.) with applied fields of -5 to 5 T. Superconductivity was additionally examined in a differential dual-coil AC susceptometer with an applied field of 0.3 mT.

Resistivity measurements

Temperature-dependent resistivity measurements were carried out on cold-pressed pellets with a diameter of 4 mm using a standard four-probe method. The temperature-dependent resistivity measurements under different magnetic fields up to 15 T were carried out at the Walther-Meißner-Institut (WMI), Garching.

Chemical composition

Chemical composition was determined by energy-dispersive X-ray analysis (EDX) as well as by chemical methods using inductively coupled plasma atomic absorption spectroscopy (ICP-AAS) and elemental analysis.

EDX experiments were performed on a CARL ZEISS EVO-MA 10 with SE-, BSE- and a BRUKER Nano EDX (X-Flash 410-M) detector. For ICP-AAS, a VARIAN Vista RL was used. Elemental analysis was performed with an ELEMENTAR vario MICRO cube.

pH value

To determine the pH value of the obtained aqueous solutions, a pH meter METTLER TOLEDO MP 220 with Ag/AgCl electrode was applied.

Raman spectroscopy

Raman spectroscopy was performed by S. Datz, LMU Munich, employing a Raman spectrometer equipped with an He-Ne laser ($\lambda = 633$ nm). A confocal LABRAM HR UV/VIS (HORIBA Jobin Yvon) Raman microscope (OLYMPUS BX 41) with a SYMPHONY CCD detection system was used.

Mössbauer spectroscopy

^{57}Fe -Mössbauer spectroscopy was performed in cooperation with S. Kamusella, TU Dresden. A standard Wissel setup in transmission geometry using a Co/Rh source with an experimental line width (HWHM) $\omega_{\text{exp}} = 0.13$ mm/s was used.

Nuclear magnetic resonance

^7Li nuclear magnetic resonance (NMR) spectra were taken by Dr. R. Sarkar, TU Dresden, at several temperatures using the Fourier-transformation field-sweep method.

Muon spin rotation

Muon spin rotation (μSR) experiments were carried out with the GPS spectrometer at the pM3.2 beamline of the Swiss Muon Source at the Paul Scherrer Institut (Villigen, Switzerland) in cooperation with Dr. H. Luetkens and S. Holenstein. The data were analyzed using the musrfit package.^[7]

Density functional theory calculations

Electronic structure calculations were performed using the Vienna *ab initio* simulation package (VASP),^[8, 9] which is based on density functional theory (DFT) and plane-wave basis sets. Projector-augmented waves (PAW)^[10] were used and contributions of correlation and exchange were treated in the generalized-gradient approximation (GGA) as described by Perdew, Burke, and Ernzerhof.^[11]

2.3 References

- [1] A. Coelho, *TOPAS-Academic, Vol. 4.1*, TOPAS-Academic, Version 4.1, Coelho Software, Brisbane, **2007**.
- [2] *APEX2, Vol. 2014.1*, Bruker AXS Inc., Madison, Wisconsin, USA, **2014**.
- [3] G. M. Sheldrick, *SADABS, Multi-Scan Absorption Correction, Vol. 2*, Bruker AXS Inc., Madison, Wisconsin, USA, **2012**.
- [4] V. Petricek, M. Dusek, L. Palatinus, *Jana2006*, Structure Determination Software Programs, Institute of Physics, Praha, Czech Republic, **2009**.
- [5] *ESVision Vol. 4.0.164*, Emispec Systems Inc., Quebec, Canada, **2002**.
- [6] P. A. Stadelmann, *JEMS, Vol. 3.3425*, CIME-EPFL, Switzerland, **2008**.
- [7] G. M. Luke, J. Sonier, A. Suter, B. M. Wojek, *Physics Procedia* **2012**, 30, 69-73.
- [8] G. Kresse, J. Furthmüller, *Computational Materials Science* **1996**, 6, 15-50.
- [9] G. Kresse, J. Hafner, *Physical Review B* **1994**, 49, 14251-14269.
- [10] P. E. Blöchl, *Physical Review B* **1994**, 50, 17953-17979.
- [11] J. P. Perdew, K. Burke, M. Ernzerhof, *Physical Review Letters* **1996**, 77, 3865-3868.

3 Hydrothermally prepared FeX (X = Se, S)

3.1 Influence of synthesis parameters on the hydrothermal synthesis of FeSe

3.1.1 Introduction

Hydrothermal syntheses are heterogeneous reactions in aqueous media above 100 °C and 1 bar.^[1] The preparative possibilities of hydrothermal synthesis in solid state chemistry are based on advantages like the accessibility of compounds with elements in oxidation states that are difficult to attain, low-temperature phases and metastable compounds.^[1] Thereby, the adjustment of numerous parameters like temperature, pH value, redox potential, reaction time and pressure offers the possibility to make the desired products accessible. However, most of the parameters are not independent, i.e. they influence each other as illustrated in Fig. 1. As a consequence the adjustment of optimal synthesis conditions becomes challenging.

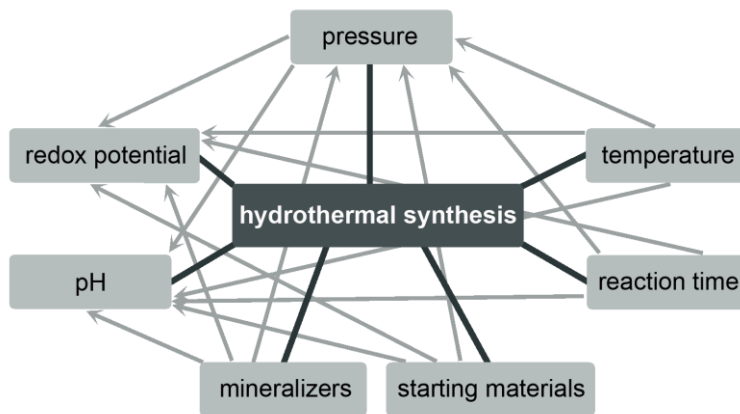


Fig. 1: Parameters for hydrothermal synthesis. Arrows indicate the respective dependence of two parameters.

For the preparation of iron based superconductors, this promising synthesis approach is barely applied so far. However, strictly anhydrous solvothermal synthesis and room temperature intercalation in organic solvents yielded superconducting iron selenides, among them β -FeSe ($T_c = 8$ K),^[2] $\text{Li}_x(\text{NH}_2)_y(\text{NH}_3)_{1-y}\text{Fe}_2\text{Se}_2$ ($T_c = 43$ K),^[3, 4] $A_x(\text{C}_5\text{H}_5\text{N})_y\text{Fe}_{2-z}\text{Se}_2$ ($A = \text{Li, Na, K, Rb}$; $T_c \approx 45$ K)^[5] and $\text{Li}_x(\text{C}_2\text{H}_8\text{N}_2)_y\text{Fe}_{2-z}\text{Se}_2$ ($T_c \approx 45$ K).^[6] Lu *et al.* reported the

hydrothermal synthesis of a layered iron based superconductor $\text{LiFeO}_2\text{Fe}_2\text{Se}_2$ with $T_c = 43 \text{ K}$.^[7] This work expanded the categories of iron-based superconductors with regard to new compounds and was some kind of a starting point for the present thesis.

To advance in this emergent field of hydrothermally prepared iron-chalcogenide superconductors, first experiences regarding the influence of synthesis parameters were acquired in this chapter. $\beta\text{-FeSe}$ was selected as target compound as it adopts the simplest crystal structure of any known iron-based superconductor and can be seen as the basic structure of the compounds of interest. Nitsche *et al.* showed that stoichiometric $\beta\text{-FeSe}$ can be precipitated from aqueous solutions of Li_2Se and FeI_2 as metastable phase.^[8] Via hydrothermal recrystallization the crystallinity of the amorphous precipitate was increased, however the particle size remained in the range of nanoparticles. This stoichiometric phase of FeSe is non-superconducting, possibly due to the absence of intrinsic doping. Based on these ideas, a hydrothermal synthesis of highly crystalline $\beta\text{-FeSe}$ is developed in this chapter starting from elemental iron and selenium powders. The influence of several synthesis parameters is investigated in order to gain a deeper insight into the hydrothermal synthesis of these compounds.

3.1.2 Experimental details

Hydrothermal synthesis of FeSe was performed with variations of the amounts of NaBH_4 and KOH, reaction time and temperature.

Variation of the amount of NaBH_4 and KOH

1.0 mmol Fe (55.8 mg) and Se (79.0 mg) together with various concentrations of NaBH_4 and KOH were used as starting materials. In Fig. 2, the respective amounts of NaBH_4 and KOH used for the syntheses are marked by blue squares.

The educts were mixed with distilled water (20 mL), sealed in a teflon-lined steel autoclave (50 mL) under argon atmosphere and heated at 155°C for 6 days. The obtained black precipitates were collected by centrifugation and washed with distilled water and ethanol. The samples were dried at room temperature under dynamic vacuum and stored in a purified argon atmosphere glove box.

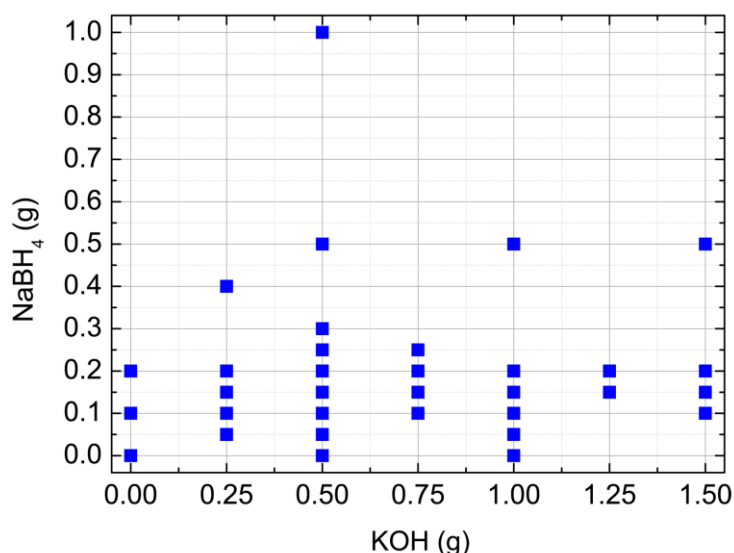


Fig. 2: Respective amounts of NaBH₄ and KOH used for the hydrothermal syntheses of FeSe (marked by blue squares).

Variation of reaction time

The syntheses in which the influence of reaction time was investigated were performed analogously. 1.0 mmol elementary Fe (55.8 mg) and Se (79.0 mg) as well as 0.50 g (8.91 mmol) KOH and 0.15 g (3.97 mmol) NaBH₄ were used as optimized starting materials. A reaction time of 1, 3, 6, 10, 14 and 18 days was applied.

Variation of temperature

For the syntheses with variation of temperature, a teflon-lined steel autoclave (BERGHOF BR-100 high pressure reactor) with a volume of 150 mL was used which allows a permanent survey of pressure and temperature inside the reactor. 3.0 mmol Fe metal (0.17 g) and Se (0.24 g) as well as 1.50 g (26.7 mmol) KOH and 0.15 g (23.8 mmol) NaBH₄ were used together with 60 mL distilled water. Reaction temperatures of 160, 170, 175, 180, 185 and 190 °C were applied with a reaction time of 7 days.

3.1.3 Results and discussion

A hydrothermal synthesis of *anti*-PbO type FeSe was developed starting from elementary iron and selenium. For the creation of appropriate synthesis conditions, NaBH₄ was used as reducing agent and KOH for the adjustment of the pH value. In the following, the influence of the amount of NaBH₄ and KOH, reaction time, pressure and temperature is investigated with

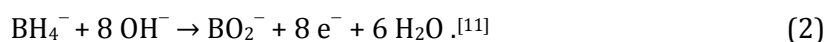
respect to the formation of FeSe. The structural and physical properties of the synthesized FeSe are discussed in the following chapter.

Variation of the amount of NaBH₄ and / or KOH

KOH is a strong base and leads to a vigorous increase of pH value of aqueous solutions even for small concentrations. All batches containing KOH showed a pH value larger than 13. For the batches containing no KOH but NaBH₄, an increase of pH value was observed as well. This is caused by the formation of the strongly basic metaborate ion during hydrolysis of sodium borohydride



The stability of NaBH₄ in aqueous solutions depends on the temperature, the pH value and the presence of catalysts.^[9, 10] An increase of temperature, a decrease of pH value as well as the presence of catalysts result in an accelerated decomposition. Apart from this alkaline property, NaBH₄ primarily serves as reducing agent. Alkaline solutions of pH larger than 12 hinder the hydrolysis reaction and the tetrahydroborate anion can be oxidized directly providing eight electrons according to



First, the influence of the pH value of the solution on the synthesis of FeSe was investigated. Different amounts of KOH were used whereby the amount of NaBH₄ was kept constant at 0.2 g. The black solids obtained were examined with X-ray powder diffraction and subsequent Rietveld-analysis. Fig. 3 exemplarily shows the X-ray powder pattern with Rietveld-fit for a sample synthesized with 0.5 g KOH. The absolute yield in mol% of the obtained phases related to the amount of Fe and Se used is depicted in Fig. 4.

The sample prepared without KOH shows no signs of the desired compound FeSe. The educt Fe as well as the iron-selenide FeSe₂ occur in approximately equal shares. Given the present pH is about 10.6, part of the NaBH₄ will be hydrolyzed providing less electrons for possible reduction processes.^[12] In the present solution with a comparably small reduction potential the compound FeSe₂ containing [Se₂]²⁻ units^[13] is apparently more stable than FeSe. By addition of 0.25 g KOH, NaBH₄ is stabilized and the hydrolysis reaction is hindered. The desired iron-selenide FeSe arises as main phase beside 8 mol% of unreacted Fe. For KOH quantities ≥ 0.75 g, the yield of FeSe declines whereby Fe₃O₄ is formed at an increasing rate. For 1.25 g KOH the formation of FeSe is completely suppressed and Fe₃O₄ is the only phase obtained beside Fe. Thus, the amount of KOH and by association the pH value is essential for

the synthesis of FeSe. A small amount of KOH is necessary, whereas quantities larger than 1.25 g prevent the formation of FeSe under the present conditions.

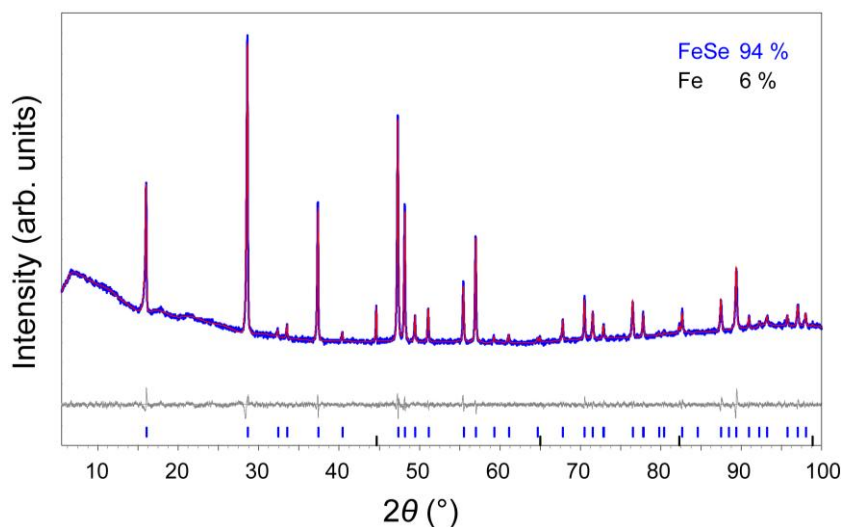


Fig. 3: X-ray powder pattern (blue) with Rietveld-fit (red) and difference plot (gray) of a sample synthesized with 0.5 g KOH and 0.2 g NaBH₄.

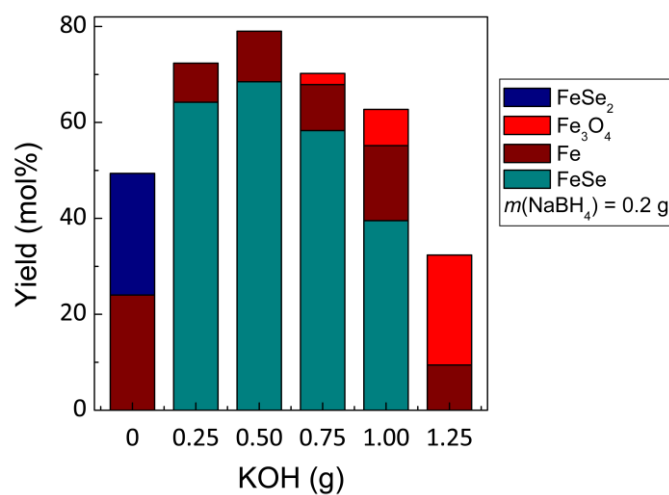


Fig. 4: Yield of the obtained phases in mol% for 0.2 g NaBH₄ dependent on the amount of KOH.

The influence of the reduction potential of the solution on the synthesis of FeSe was investigated in relation to the amount of NaBH₄ used. The synthesis was performed with various amounts of NaBH₄ whereby the amount of KOH was kept constant to 0.5 g

respectively 1.0 g. Fig. 5 shows the yield of the phases obtained, related to the amount of Fe and Se used.

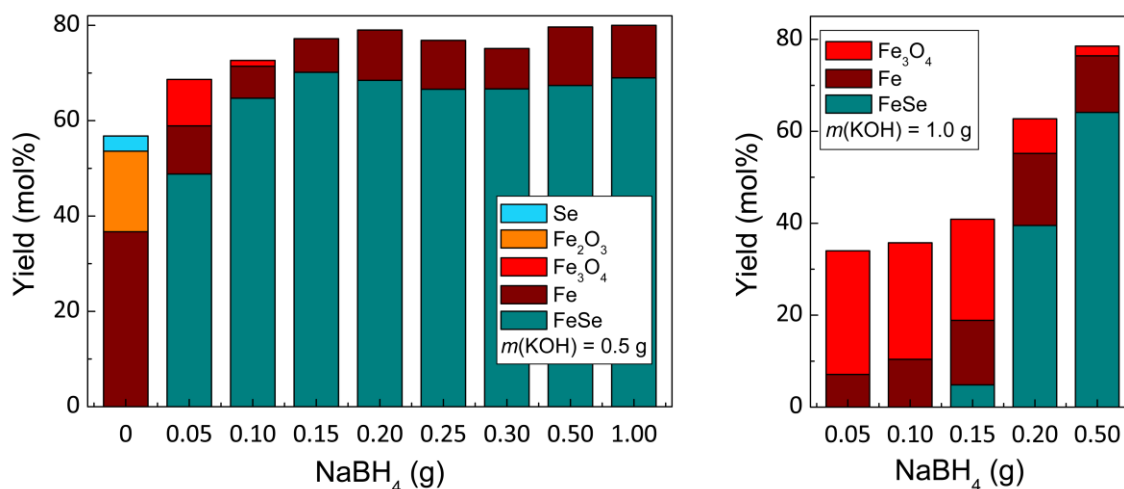


Fig. 5: Yield of the phases in mol% obtained for 0.5 g (left) and 1.0 g (right) KOH dependent on the amount of NaBH_4 , respectively.

The two diagrams are distinctly different in conformity with the influence of the amount of KOH (Fig. 4). The syntheses with 0.5 g KOH, which appeared to be the optimal amount in combination with 0.2 g NaBH_4 , yield FeSe as main phase for almost all batches. The only exception is the batch where no NaBH_4 is used at all. Beside Fe and residues of Se, the iron(III)-oxide Fe_2O_3 is the only solid formed. This changes when even small amounts of NaBH_4 are added. 0.05 g of the reducing agent leads to the formation of FeSe as main phase together with Fe and Fe_3O_4 . For NaBH_4 quantities of 0.15 g and larger, FeSe is obtained with a yield of about 70 % related to the starting amount of Fe and Se. The only side phase under these conditions is Fe. Interestingly, the yield of FeSe is more or less constant from 0.15 g to 1.00 g NaBH_4 . A large amount of reducing agent thus has no negative impact on the synthesis of FeSe.

The syntheses with 1.0 g KOH reveal that an enlarged amount of KOH requires an increased amount of NaBH_4 as well to synthesize FeSe. Here, 0.5 g NaBH_4 is necessary to obtain FeSe in a yield comparable to the one of 0.10 g NaBH_4 for the synthesis with 0.5 g KOH.

The presence of a reducing agent, here NaBH_4 , is thus essential for the synthesis of FeSe, whereby the quantity needed is dependent on the amount of KOH.

Hence, the synthesis of FeSe is strongly dependent on the amount of KOH and NaBH₄. The parameters influence each other and therefore have to be considered both together. In Fig. 6 the yield of the desired phase FeSe as well as the most frequent further phases Fe and Fe₃O₄ are depicted dependent on the amount of KOH and NaBH₄ used. The colours represent the respective yield of the phase in mol% related to the starting amount of Fe and Se.

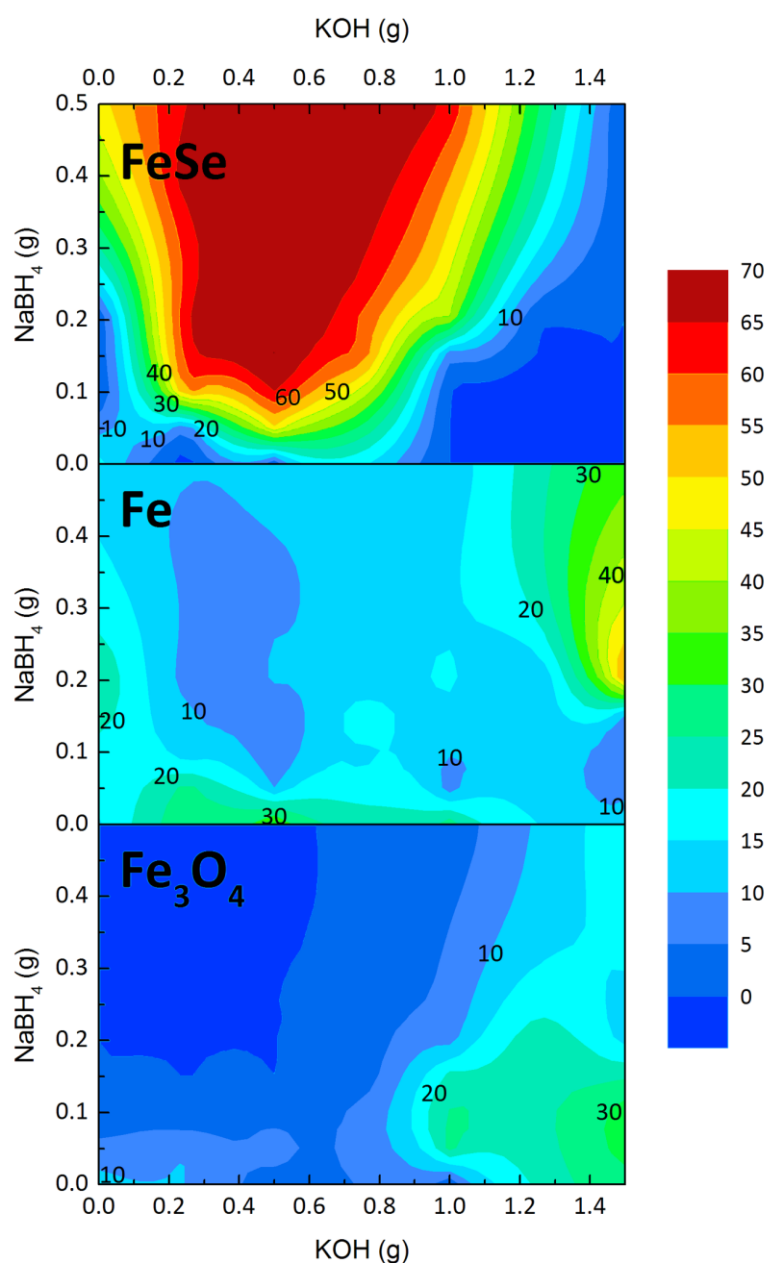
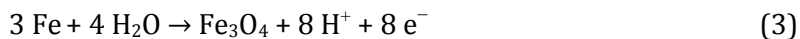


Fig. 6: Yield of the desired phase FeSe as well as Fe and Fe₃O₄ dependent on the amount of KOH and NaBH₄ used. The colours represent the respective yield of the phase in mol% related to the starting amount of Fe and Se.

For the present conditions, FeSe is obtained in a yield of over 60 mol% for about 0.1–0.5 g NaBH₄ and 0.2–0.8 g KOH. An increase in the amount of NaBH₄ yields a continuous increase of the amount of KOH applicable without reduction of the yield. Fe is present over the whole range investigated, whereas Fe₃O₄ is predominantly formed at large amounts of KOH and relatively small amounts (< 0.2 g) of NaBH₄. When the amount of NaBH₄ is increased in this region of large pH value the formation of Fe is preferred. Equation (3) illustrates this behavior.^[14]



A large pH value (large amount of KOH) drives the reaction in the direction of Fe₃O₄ whereas a large negative potential (large amount of NaBH₄) stabilizes Fe.

Variation of reaction time

Another parameter which influences the synthesis of FeSe is the reaction time. Fig. 7 illustrates the dependency of the synthesis products from heating time. The best yield of 70 mol% FeSe was obtained for a heating time of 6 days. 3 days or less is apparently too short as a large amount of Fe (46 and 27 mol% for 1 and 3 days, respectively) remains unreacted. Longer times lead to a further reaction of Fe, however Fe₃O₄ is formed in increasing amount and the yield of FeSe continuously decreases.

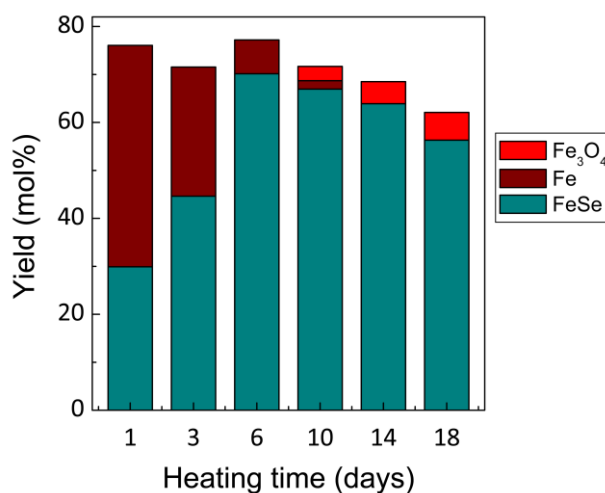


Fig. 7: Yield of the obtained phases in mol% dependent on the reaction time.

In Fig. 8, scanning electron microscopy (SEM) images of samples with 1 day respectively 6 days reaction time illustrate the crystal growth.

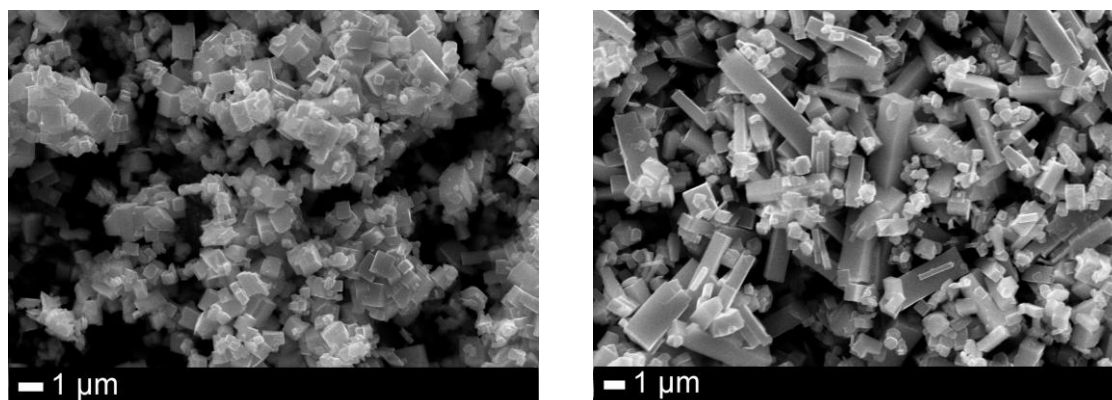


Fig. 8: SEM images of samples with 1 day (left) and 6 days (right) reaction time, respectively.

Variation of temperature

The influence of the temperature on the synthesis of FeSe is shown in Fig. 9. First, the development of pressure with temperature is examined (Fig. 9, left). The pressure increases with increasing temperature, which can be explained by the enhanced hydrolysis of NaBH_4 as well as the common increase of pressure with temperature within a constant volume.

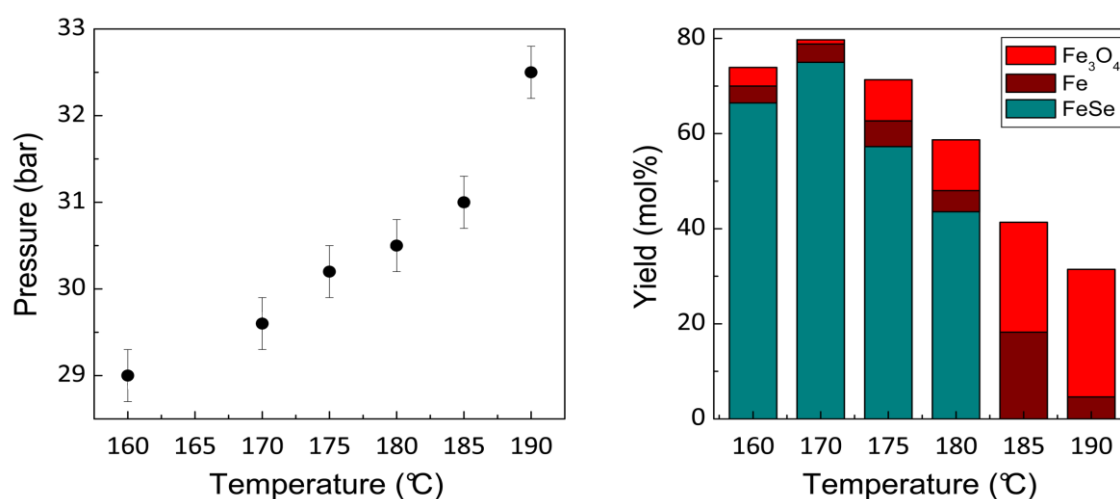


Fig. 9: Pressure within the reactor (left) and yield of the obtained phases in mol% (right) dependent on temperature; the yield is related to the starting amount of Fe and Se.

The amplified hydrolysis, thus the decrease in reduction potential of the solution might have an impact on the yield of the obtained phases dependent on temperature. For temperatures higher than 170 °C, the yield of FeSe continuously decreases whereas Fe₃O₄ emerges in increasing amounts. From 185 °C on, Fe₃O₄ is the only solid formed beside some amount of unreacted iron.

3.1.4 Conclusion

A hydrothermal synthesis of *anti*-PbO type FeSe was developed starting from elementary Fe and Se. The reduction potential and pH value of the solution as well as reaction time and temperature have wide influence on the success of the synthesis. The optimal amount of the base KOH and the reducing agent NaBH₄ was determined to 0.50 g (0.45 mol/L) and at least 0.15 g (0.20 mol/L) based on 20 mL H₂O, respectively. A larger concentration of KOH seems to favor the formation of Fe₃O₄ whereas no adverse effect was observed for a larger concentration of NaBH₄. A heating time of 6 days and temperatures of 170 °C or lower enable the formation of FeSe in a maximum yield of about 70 mol% related to the starting amount of Fe and Se. At optimized conditions, residuals of the educt Fe are the only impurity phase. It can easily be removed applying a magnetic field during the washing step. However, it is important to be aware that tiny amounts of Fe might remain in the samples. These residuals of Fe can have significant influence on magnetic measurements.

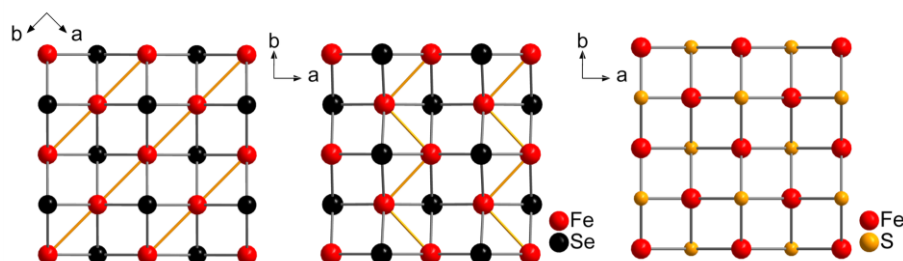
3.1.5 References

- [1] A. Rabenau, *Angewandte Chemie International Edition in English* **1985**, *24*, 1026-1040.
- [2] J. T. Greenfield, S. Kamali, K. Lee, K. Kovnir, *Chemistry of Materials* **2015**, *27*, 588-596.
- [3] M. Burrard-Lucas, D. G. Free, S. J. Sedlmaier, J. D. Wright, S. J. Cassidy, Y. Hara, A. J. Corkett, T. Lancaster, P. J. Baker, S. J. Blundell, S. J. Clarke, *Nature Materials* **2013**, *12*, 15-19.
- [4] S. J. Sedlmaier, S. J. Cassidy, R. G. Morris, M. Drakopoulos, C. Reinhard, S. J. Moorhouse, D. O'Hare, P. Manuel, D. Khalyavin, S. J. Clarke, *Journal of the American Chemical Society* **2014**, *136*, 630-633.
- [5] A. Krzton-Maziopa, E. V. Pomjakushina, V. Y. Pomjakushin, F. v. Rohr, A. Schilling, K. Conder, *Journal of Physics: Condensed Matter* **2012**, *24*, 382202.
- [6] T. Hatakeda, T. Noji, T. Kawamata, M. Kato, Y. Koike, *Journal of the Physical Society of Japan* **2013**, *82*, 123705.

-
- [7] X. F. Lu, N. Z. Wang, G. H. Zhang, X. G. Luo, Z. M. Ma, B. Lei, F. Q. Huang, X. H. Chen, *Physical Review B* **2014**, *89*, 020507.
- [8] F. Nitsche, T. Goltz, H. H. Klauss, A. Isaeva, U. Müller, W. Schnelle, P. Simon, T. Doert, M. Ruck, *Inorganic Chemistry* **2012**, *51*, 7370-7376.
- [9] H. I. Schlesinger, H. C. Brown, A. E. Finholt, J. R. Gilbreath, H. R. Hoekstra, E. K. Hyde, *Journal of the American Chemical Society* **1953**, *75*, 215-219.
- [10] S. C. Amendola, S. L. Sharp-Goldman, M. S. Janjua, M. T. Kelly, P. J. Petillo, M. Binder, *Journal of Power Sources* **2000**, *85*, 186-189.
- [11] M. Chatenet, F. Micoud, I. Roche, E. Chainet, *Electrochimica Acta* **2006**, *51*, 5459-5467.
- [12] S. C. Amendola, P. Onnerud, M. T. Kelly, P. J. Petillo, S. L. Sharp-Goldman, M. Binder, *Journal of Power Sources* **1999**, *84*, 130-133.
- [13] B. Yuan, W. Luan, S.-t. Tu, *Dalton Transactions* **2012**, *41*, 772-776.
- [14] E. D. Verink, in *Uhlig's Corrosion Handbook*, John Wiley & Sons, Inc., **2011**, pp. 93-101.

3.2 Structural transition and superconductivity in hydrothermally synthesized FeX (X = S, Se)

Ursula Pachmayr, Natalie Fehn, and Dirk Johrendt



published in: *Chemical Communications* **2016**, 52, 194-197.

Copyright 2016, Royal Society of Chemistry.

Abstract

Iron selenide obtained by mild hydrothermal reaction is not superconducting and exhibits a triclinic crystal structure below 60 K unlike superconducting FeSe from conventional solid state synthesis which is orthorhombic. In contrast, tetragonal iron sulfide FeS from hydrothermal synthesis is superconducting but undergoes no structural change on cooling.

3.2.1 Introduction

Unconventional superconductivity in iron-arsenides and selenides with layered crystal structures and transition temperatures (T_c) up to 56 K in bulk phases^[1-3] or even exciting 100 K in thin FeSe films^[4] triggers enormous interest in the scientific community.^[5-9] One of the most intriguing traits of these materials is that superconductivity coexists or competes with other types of electronic, magnetic, or structural orders that may or may not directly couple to superconductivity.^[10, 11] Most of the iron arsenides, among them LaOFeAs and BaFe₂As₂, traverse tetragonal-to-orthorhombic phase transitions accompanied by antiferromagnetic order.^[12, 13] Superconductivity emerges during suppression of the magnetic order by doping or pressure and the highest critical temperatures occur in the undistorted tetragonal phases. Such a structural transition also occurs in the iron chalcogenide FeSe with tetragonal *anti*-PbO type structure,^[14] but no magnetic order

follows. This was quite surprising since magnetism was believed to be the driving force for the lattice distortion in iron arsenides (spin-nematic),^[15, 16] and moreover, magnetic fluctuations were considered as important for the formation of the Cooper pairs. Recent studies conclude that the structural transition in FeSe has no magnetic origin but is a consequence of orbital ordering (orbital-nematic)^[16] with an unequal occupation of the iron $3d_{xz}/3d_{yz}$ orbitals.^[17, 18] The latest results suggest that orbital ordering and superconductivity compete in FeSe at low temperatures.^[17] Thus superconducting, orbital and structural order parameters are uniquely intertwined and display the signature of unconventional superconductivity in FeSe. This is in line with the fact that the relatively low T_c of 8 K in pure FeSe strongly increases under pressure to 36 K and by intercalation with molecular^[19] or other species to 43 K.^[20, 21]

Recently Lai *et al.* reported that also the iron sulfide FeS with *anti*-PbO structure (mackinawite) is superconducting at 5 K if synthesized by a hydrothermal process.^[22] So far all efforts made to pursue superconductivity in FeS from conventional synthesis failed. However, the complexity of the Fe-S phase diagram makes the synthesis of stoichiometric FeS difficult. Contrary to FeSe, several polymorphs of FeS are known,^[23, 24] where the mackinawite is of near FeS composition (Fe_{1+x}S , where $0 < x < 0.07$).^[25-27] Thus, one might assume that only the low-temperature hydrothermal process used by Lai *et al.* produces stoichiometric FeS which is not accessible by conventional high-temperature routes.

Given the above scenario of FeSe the question arises, whether superconductivity in FeS also occurs in an orthorhombic phase as in the selenide. This would be a strong hint to unconventional pairing, and thus to the potential of FeS to exhibit much higher critical temperatures upon intercalation or other chemical modification. The unexpected observation of superconductivity in iron sulfide motivated us to study the low-temperature crystal structures of both FeSe and FeS synthesized under mild hydrothermal conditions.

3.2.2 Experimental details

Hydrothermal synthesis of FeX (X = Se, S) was carried out using 1.0 mmol elementary iron (55.8 mg) and selenium (79.0 mg) respectively thiourea (76.2 mg) as starting materials.

For the synthesis of FeSe, 110 mg (2.91 mmol) NaBH_4 was added as reducing agent and 700 mg (12.5 mmol) KOH as mineralizer. FeS was synthesized using 733 mg (18.3 mmol)

NaOH as mineralizer and only 5.0 mg (0.13 mmol) NaBH_4 as additional reducing agent due to the reducing impact of thiourea.

The educts were mixed with distilled water (20 respectively 5 mL), sealed in a teflon-lined steel autoclave (50 mL) under argon atmosphere and heated at 150 °C for 8–13 days. The obtained black precipitates were collected by centrifugation and washed with distilled water and ethanol. During this washing step small amounts of unreacted Fe can be removed applying a magnetic field. The samples were dried at room temperature under dynamic vacuum and stored in a purified argon atmosphere glove box.

For conventional solid-state reaction method stoichiometric amounts of Fe and Se were heated under argon atmosphere for 48 h at 700 °C and 10 days at 320 °C.

3.2.3 Results and discussion

Fig. 1 shows the X-ray powder pattern of FeSe obtained by hydrothermal reaction method, referred to as $\text{FeSe}_{\text{hydro}}$ in the following. The Rietveld-analysis was carried out using the structural model of *anti*-PbO type FeSe. No impurity phases occur within the experimental limits ($\sim 1\%$ of a crystalline phase). Chemical analysis by ICP-AAS confirmed the stoichiometry $\text{Fe}_{1.02(1)}\text{Se}$ and $\text{Fe}_{1.01(1)}\text{Se}$ for $\text{FeSe}_{\text{hydro}}$ and conventionally synthesized FeSe ($\text{FeSe}_{\text{conv}}$), respectively.

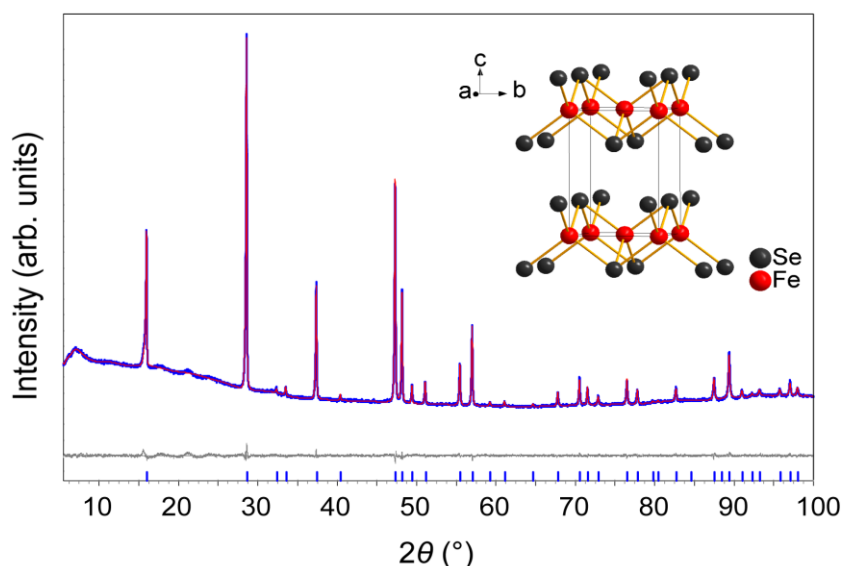


Fig. 1: X-ray powder pattern of FeSe synthesized via hydrothermal reaction method (blue) with Rietveld-fit (red) and difference plot (gray). Inset: Crystal structure of *anti*-PbO type FeSe.

Crystallographic parameters are listed in Tab. 1 together with data for FeSe_{conv}. The lattice parameters and the selenium z positions are mutually the same, thus both crystal structures are absolutely identical from the view of X-ray powder diffraction.

Tab. 1: Crystallographic data of FeX (X = S, Se)

| | <i>FeSe_{hydro}</i> | <i>FeSe_{conv}</i> | <i>FeS_{hydro}</i> |
|---------------------------------------------|-------------------------------------------------------------------------------------------------------------------------------------------------------------------------------------------------------------------------------------------------------|----------------------------|----------------------------|
| Space group | <i>P4/nmm</i> (No. 129, 02) | | |
| <i>a</i> /pm | 377.11(1) | 377.09(1) | 368.18(1) |
| <i>c</i> /pm | 552.14(1) | 552.16(1) | 502.97(2) |
| Volume /nm ³ | 0.07852(1) | 0.07852(1) | 0.06818(1) |
| Positions | 2 Fe at 2 <i>a</i> (³ / ₄ , ¹ / ₄ ,0) 2 Se(S) at 2 <i>c</i> (¹ / ₄ , ¹ / ₄ , <i>z</i>) <i>z</i> = 0.2672(2) <i>z</i> = 0.2669(2) <i>z</i> = 0.262(1) | | |
| Phase fractions (/wt%) and <i>R</i> -values | | | |
| Fe <i>X</i> _(PbO-type) | 100 | 93.6 | 100 |
| Fe <i>X</i> _(NiAs-type) | 0 | 6.4 | 0 |
| <i>R</i> _{wp} | 1.21 | 1.01 | 1.81 |
| <i>R</i> _{exp} | 1.09 | 0.85 | 1.22 |
| χ ² | 1.11 | 1.19 | 1.49 |
| Atomic distances (/pm) and angles (/deg) | | | |
| Fe–Fe | 266.66(1) × 4 | 266.64(1) × 4 | 260.3(1) × 4 |
| Fe– <i>X</i> | 239.31(3) × 4 | 239.40(3) × 4 | 226.5(3) × 4 |
| <i>X</i> –Fe– <i>X</i> | 103.93(1) × 2 | 103.97(1) × 2 | 108.8(1) × 2 |
| | 112.31(1) × 4 | 112.29(1) × 4 | 109.8(1) × 4 |

The AC-susceptibilities of the FeSe samples are surprisingly different (Fig. 2). While the expected bulk superconductivity occurs near 8 K in the conventionally synthesized sample, only traces of superconductivity are visible in the sample from hydrothermal synthesis. Since no differences in composition or structure were detected at room temperature, next we have determined the low-temperature crystal structures.

Fig. 3 shows the temperature dependency of the lattice parameters. The structural transition from tetragonal (*P4/nmm*) to orthorhombic (*Cmme*) symmetry occurs near 90 K in FeSe_{conv} in good agreement with the published data.^[28, 29] The transition temperature is significantly lower in the hydrothermally synthesized sample, where the lattice parameters split near 60 K.

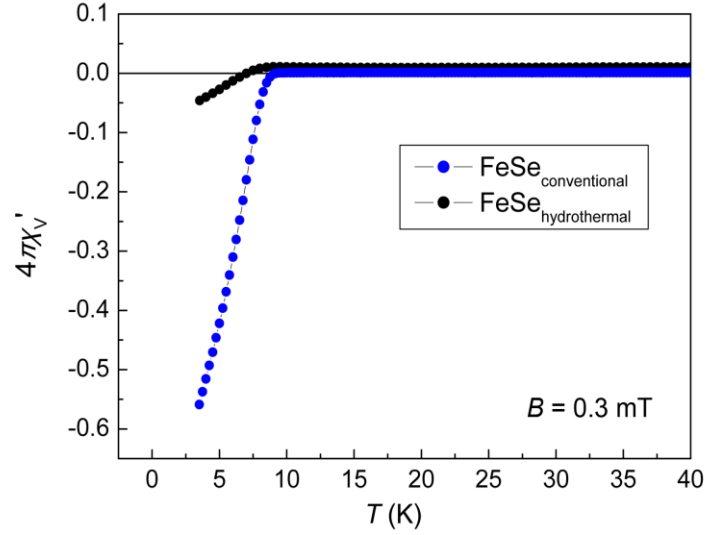


Fig. 2: Low-temperature AC-susceptibility of FeSe samples obtained by conventional (blue) and by hydrothermal synthesis (black).

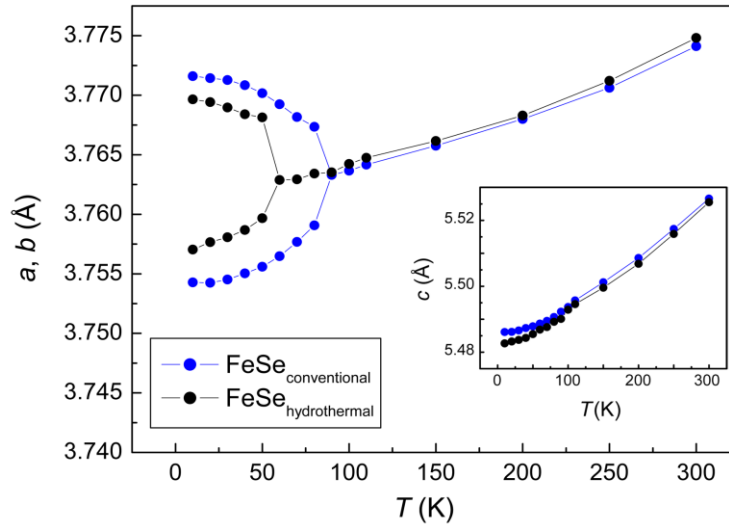


Fig. 3: Temperature dependency of the lattice constants in FeSe synthesized via hydrothermal (black) and conventional (blue) reaction method, respectively. The a and b lattice constants are divided by $\sqrt{2}$ at temperatures below the tetragonal-to-orthorhombic phase transition.

A detailed inspection of the diffraction pattern reveals a less symmetric splitting of the reflections in FeSe_{hydro}. Fig. 4 shows profiles of the (220) Bragg reflection of the tetragonal phase that splits into (400) and (040) during the phase transition. Their intensities have to be equal if the structure is orthorhombic, which is true for FeSe_{conv} but not for FeSe_{hydro}. This

means that the low-temperature structure of hydrothermally synthesized FeSe is different from the known $Cmme$ structure and has lower lattice symmetry.

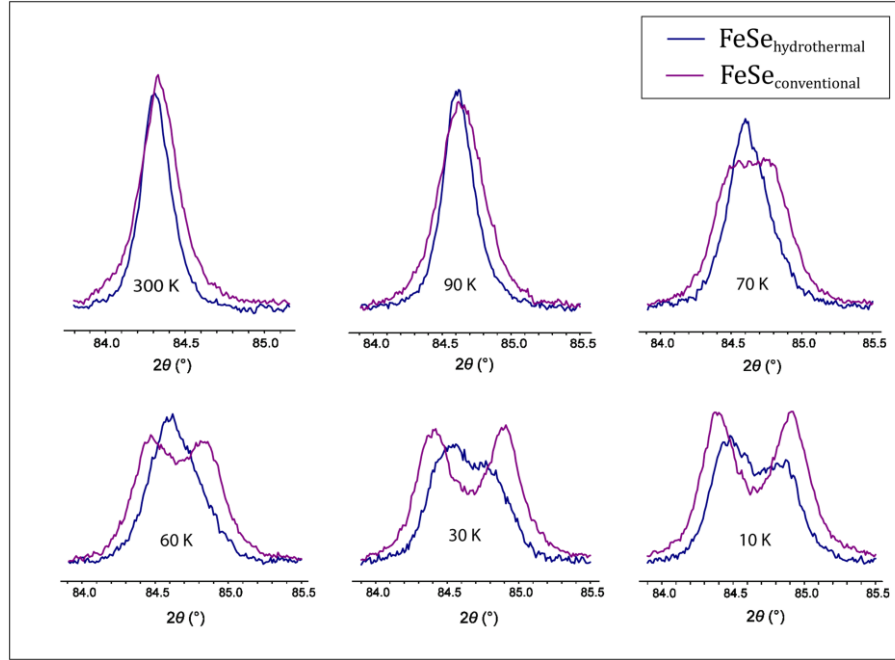


Fig. 4: Temperature evolution of the $(220)_t$ Bragg reflection splitting into a doublet $[(040)_o, (400)_o]$ for FeSe synthesized via hydrothermal (blue) and conventional (magenta) reaction method, respectively.

The Rietveld refinement suggests a triclinic crystal structure ($P\bar{1}$) at 10 K with lattice parameters $a = 376.59(2)$ pm, $b = 376.66(2)$ pm and $c = 547.93(1)$ pm. The α angle remains close to 90° ($90.024(4)^\circ$), β and γ alter into $89.943(4)^\circ$ and $90.168(2)^\circ$, respectively.

Thus the resulting crystal structure differs significantly from superconducting FeSe_{conv} and exhibits another distortion motif of the iron atoms, depicted in Fig. 5. In the known orthorhombic low-temperature structure, iron atoms form stripes running along the shorter axis. The four identical Fe–Fe bonds in the tetragonal phase split into two slightly shorter (265.9 pm) and two longer ones (267.2 pm),^[30] however, this difference is rather small. In the new structure of hydrothermally synthesized non-superconducting FeSe_{hydro} we observe iron atoms in zigzag-chains with short Fe–Fe bonds (256.9(2), 257.7(2) pm), while the distances between neighboring chains become long (275.2(2) pm, 276.0(2) pm). Thus the structural transition in FeSe_{hydro} leads to significantly enhanced Fe–Fe bonds in the zigzag chains, while the distortion in FeSe_{conv} is much weaker and the Fe–Fe bonds remain longer.

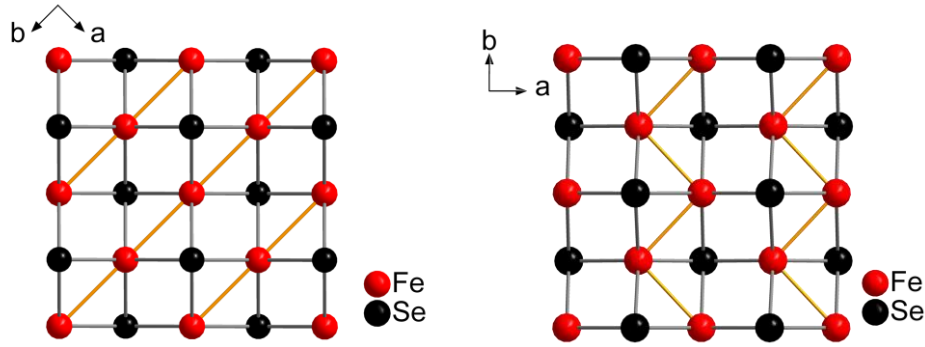


Fig. 5: Low-temperature phase of FeSe synthesized via conventional (left) and hydrothermal (right) method. Iron stripes respectively iron zigzag chains are formed by short and large Fe–Fe distances.

These intriguing different crystal structures may be the reason for the absence of superconductivity in hydrothermally prepared FeSe. Currently it is accepted that the tiny distortion of FeSe_{conv} is a result of orbital ordering, which is believed to be related to superconductivity.^[17] From our results we suggest that the stronger distortion in FeSe_{hydro} is rather driven by Fe–Fe bond formation, which may suppress superconductivity. However, even if the absence of superconductivity may finally be traced back to the different crystal structure, it remains unclear why the obviously identical room temperature FeSe phases transform to different low-temperature structures.

If superconductivity in FeSe only occurs in the orthorhombic phase, the question arises if this is also the case in the newly discovered superconducting FeS. We have synthesized the iron sulfide using a similar hydrothermal procedure recently described by Lai *et al.*^[31] X-ray powder diffraction revealed single-phase samples of FeS with *anti*-PbO type structure. The lattice parameters $a = 368.18(1)$ pm and $c = 502.97(2)$ pm are in good agreement with those reported in literature.^[32–35] Additional X-ray single-crystal analysis confirms the tetragonal structure (see Tab. 1 in chapter 8.1). Our samples show superconductivity at 4.5–5 K (Fig. 6). As elucidated by Lai *et al.*, the high crystallinity and high structural stability of the samples play a crucial role in the observation of superconductivity. Hydrothermal conditions turned out to be perfectly convenient to realize high quality FeS in a simple synthesis.

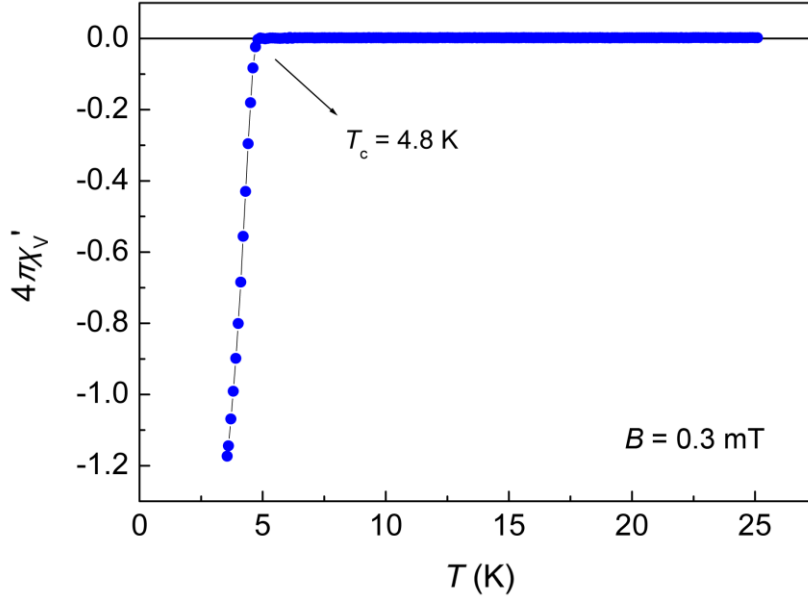


Fig. 6: Low-temperature AC-susceptibility of FeS.

Fig. 7 shows the temperature dependencies of the lattice parameters. As expected the unit cell decreases upon cooling, visible in a decline of the lattice parameters a and c . This progress proceeds without any appreciable anomalies. No characteristic broadening or splitting of the reflections is observed down to 10 K.

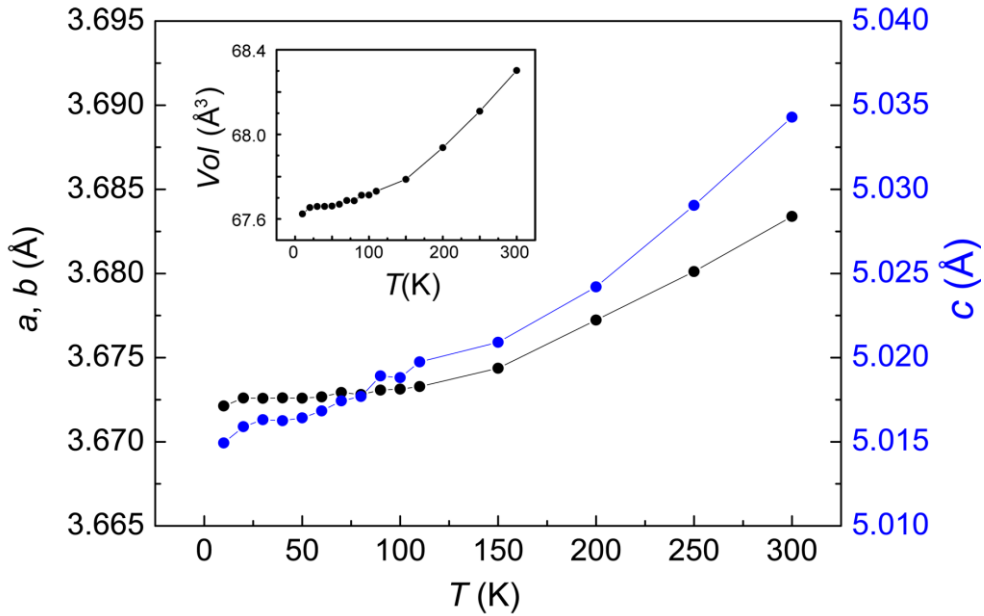


Fig. 7: Lattice parameters and unit cell volume (inset) of tetragonal FeS.

Thus, contrary to FeSe, superconductivity in FeS emerges in the tetragonal phase. This is reminiscent of LaOFeP and LaOFeAs. While the phosphide is a conventional superconductor with T_c near 4 K, the arsenide is a parent compound of the high- T_c materials and exhibits magnetic fluctuations as well as a structural distortion. The absence of the latter in FeS may indicate that the iron sulfide may rather be a conventional BCS-type superconductor and thus quite different from the selenide FeSe.

3.2.4 Conclusion

Finally it is intriguing that hydrothermal synthesis under mild conditions yields superconducting FeS but non superconducting FeSe, while the opposite is true for high-temperature solid state methods. While really stoichiometric FeS is probably only accessible by the hydrothermal method due to the complex phase diagram, we currently have no explanation for the surprising differences of the structures and properties between the FeSe samples at low temperatures.

3.2.5 References

- [1] D. C. Johnston, *Advances in Physics* **2010**, *59*, 803-1061.
- [2] G. R. Stewart, *Reviews of Modern Physics* **2011**, *83*, 1589-1652.
- [3] D. Johrendt, *Journal of Materials Chemistry* **2011**, *21*, 13726-13736.
- [4] J.-F. Ge, Z.-L. Liu, C. Liu, C.-L. Gao, D. Qian, Q.-K. Xue, Y. Liu, J.-F. Jia, *Nature Materials* **2015**, *14*, 285-289.
- [5] X. H. Chen, T. Wu, G. Wu, R. H. Liu, H. Chen, D. F. Fang, *Nature* **2008**, *453*, 761-762.
- [6] P. Cheng, B. Shen, G. Mu, X. Zhu, F. Han, B. Zeng, H.-H. Wen, *Europhysics Letters* **2009**, *85*, 67003.
- [7] Y. Kamihara, T. Watanabe, M. Hirano, H. Hosono, *Journal of the American Chemical Society* **2008**, *130*, 3296-3297.
- [8] R. H. Liu, G. Wu, T. Wu, D. F. Fang, H. Chen, S. Y. Li, K. Liu, Y. L. Xie, X. F. Wang, R. L. Yang, L. Ding, C. He, D. L. Feng, X. H. Chen, *Physical Review Letters* **2008**, *101*, 087001.
- [9] M. Rotter, M. Tegel, D. Johrendt, *Physical Review Letters* **2008**, *101*, 107006.
- [10] R. M. Fernandes, J. Schmalian, *Physical Review B* **2010**, *82*, 014521.
- [11] R. M. Fernandes, A. V. Chubukov, J. Schmalian, *Nature Physics* **2014**, *10*, 97-104.
- [12] C. de la Cruz, Q. Huang, J. W. Lynn, J. Li, W. R. Li, J. L. Zarestky, H. A. Mook, G. F. Chen, J. L. Luo, N. L. Wang, P. Dai, *Nature* **2008**, *453*, 899-902.

- [13] M. Rotter, M. Tegel, D. Johrendt, I. Schellenberg, W. Hermes, R. Pöttgen, *Physical Review B* **2008**, *78*, 020503.
- [14] T. M. McQueen, A. J. Williams, P. W. Stephens, J. Tao, Y. Zhu, V. Ksenofontov, F. Casper, C. Felser, R. J. Cava, *Physical Review Letters* **2009**, *103*, 057002-057004.
- [15] A. E. Böhmer, C. Meingast, *Comptes Rendus Physique* **2016**, *17*, 90-112.
- [16] W. Zhentao, H. N. Andriy, *Journal of Physics: Condensed Matter* **2015**, *27*, 225602.
- [17] S. H. Baek, D. V. Efremov, J. M. Ok, J. S. Kim, J. van den Brink, B. Büchner, *Nature Materials* **2015**, *14*, 210-214.
- [18] T. Shimojima, Y. Suzuki, T. Sonobe, A. Nakamura, M. Sakano, J. Omachi, K. Yoshioka, M. Kuwata-Gonokami, K. Ono, H. Kumigashira, A. E. Böhmer, F. Hardy, T. Wolf, C. Meingast, H. v. Löhneysen, H. Ikeda, K. Ishizaka, *Physical Review B* **2014**, *90*, 121111.
- [19] M. Burrard-Lucas, D. G. Free, S. J. Sedlmaier, J. D. Wright, S. J. Cassidy, Y. Hara, A. J. Corkett, T. Lancaster, P. J. Baker, S. J. Blundell, S. J. Clarke, *Nature Materials* **2013**, *12*, 15-19.
- [20] U. Pachmayr, F. Nitsche, H. Luetkens, S. Kamusella, F. Brückner, R. Sarkar, H.-H. Klauss, D. Johrendt, *Angewandte Chemie International Edition* **2015**, *54*, 293-297.
- [21] U. Pachmayr, D. Johrendt, *Chemical Communications* **2015**, *51*, 4689-4692.
- [22] X. Lai, H. Zhang, Y. Wang, X. Wang, X. Zhang, J. Lin, F. Huang, *Journal of the American Chemical Society* **2015**, *137*, 10148-10151.
- [23] A. R. Lennie, S. A. T. Redfern, P. F. Schofield, D. J. Vaughan, *Mineralogical Magazine* **1995**, *59*, 677-683.
- [24] S. D. Scott, in *Short Course Notes, Sulfide Mineralogy*, **1974**, pp. CS21-CS29.
- [25] W. Davison, *Aquatic Sciences* **1991**, *53*, 309-329.
- [26] A. R. Lennie, S. A. T. Redfern, P. E. Champness, C. P. Stoddart, P. F. Schofield, D. J. Vaughan, *American Mineralogist* **1997**, *82*, 302-309.
- [27] D. J. Vaughan, J. R. Craig, in *Mineral chemistry of metal sulfides*, Cambridge University Press, **1978**.
- [28] S. Margadonna, Y. Takabayashi, M. T. McDonald, K. Kasperkiewicz, Y. Mizuguchi, Y. Takano, A. N. Fitch, E. Suard, K. Prassides, *Chemical Communications* **2008**, *43*, 5607-5609.
- [29] T. M. McQueen, A. J. Williams, P. W. Stephens, J. Tao, Y. Zhu, V. Ksenofontov, F. Casper, C. Felser, R. J. Cava, *Physical Review Letters* **2009**, *103*, 057002.
- [30] K. Horigane, H. Hiraka, K. Ohoyama, *Journal of the Physical Society of Japan* **2009**, *78*, 074718.
- [31] X. Lai, H. Zhang, Y. Wang, X. Wang, X. Zhang, J. Lin, F. Huang, *Journal of the American Chemical Society* **2015**, *137*, 10148-10151.

-
- [32] S. J. Denholme, S. Demura, H. Okazaki, H. Hara, K. Deguchi, M. Fujioka, T. Ozaki, T. Yamaguchi, H. Takeya, Y. Takano, *Materials Chemistry and Physics* **2014**, *147*, 50-56.
- [33] S. J. Denholme, H. Okazaki, S. Demura, K. Deguchi, M. Fujioka, T. Yamaguchi, H. Takeya, M. ElMassalami, H. Fujiwara, T. Wakita, T. Yokoya, Y. Takano, *Science and Technology of Advanced Materials* **2014**, *15*, 055007.
- [34] Z. Shu-Lin, W. Hui-Xian, D. Cheng, *Chinese Physics B* **2014**, *23*, 087203.
- [35] I. T. Sines, D. D. Vaughn, R. Misra, E. J. Popczun, R. E. Schaak, *Journal of Solid State Chemistry* **2012**, *196*, 17-20.

3.3 The solid-solution FeSe_{1-x}S_x prepared via hydrothermal synthesis

3.3.1 Introduction

The *anti*-PbO type superconductor FeSe shows a strong increase of T_c from 8 to 37 K under high physical pressure of 9 GPa.^[1] Substitution of atoms by smaller respectively larger ones in the crystal structure can lead to similar effects via so called chemical pressure. Mizuguchi *et al.* investigated the substitution of sulfur ($r(S^{2-}) = 184$ pm^[2], $r(Se^{2-}) = 198$ pm^[2], positive chemical pressure) and tellurium ($r(Te^{2-}) = 221$ ppm^[2], negative chemical pressure) for selenium in FeSe.^[3] FeSe_{1-x}Te_x which can be prepared for the entire substitution range via conventional solid state reaction shows an increase of T_c for $x \leq 0.75$ despite the negative pressure effect. In contrast, Fe_{1.1}Te is not superconducting. The analogous substitution by sulfur enlarges T_c for $x \leq 0.3$ before it decreases for $x \geq 0.3$. However, the authors report a solubility limit of sulfur in FeSe_{1-x}S_x at $x = 0.3$. Both substitutions also enhance the superconducting volume fractions, which might indicate that the substitution of S and Te for Se stabilizes superconductivity.^[3]

In contrast to the solubility limit observed for the solid state reaction of FeSe_{1-x}S_x, the hydrothermal synthesis of superconducting *anti*-PbO type FeS was reported recently.^[4] An improvement of the accessibility with regard to samples with higher sulfur contents seems thus feasible by applying hydrothermal synthesis method, and is examined in this chapter. Thereby, the stabilization of superconductivity which was observed for the substituted compounds from solid state reaction might apply as well for hydrothermally prepared samples. FeSe prepared via hydrothermal reaction shows only traces of superconductivity in contrast to bulk superconducting FeS. The possible re-emergence of superconductivity in hydrothermally prepared FeSe by substitution of S for Se as well as the concomitant evolution of T_c is subject of this chapter.

3.3.2 Experimental details

Hydrothermal synthesis of FeSe_{1-x}S_x ($0 \leq x \leq 1$) was carried out using 1.0 mmol iron (56 mg), selenium and thiourea in respective amounts (see below), 0.30 g (7.9 mmol) NaBH₄ as reducing agent and 0.50 g (8.9 mmol) KOH as mineralizer. The educts were mixed with distilled water (20 mL), sealed in a teflon-lined steel autoclave (50 mL) under argon atmosphere and heated at 155 °C for 6–15 days. The obtained black precipitates were collected by centrifugation and washed with distilled water and ethanol. During this

washing step small amounts of unreacted Fe can be removed with a magnet. The samples were dried at room temperature under dynamic vacuum and stored in a purified argon atmosphere glove box.

3.3.3 Results and discussion

Fig. 1 gives an overview of some X-ray powder patterns of samples of the solid solution $\text{FeSe}_{1-x}\text{S}_x$, which was successfully prepared for the whole substitution range $0 \leq x \leq 1$. The composition of all compounds was determined by Rietveld refinement of the respective X-ray powder pattern and confirmed by EDX measurements.

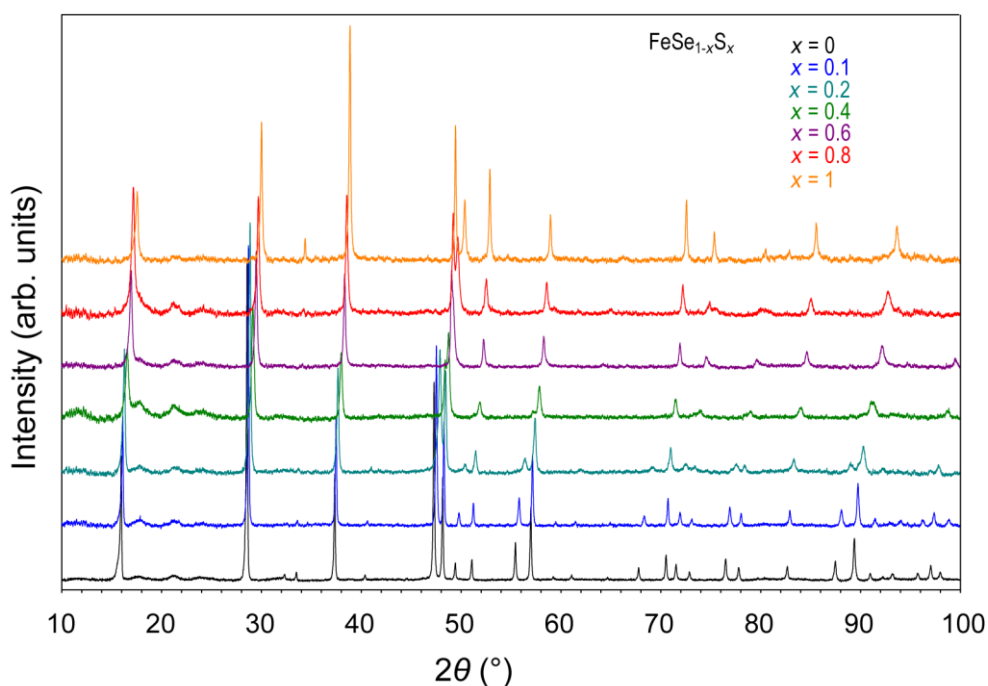


Fig. 1: X-ray powder patterns of $\text{Fe}(\text{Se}_{1-x}\text{S}_x)$ ($0 \leq x \leq 1$).

Interestingly, the incorporation of selenium in the structure is favored over that of sulfur. In Fig. 2, the sulfur content from Rietveld refinement of the obtained samples is depicted depending on the relative amount of sulfur applied in the syntheses. The data illustrates that an excess of sulfur, respectively thiourea, has to be used.

The chemical pressure induced by partially substituting selenium by smaller sulfur atoms leads to a reduction of both lattice parameters and thus also the cell volume (Fig. 3). Hereby, all three parameters decrease linearly with increasing sulfur content indicating

homogeneous substitution. While a decreases only by 2.4 %, c is reduced by 8.9 %, which results in a continuous decrease of c/a as well.

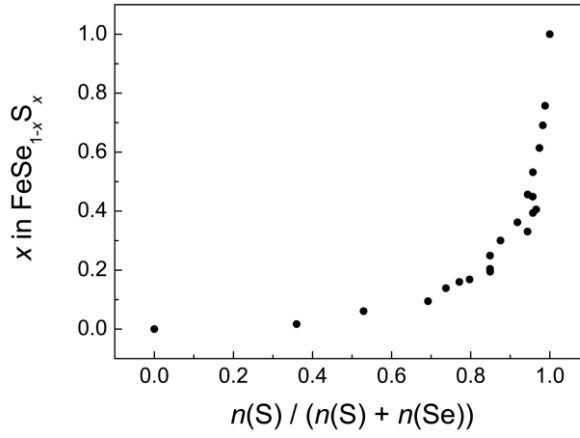


Fig. 2: Amount of sulfur incorporation dependent on the relative amount of sulfur used. $n(\text{S})$ and $n(\text{Se})$ is the molar amount of applied sulfur respectively selenium in the syntheses.

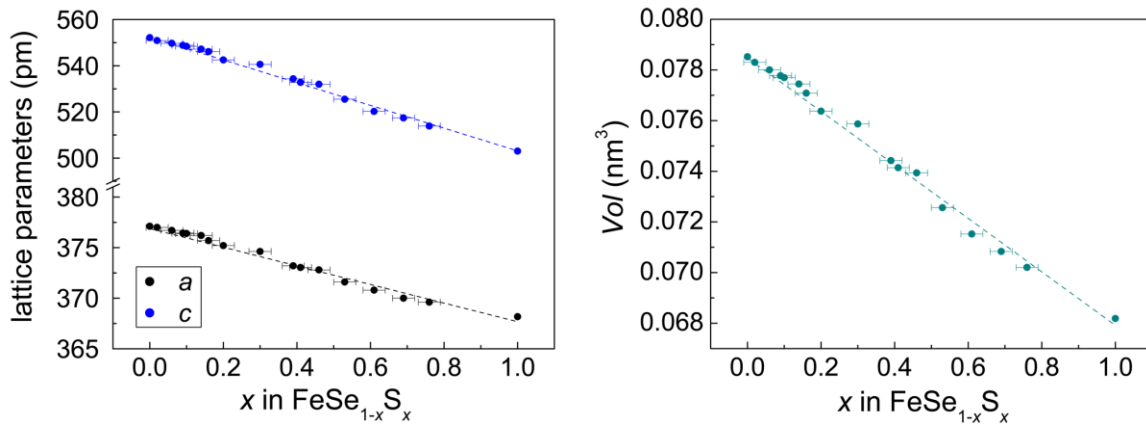


Fig. 3: Lattice parameters (left) and unit cell volume (right) of $\text{FeSe}_{1-x}\text{S}_x$ as a function of the sulfur content x .

This compression of the unit cell along c is associated with a flattening of the $\text{FeSe}_{1-x}\text{S}_x$ tetrahedra. Fig. 4 shows the $\text{Fe}-(\text{Se}/\text{S})$ distance as well as the twofold and fourfold tetrahedral angles as a function of the sulfur content. With increasing amount of sulfur, the iron-chalcogenide bond length decreases as expected, which in turn results in a continuous approach of the tetrahedral angles towards the ideal one of 109.47° .

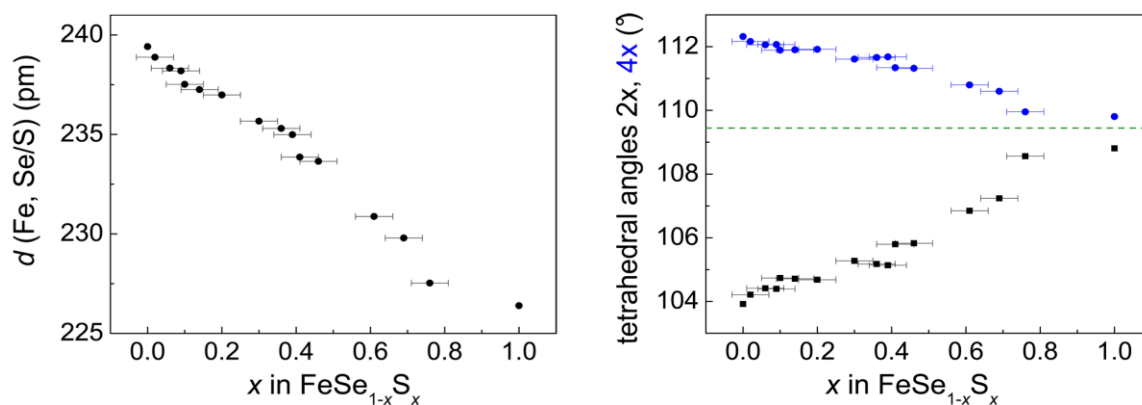


Fig. 4: Fe–(Se/S) distance d (left) and tetrahedral angles (right) of $\text{FeSe}_{1-x}\text{S}_x$ as a function of the sulfur content x . The green line represents the ideal tetrahedral angle of 109.47° .

Along with these unit cell changes, the morphology of the crystals changes as well. Where FeSe crystallizes in rod shaped particles, the crystals show a more and more flake like morphology with increasing sulfur content (Fig. 5). The particles of FeS are more than one magnitude larger than those of the rest of the solid-solution for comparable heating times.

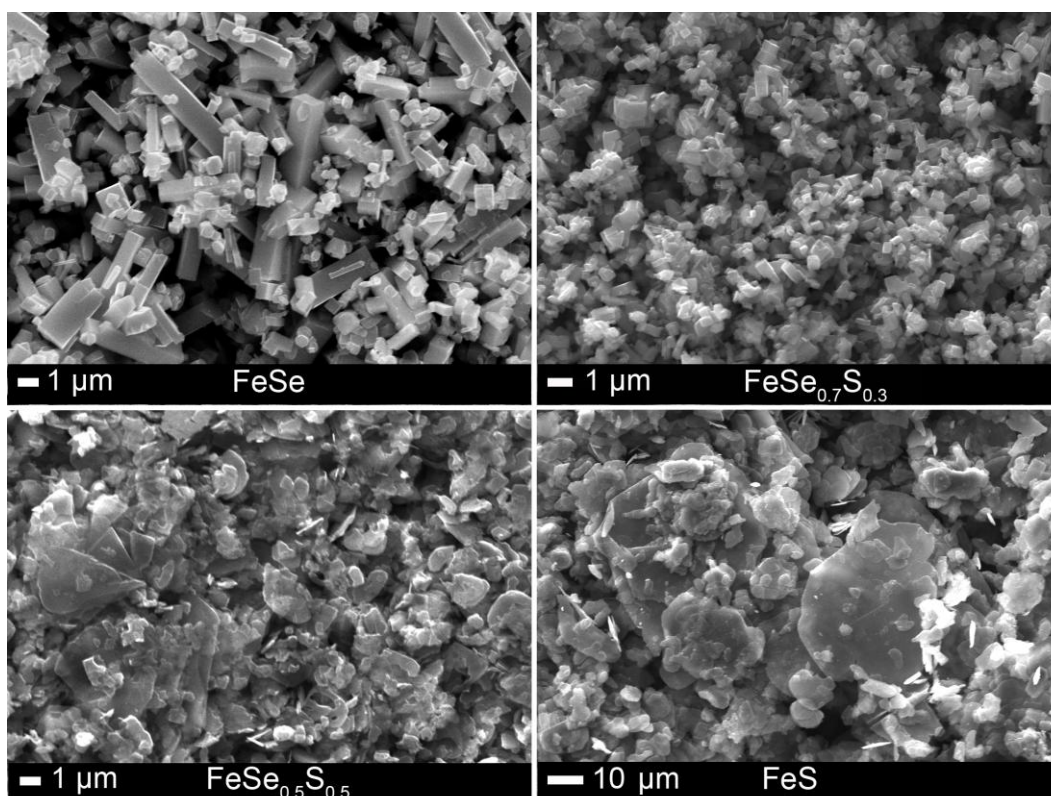


Fig. 5: SEM images of samples FeSe (top, left), $\text{FeSe}_{0.7}\text{S}_{0.3}$ (top, right), $\text{FeSe}_{0.5}\text{S}_{0.5}$ (bottom, left) and FeS (bottom, right). Note that the scale for FeS is about 10 times larger.

Susceptibility measurements reveal that hydrothermally prepared $\text{FeSe}_{1-x}\text{S}_x$ exhibits bulk superconductivity only for $x = 1$. In Fig. 6 the volume susceptibility of some samples $0 \leq x < 1$ shows only traces of superconductivity. The partial substitution of Se by S does not lead to a re-emergence of bulk superconductivity. This is in contrast to the stabilization of superconductivity observed for the substituted compounds prepared via solid state reaction. It seems that tiny differences in the hydrothermal reaction conditions induced by the necessarily different educts decide on the emergence respectively absence of superconductivity. Bulk superconductivity is solely observed for the synthesis conditions of the pure sulfur compound. However, the underlying differences of $\text{FeSe}_{1-x}\text{S}_x$ for $x = 1$ versus $0 \leq x < 1$ remain unclear. Possibly, slight changes in reduction potential or pH value cause vacancies, distortions or interstitial atoms in the crystal structure. These changes are most likely too weak to be detected by the standard analytical methods.

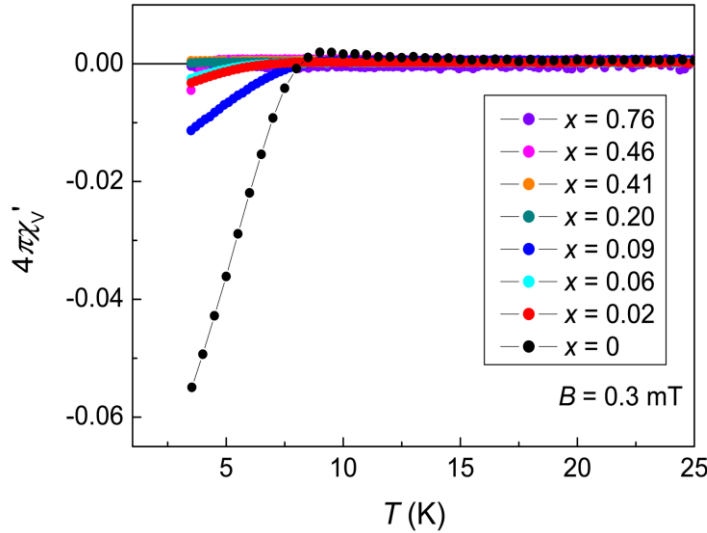


Fig. 6: AC-susceptibility of $\text{FeSe}_{1-x}\text{S}_x$.

An explanation based on the different particle sizes can be discussed as well. When a superconductor is cooled below its transition temperature, external magnetic fields are excluded (Meissner effect). However, the field is not completely absent but decays exponentially from the surface. This characteristic length is called the London penetration depth λ_L and is related to the density of superconducting electrons in the material.^[5] For particles with radii smaller than λ_L , this penetrating magnetic field brings significant changes to the observed Meissner effect.^[6, 7] Isolated lead nanoparticles of 11 nm diameter for example show a reduction in the signal amplitude by 5×10^4 times ($\lambda_L = 37$ nm).^[8]

For FeSe, the London penetration depth at $T = 0$ was determined to about 450 nm.^[9] The crystallites of $\text{FeSe}_{1-x}\text{S}_x$ with $0 \leq x < 1$ are in the magnitude of roughly 0.5–3 μm , thus a significant percentage of the crystallites' volume would come within this region of decaying magnetic field. However, it must be considered that the particles are not isolated from each other in the present samples. In a bulk superconductor the magnetic field is excluded from the entire volume of the sample except for a surface layer of the thickness λ_L . Thus, the small size of the single crystallites of $\text{FeSe}_{1-x}\text{S}_x$ for $0 \leq x < 1$ can be excluded as reason for the small diamagnetic signals as bulk samples were employed for the measurements.

The different particle sizes and physical properties of $\text{FeSe}_{1-x}\text{S}_x$ for $x = 1$ respectively $0 \leq x < 1$ might be related to different growth processes. Samples with $0 \leq x < 1$ show either particles of $\text{FeSe}_{1-x}\text{S}_x$ or residual particles of pure Fe. Fig. 7A depicts a bisected residual Fe particle from a FeSe synthesis as well as the corresponding EDX mapping of Fe and/or Se.

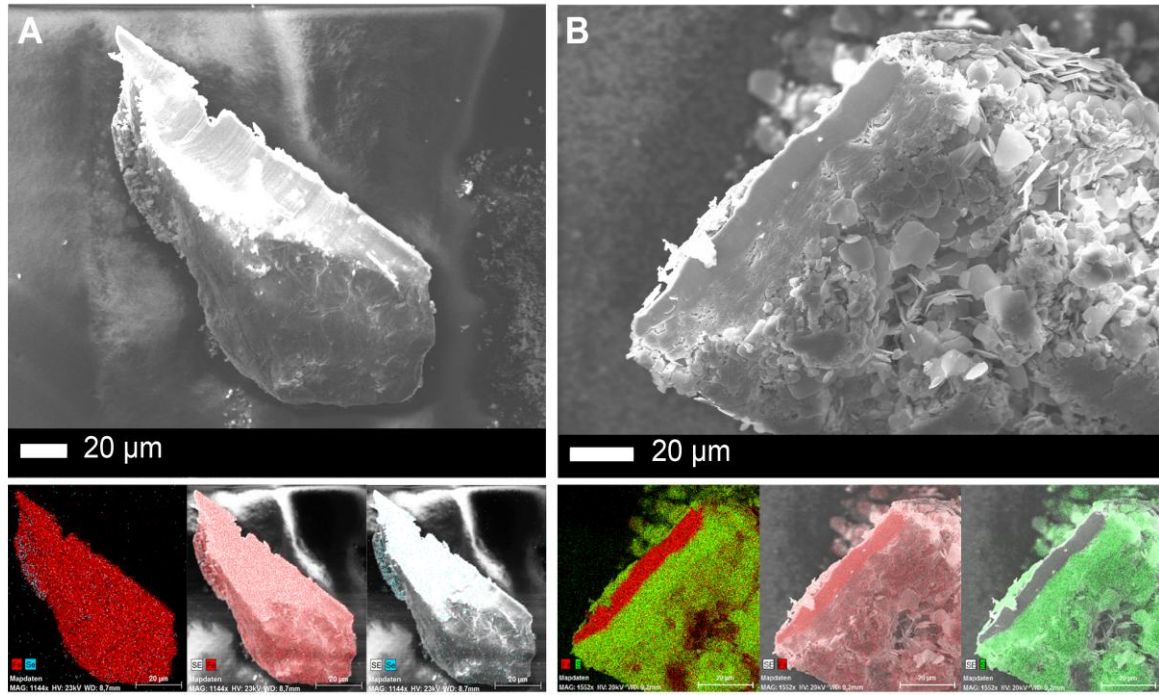


Fig. 7: A: SEM image of the cutting edge of a Fe particle from FeSe synthesis (top). EDX mapping of Fe (red) and Se (blue) (bottom, left), Fe (bottom, center) and Se (bottom, right), respectively. B: SEM image of the cutting edge of a Fe particle with FeS shell from FeS synthesis (top). EDX mapping of Fe (red) and S (green) (bottom, left), Fe (bottom, center) and S (bottom, right), respectively.

For FeS, the iron particles beside pure FeS are all covered by a shell of FeS platelets as illustrated in Fig. 7B. The figure shows the cutting edge of a bisected particle in a SEM image. The distribution of Fe and S reveals that the particle is built of an iron core which is surrounded by a shell of FeS platelets. Apparently, FeS grows directly on the surface of the Fe educt particles. For $\text{FeSe}_{1-x}\text{S}_x$ with $0 \leq x < 1$ a mechanism where most of the elementary iron dissolves first under oxidation seems more plausible.

3.3.4 Conclusion

Hydrothermally prepared $\text{FeSe}_{1-x}\text{S}_x$ with $0 \leq x \leq 1$ is bulk superconducting only for $x = 1$. The superconducting FeS exhibits particles, which are more than one magnitude larger than those of the rest of the solid-solution. However, these different sizes of the crystallites $\text{FeSe}_{1-x}\text{S}_x$ can be excluded as reason for the decisive reduction of the superconducting volume fraction as bulk samples were employed for the measurements. Slight differences in the detailed crystal structure, for example vacancies, distortions or interstitial atoms could rather be the reason for the absence of superconductivity. The examination of residual magnetic particles gives indication of different growth processes for non-superconducting and superconducting samples.

3.3.5 References

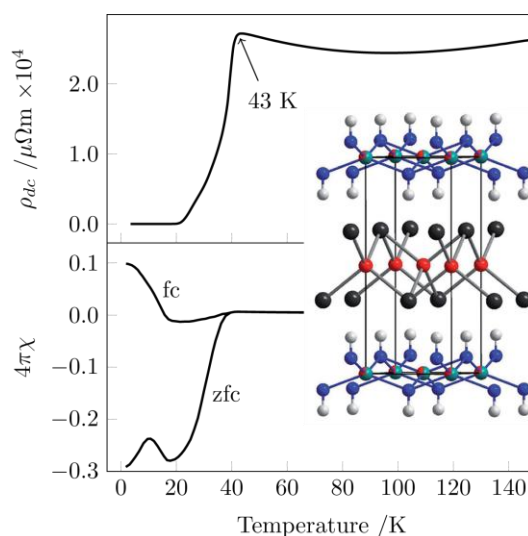
- [1] S. Medvedev, T. M. McQueen, I. A. Troyan, T. Palasyuk, M. I. Eremets, R. J. Cava, S. Naghavi, F. Casper, V. Ksenofontov, G. Wortmann, C. Felser, *Nature Materials* **2009**, 8, 630-633.
- [2] R. Shannon, *Acta Crystallographica Section A* **1976**, 32, 751-767.
- [3] Y. Mizuguchi, F. Tomioka, S. Tsuda, T. Yamaguchi, Y. Takano, *Journal of the Physical Society of Japan* **2009**, 78, 074712.
- [4] X. Lai, H. Zhang, Y. Wang, X. Wang, X. Zhang, J. Lin, F. Huang, *Journal of the American Chemical Society* **2015**, 137, 10148-10151.
- [5] F. London, H. London, *Proceedings of the Royal Society of London. Series A - Mathematical and Physical Sciences* **1935**, 149, 71-88.
- [6] W. Buckel, R. Kleiner, *Superconductivity. Fundamentals and Applications, Vol. 6*, Wiley-VCH, Weinheim, **2004**.
- [7] Y. L. Zuev, E. D. Specht, C. Cantoni, D. K. Christen, J. R. Thompson, R. Jin, A. S. Sefat, D. G. Mandrus, M. A. McGuire, B. C. Sales, *Physical Review B* **2009**, 79, 224523.
- [8] P. Zolotavin, P. Guyot-Sionnest, *ACS Nano* **2010**, 4, 5599-5608.

- [9] M. Abdel-Hafiez, J. Ge, A. N. Vasiliev, D. A. Chareev, J. Van de Vondel, V. V. Moshchalkov, A. V. Silhanek, *Physical Review B* **2013**, *88*, 174512.

4 The layered lithium iron chalcogenide hydroxide $[(\text{Li}_{0.8}\text{Fe}_{0.2})\text{OH}]\text{FeX}$ ($X = \text{Se}, \text{S}$)

4.1 Coexistence of 3d-ferromagnetism and superconductivity in $[(\text{Li}_{0.8}\text{Fe}_{0.2})\text{OH}]\text{FeSe}$

Ursula Pachmayr, Fabian Nitsche, Hubertus Luetkens, Sirko Kamusella, Felix Brückner, Rajib Sarkar, Hans-Henning Klauss, and Dirk Johrendt



published in: *Angewandte Chemie International Edition* **2015**, 54, 293-297.

Copyright 2015, Wiley-VCH Verlag GmbH & Co. KGaA, Weinheim.

Abstract

Superconducting $[(\text{Li}_{0.8}\text{Fe}_{0.2})\text{OH}]\text{FeSe}$ was synthesized by hydrothermal methods and characterized by single-crystal and powder X-ray diffraction. The structure contains alternating layers of *anti*-PbO type FeSe and $(\text{Li}_{0.8}\text{Fe}_{0.2})\text{OH}$. Electrical resistivity and magnetic susceptibility measurements reveal superconductivity at 43 K. An anomaly in the diamagnetic shielding indicates ferromagnetic ordering near 10 K while superconductivity is retained. The ferromagnetism is from the iron atoms in the $(\text{Li}_{0.8}\text{Fe}_{0.2})\text{OH}$ layer. Isothermal magnetization measurements confirm the superposition of ferromagnetic and superconducting hysteresis. The internal ferromagnetic field is larger than the lower, but smaller than the upper critical field of the superconductor. The formation of a spontaneous

vortex phase where both orders coexist is supported by ^{57}Fe -Mössbauer spectra, ^7Li -NMR spectra, and μSR experiments.

4.1.1 Introduction

Superconductivity expels magnetic flux from the interior of a solid, while ferromagnetism generates it, thus these phenomena are antagonistic. Moreover, ferromagnetic order is usually detrimental to superconductivity because strong internal fields from aligned moments break Cooper pairs. Nevertheless, both phenomena are not mutually exclusive in all cases. After early investigations of alloys with magnetic rare-earth atoms diluted in superconducting lanthanum metal,^[1] the first superconductors with spatially ordered arrays of magnetic atoms were the metallic molybdenum sulfides REMo_6S_8 (RE = rare earth element), referred to as the Chevrel phases.^[2, 3] Among them, compounds with the strongly magnetic rare-earth elements Tb–Er have superconducting critical temperatures (T_c) around 2 K, and enter magnetically ordered states between 15 mK and 5 mK.^[4, 5] A further example is ErRh_4B_4 where ferromagnetism destroys superconductivity at 1 K, while co-existence with antiferromagnetic ordering has been found in the borocarbides $\text{RENi}_2\text{B}_2\text{C}$ ^[6, 7] and the ruthenate $\text{RuSr}_2\text{GdCu}_2\text{O}_8$.^[8] Recently, the co-existence of superconductivity and ferromagnetic ordering of Eu^{2+} ions in the iron arsenides $\text{EuFe}_2(\text{As}_{1-x}\text{P}_x)_2$ and $\text{Eu}(\text{Fe}_{1-x}\text{Ru}_x)_2\text{As}_2$ has been reported.^[9-11] Such materials where the ferromagnetic ordering temperature (Curie temperature, T_c) is below T_c are called ferromagnetic superconductors. Therein, both phenomena are usually spatially decoupled, and do not interact directly in the sense that the same electrons are responsible for both. The situation in which the same electrons are responsible for both phenomena is discussed in superconducting ferromagnets with $T_c > T_c$. In these materials the superconducting state emerges in a ferromagnetic metal (usually at mK temperatures), which gives evidence for exotic mechanisms, such as spin triplet pairing, for example in UGe_2 or URhGe which have been intensively studied.^[12-14]

To date the extremely low temperatures, as well as the inertness of the rare-earth $4f$ shell hardly allowed chemical manipulation of these quite fascinating phenomena. This would be different if the ferromagnetic ordering emerges from d -elements, where the magnetic state is much more susceptible to the chemical environment. Materials where superconductivity coexists with $3d$ -ferromagnetism in a bulk phase are unknown to our knowledge.^[15, 16] Herein we report the synthesis, crystal structure, and basic physical properties of the

ferromagnetic superconductor $[(\text{Li}_{0.8}\text{Fe}_{0.2})\text{OH}]\text{FeSe}$, in which magnetic ordering emerges from iron ions in the hydroxide layer at 10 K, which is sandwiched between iron selenide layers providing superconductivity up to 43 K.

4.1.2 Experimental details

Polycrystalline samples of $[(\text{Li}_{0.8}\text{Fe}_{0.2})\text{OH}]\text{FeSe}$ were synthesized under hydrothermal conditions using a modified procedure given in Ref. [17]. Iron metal (0.0851 g, 1.524 mmol), Selenourea (0.50 g, 4.1 mmol) and $\text{LiOH}\cdot\text{H}_2\text{O}$ (3 g, 0.1 mol) were mixed with distilled water (10 mL). The starting mixtures were tightly sealed in a teflon-lined steel autoclave (50 mL) and heated at 150 °C for 8 days. The shiny lamellar precipitates obtained were separated by centrifugation, and washed several times with distilled water and ethanol. Afterwards, the polycrystalline products were dried at room temperature under dynamic vacuum and stored at -25 °C under argon atmosphere.

4.1.3 Results and discussion

Fig. 1 shows a scanning electron microscope (SEM) image of the sample and a typical platelike crystal. A small specimen ($50 \times 40 \times 5 \mu\text{m}^3$) was selected for the X-ray single crystal analysis.

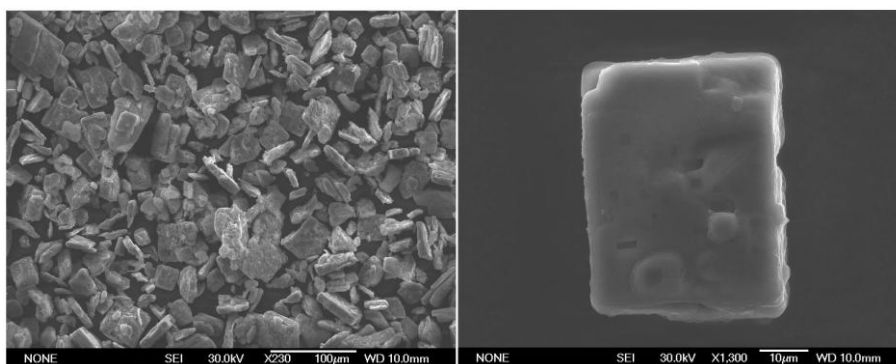


Fig. 1: Left: SEM image of a $[(\text{Li}_{0.8}\text{Fe}_{0.2})\text{OH}]\text{FeSe}$ sample. Right: plate-like single crystal.

First structure refinements using the data of $\text{LiFeO}_2\text{Fe}_2\text{Se}_2$ given by Lu *et al.*[17] as starting parameters were not satisfying. A closer inspection revealed residual electron density at about 75 pm below the oxygen atoms which indicated additional hydrogen. Furthermore the U_{33} component of the thermal displacement ellipsoid at the Fe/Li site was too large,

which required a split position with Li shifted off the center of the oxygen tetrahedra by 40 pm along the c -direction. Attempts to find an ordered model by twinning and/or symmetry reduction failed. Finally we detected a slight deficiency of approximately 8 % at the iron site in the FeSe layer. X-ray diffraction cannot distinguish between iron vacancies or a possible Fe/Li mixed site. Since Li-NMR spectroscopy shows two appropriate Li sites in the structure, we initially interpreted the deficiency as Fe/Li mixing. However, the investigation of further samples clarified that this second signal is rather the result of traces of remaining $\text{LiOH}\cdot\text{H}_2\text{O}$ than a Fe/Li mixed site in the FeSe layer.

Using this model, the structure refinements rapidly converged to small residuals ($R_1 = 0.016$). The crystallographic parameters are compiled in Tab. 1 in chapter 8.2. In the following we denote iron in the hydroxide layer as Fe^a and in the FeSe layer as Fe^b . By using these crystal data we were able to perform a Rietveld fit of the X-ray powder pattern, which revealed the identical structure and confirmed that the sample is free from impurities within the sensitivity of laboratory X-ray powder diffraction ($\sim 1\%$ of a crystalline phase). The crystal structure of $[(\text{Li}_{0.8}\text{Fe}_{0.2})\text{OH}]\text{FeSe}$ is depicted in the inset of Fig. 2.

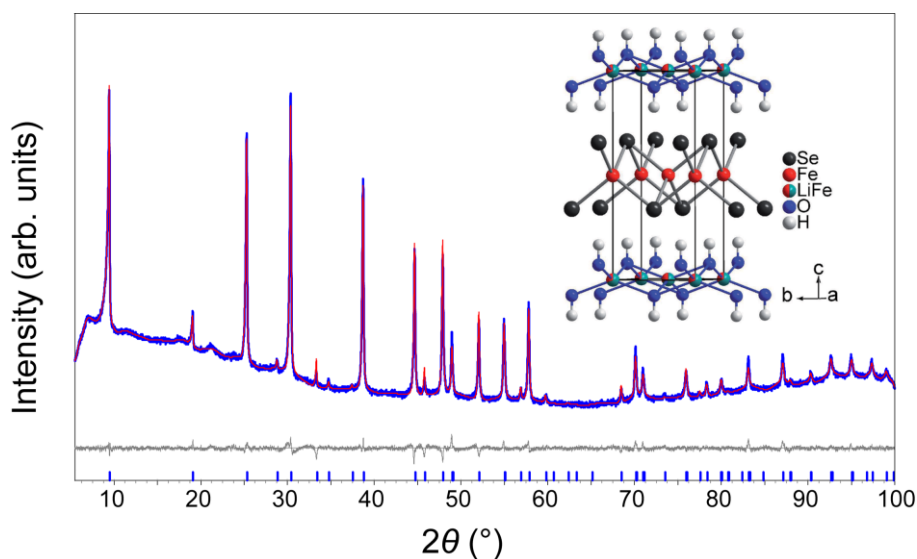


Fig. 2: X-ray powder pattern (blue) with Rietveld-fit (red) and difference curve (gray). Inset: crystal structure of $[(\text{Li}_{0.8}\text{Fe}_{0.2})\text{OH}]\text{FeSe}$.

Along the c -axis *anti*-PbO type layers of lithium-iron-hydroxide alternate with FeSe-layers. Unlike $\text{LiFeO}_2\text{Fe}_2\text{Se}_2$ ^[17] our compound is not an oxide but a hydroxide, where positively polarized hydrogen atoms point towards the negatively polarized selenium of the FeSe

layer. The structure of the $(\text{Li}_{0.8}\text{Fe}_{0.2})\text{OH}$ layer is quite similar to LiOH itself, which likewise crystallizes in the *anti*- PbO -type.^[18]

The Se-Fe-Se bond angles of the FeSe_4 tetrahedra are almost identical to those in binary $\beta\text{-FeSe}$,^[19] while the Fe-Se bond lengths (241.4 pm) are slightly longer than in $\beta\text{-FeSe}$ (239.5 pm). Thus no significant changes apply to the structure of the FeSe layer in $[(\text{Li}_{0.8}\text{Fe}_{0.2})\text{OH}]\text{FeSe}$, however, the tiny elongation of the Fe-Se bonds may already influence the electronic properties. The situation in the hydroxide layer is more difficult. Iron is in a flattened tetrahedron of oxygen atoms with a Fe-O distance of 201.6 pm. This matches the sum of the ionic radii^[20] if iron is Fe^{2+} (203 pm), but not if iron is Fe^{3+} (189 pm). Thus we suggest the presence of Fe^{2+} in the hydroxide layer, even though a tetrahedral coordination is rather unusual. Lithium in the center of the flat oxygen tetrahedron would have Li-O separation of 201.6 pm, significantly longer than the 196 pm in LiOH .^[21] We suggest that this is the reason why Li is shifted along c , however, the Li position is not precise owing to the low scattering power. This is even more the case for the hydrogen atom, where the refined O-H distance is 72(8) pm. Given the large error and the fact that X-H bond lengths from X-ray diffraction are usually underestimated by at least 10 %, we are not that far from the O-H distance in LiOH which was determined to be 89 pm using neutron diffraction.^[18]

The composition obtained from X-ray diffraction is $[(\text{Li}_{0.795(5)}\text{Fe}_{0.205(5)})\text{OH}]\text{Fe}_{0.922(3)}\text{Se}$. However, the true errors of the stoichiometric indices are certainly higher and rather in the range of about $\pm 10\%$. Within this range, energy dispersive X-ray spectroscopy (EDX) measurements confirm the contents of iron, selenium, and oxygen. Lithium was determined by inductively coupled plasma (ICP) analysis and hydrogen by elementary analysis to be 0.8(3) wt% in general agreement with the expected 0.613 wt%.

Fig. 3 shows electrical transport and low-field magnetic susceptibility measurements of the $[(\text{Li}_{0.8}\text{Fe}_{0.2})\text{OH}]\text{FeSe}$ sample. The resistivity is relatively high at 300 K and weakly temperature dependent until it drops abruptly at 43 K. Zero resistivity is reached below 25 K. The superconducting transition is confirmed by the magnetic susceptibility which becomes strongly diamagnetic below 40 K in a 3 mT field. However, the low-temperature susceptibility behaves quite unusual. After zero-field cooling (zfc, Fig. 3) the value starts strongly negative according to the shielding effect, and first increases with temperature until a maximum is reached at 10 K, then decreases again until 18 K, and finally increases steeply to zero as the temperature approaches T_c . In field-cooled mode (fc, Fig. 3), the susceptibility becomes slightly negative below 40 K owing to the Meissner-Ochsenfeld effect, but increases again to positive values at lower temperatures.

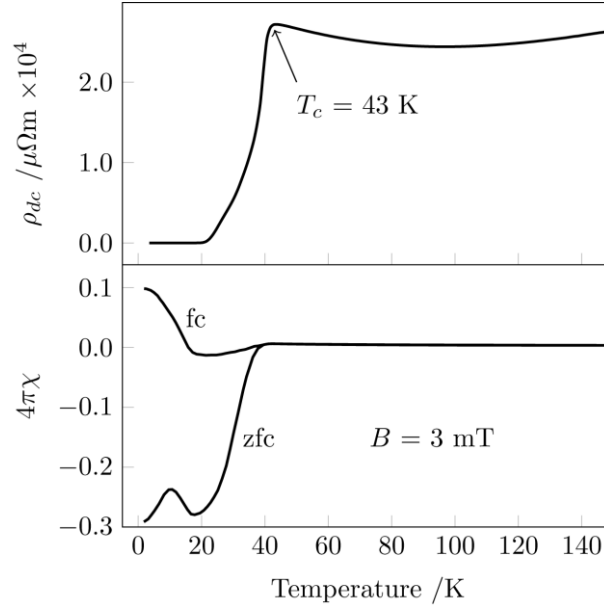


Fig. 3: Top: DC resistivity of the $[(\text{Li}_{0.8}\text{Fe}_{0.2})\text{OH}]\text{FeSe}$ sample; bottom: DC magnetic susceptibility.

Remarkably, the diamagnetism of the superconductor competes with strong paramagnetism which emerges below 18 K. The paramagnetism dominates in the fc mode, in which the diamagnetic contribution arising from the Meissner effect is weak. Thus actually no Meissner phase exists at the lowest temperatures. In contrast in zfc mode the diamagnetic shielding is much stronger than the paramagnetic contribution. Note that the resistivity remains zero at low temperatures, which means that the emerging paramagnetic field is not strong enough to destroy the superconductivity.

The magnetic susceptibility experiment suggests that superconductivity coexists with ferromagnetic ordering which emerges near 18 K, well below the critical temperature of 43 K. Fig. 4 shows the isothermal magnetization measured at 1.8 K. The typical ferromagnetic hysteresis is superimposed by the magnetization known for hard type-II superconductors.^[22, 23] This becomes obvious if the approximate ferromagnetic contribution (dashed line in Fig. 4) is subtracted. The resulting curve (inset in Fig. 4) is typical for a superconductor which is partially penetrated by magnetic flux lines (mixed or Shubnikov phase). Some flux becomes trapped by vortex pinning, therefore we detect non-zero magnetization even at zero external field ($B = 0$). The upper critical field of the superconductor is not reached at 5 T, where the magnetization makes a typical jump because the sign of the field change ΔB reverses, and thus the directions of the shielding currents are also reversed.

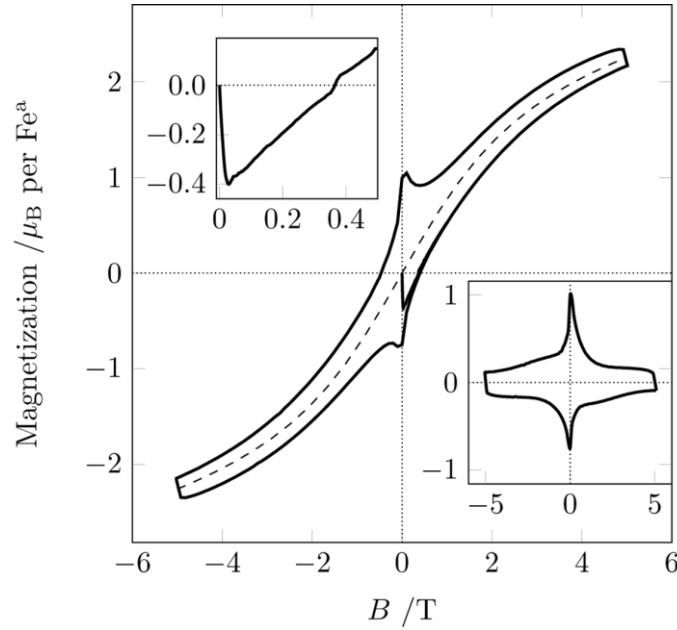


Fig. 4: Isothermal magnetization at 1.8 K; left inset: magnification of the low-field part showing the initial curve; right inset: magnetization after subtraction of the approximate ferromagnetic contribution (dashed line in the main plot).

Unlike to the Chevrel phases or ErRh_4B_4 where the ferromagnetism destroys superconductivity, we observe the rare case where both phenomena can coexist because the ferromagnetic dipole field is smaller than the upper critical field of the superconductor. Given that the magnetization emerges inside the sample owing to ferromagnetic ordering and not because of an external field, our material is in a so-called spontaneous vortex state. This is a new state of matter, where both orders coexist because the combined state has a lower free energy.^[24] Similar behavior has been suggested in $\text{EuFe}_2(\text{As}_{1-x}\text{P}_x)_2$ where ferromagnetic ordering of Eu^{2+} ($4f^7$) coexists with superconductivity.^[9, 10] In our case the ferromagnetism originates from the iron atoms in the $(\text{Li}_{0.8}\text{Fe}_{0.2})\text{OH}$ layer (see below), thus $[(\text{Li}_{0.8}\text{Fe}_{0.2})\text{OH}]\text{FeSe}$ is to our knowledge the first example where superconductivity coexists with $3d$ -ferromagnetism in a bulk material, and moreover at the highest temperatures to date.

The ^{57}Fe Mössbauer spectrum (inset in Fig. 5) consists of two doublets with an intensity ratio 0.9:0.1 in agreement with Fe^b in the FeSe and Fe^a in the hydroxide layers. The isomer shift of approximately 0.8 mm s^{-1} for Fe^a is typical for Fe^{2+} in a $S = 4/2$ state. The Fe^a doublet considerably broadens below $T_c \approx 10 \text{ K}$ which can be described by a hyperfine field of 3 T at 2.1 K. A small stray field of 0.4 T arising most probably from these ordered moments

broadens the doublet at the Fe^b site in the FeSe layer. The remanence of the internal fields confirms the ferromagnetism. The asymmetry of the spectrum results from texture. For further details see chapter 8.2.2.

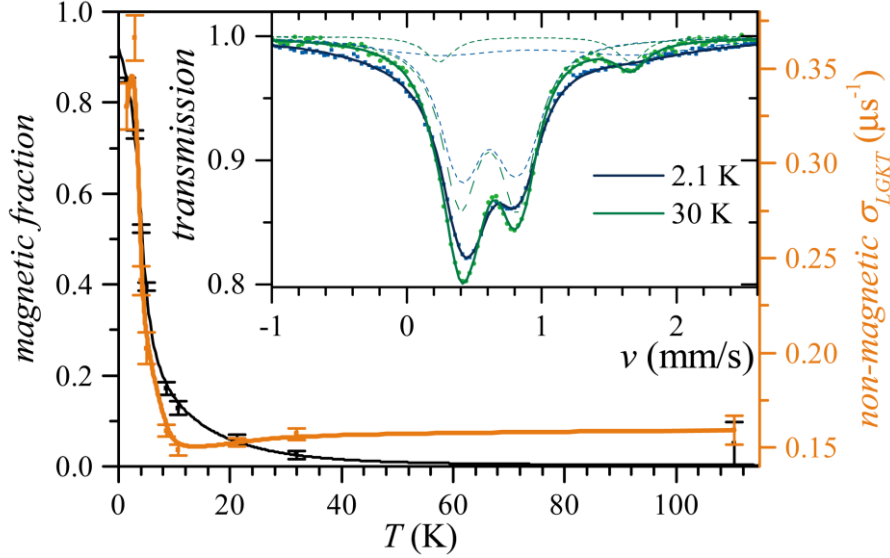


Fig. 5: Magnetic volume fraction obtained by zero-field μSR shows that almost the whole sample is ruled by ferromagnetism at low temperatures. The increase of the static relaxation rate σ_{LGKT} is due to the ferromagnetic stray field in the non-magnetic sample fraction. ^{57}Fe Mössbauer spectra detect two iron sites and demonstrate that magnetism arises from iron in the hydroxide layer, whereas the FeSe layer only senses stray fields.

Zero field muon spin rotation (μSR) data confirm the homogeneity of the sample as well as ferromagnetic ordering below $T_c \approx 10$ K (Fig. 5). The magnetism develops gradually while the whole sample is ferromagnetic at 1.5 K. A nonmagnetic fraction senses enhanced damping as a result of static fields from the magnetically ordered layer below 10 K. Reducing the field cooled flux of 200 G to 170 G we can successfully demonstrate bulk superconductivity by pinning nearly 40 % of the flux at 15 K, confirmed by transverse field (TF) data at 200 G. Cooling the sample from 40 K to 15 K a considerable damping of the precession signal in more than 40 % of the sample is induced, most probably a result of flux line lattice formation and not ferromagnetism. However both TF and pinning experiments at 1.5 K indicated, that superconducting volume fractions are reduced by ferromagnetism. For further details see chapter 8.2.3.

High-resolution^[25] ^7Li NMR spectra taken at 36 MHz show two signal fractions originating from two Li sites (Fig. 6), while the respective characteristic T_1 relaxation times are spread

over approximately three orders of magnitude. The main fraction is broad and relaxes very fast. At low temperatures, the spectrum splits into three broadened peaks. In contrast to that, the other fraction is a narrow line and relaxes very slowly. The spectrum shifts and its shape broadens slightly at low temperatures. Comparing the intensities of both spectral fractions, we assign the broad spectrum to lithium in the $(\text{Li}_{0.8}\text{Fe}_{0.2})\text{OH}$ layer, which is in line with the Mössbauer results. The close proximity to the magnetic Fe^a atoms leads to broadening and a large shift. Because the Fe^a atoms are statistically distributed, different Li-surroundings produce a complex peak structure at low temperatures. The narrow spectrum is assigned to traces of $\text{LiOH}\cdot\text{H}_2\text{O}$.

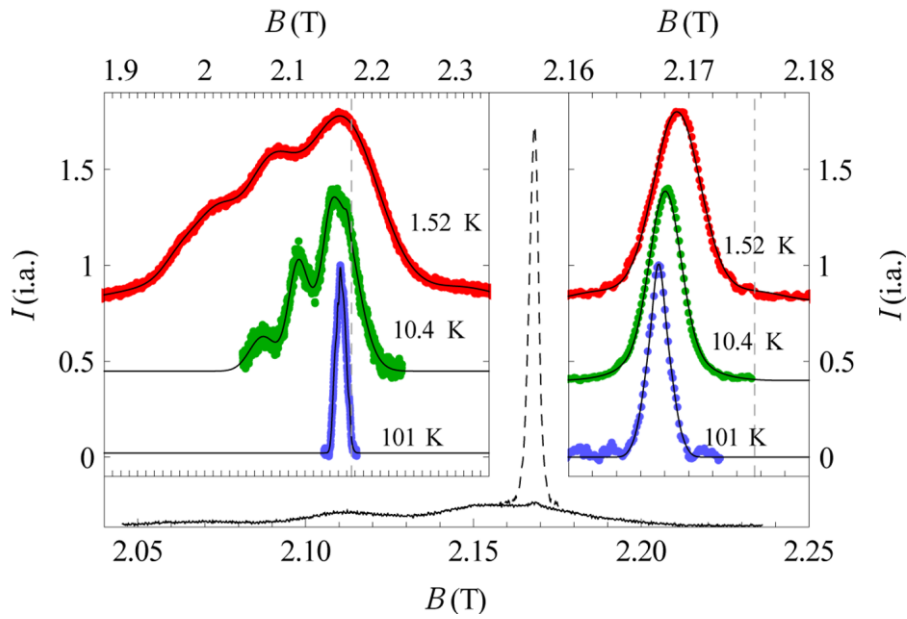


Fig. 6: ${}^7\text{Li}$ NMR spectra of $[(\text{Li}_{0.8}\text{Fe}_{0.2})\text{OH}]\text{FeSe}$. Outer graph: NMR spectra at 10 K with a short repetition time (solid line) and with a long repetition time (dashed line). Left inset: temperature dependency of the broad fraction. Right inset: temperature dependency of the narrow fraction.

DFT band-structure calculations with an ordered model of $[(\text{Li}_{0.8}\text{Fe}^a_{0.2})\text{OH}]\text{Fe}^b\text{Se}$ according to $[\text{Li}_4\text{Fe}^a(\text{OH})_5][\text{Fe}^b\text{Se}]_5$ were carried out. First the atomic coordinates of a $\sqrt{5}a \times \sqrt{5}a$ superstructure were allowed to relax, then we tried different magnetic ordering patterns. No magnetic ground state with non-zero moments at the Fe^b site in the FeSe layer could be obtained. On the other hand, ferromagnetic ordering of the moments at the Fe^a site in the hydroxide layer lowered the total energy by 41 kJ mol^{-1} with a magnetic moment of $3.5 \mu_B$ per Fe^a . Antiferromagnetic ordering resulted in the same stabilization, thus our model

cannot distinguish between ordering patterns, but it definitely shows that magnetism emerges from iron atoms in the hydroxide layer.

Fig. 7 shows the contributions of the different iron atoms to the electronic density of states (DOS). The magnetic exchange splitting of the Fe^a states is clearly discernible, while the states of the non-magnetic Fe^b sites remain almost exactly as in binary $\beta\text{-FeSe}$ (green line in Fig. 7). Moreover, the Fermi-level is located in a gap of the magnetic Fe^a states. This means that the electronic systems of the individual layers interact very weakly, and that the typical Fermi-surface topology known from other iron based superconductors^[26] is not disturbed by the presence of the hydroxide layer. Nevertheless the hydroxide layer acts as an electron reservoir. Formally 0.2 electrons are transferred from the hydroxide to the selenide layer according to $[(\text{Li}_{0.8}\text{Fe}^{2+0.2})\text{OH}]^{0.2+}(\text{FeSe})^{0.2-}$. This is also evident from the small shift of the Fe^b states (black line in Fig. 7) to lower energies relatively to $\beta\text{-FeSe}$. We suggest that this electron doping of the FeSe layer is mainly responsible for the enormous increase of T_c in our compound (43 K) in comparison to $\beta\text{-FeSe}$ (8 K). Similar electron transfers of approximately $0.2 e^-/\text{FeSe}$ have recently been reported for other intercalated iron selenides, among them $\text{Li}_x(\text{NH}_2)_y(\text{NH}_3)_{1-y}\text{Fe}_2\text{Se}_2$ ($T_c = 43 \text{ K}$),^[27, 28] $\text{K}_x\text{Fe}_2\text{Se}_2$ ($T_c = 32 \text{ K}$),^[29] $\text{Na}_x\text{Fe}_2\text{Se}_2$ ($T_c \approx 46 \text{ K}$),^[30, 31] and $\text{Li}_x(\text{C}_2\text{H}_8\text{N}_2)_y\text{Fe}_{2-z}\text{Se}_2$ ($T_c \approx 45 \text{ K}$).^[32]

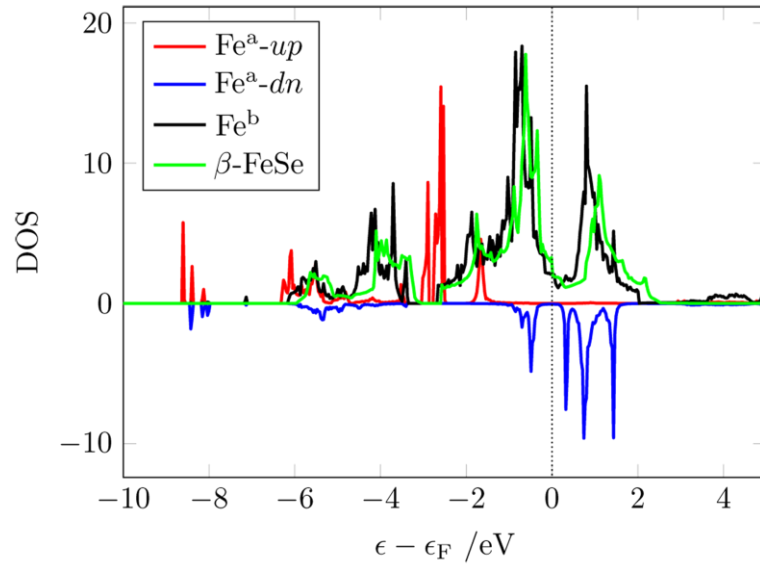


Fig. 7: Electronic density of states (DOS) contributions of the iron atoms. Red/blue: magnetic Fe^a atoms in the hydroxide layer; black: non-magnetic Fe^b atoms in the FeSe layer; green: Fe-atoms in binary $\beta\text{-FeSe}$ for comparison.

4.1.4 Conclusion

In conclusion, we have shown that superconductivity below $T_c = 43$ K coexists with ferromagnetism below $T_c \approx 10$ K in $[(\text{Li}_{0.8}\text{Fe}_{0.2})\text{OH}]\text{FeSe}$ synthesized under hydrothermal conditions. The layered crystal structure consists of ferromagnetic $(\text{Li}_{0.8}\text{Fe}_{0.2})\text{OH}$ and superconducting FeSe layers each with *anti*-PbO type structures. Both physical phenomena are spatially separated, but the internal dipole field of the ferromagnet acts on the superconductor, which suggests the existence of a special state of matter called a spontaneous vortex phase. The ^{57}Fe -Mössbauer spectroscopy, ^7Li -NMR, and μSR measurements consistently support this conclusion. This rare phenomenon was so far confined to *f*-shell magnetism, while in our compound superconductivity coexists with *3d*-ferromagnetism for the first time, and moreover at the highest temperatures to date. In contrast to the chemically inert *f*-shells, *3d*-magnetism is much more susceptible to the chemical environment, which opens new avenues for chemical modifications that can now directly couple to the magnetic and superconducting properties, thus allowing broader studies of such coexistence phenomena in the future.

4.1.5 References

- [1] B. T. Matthias, H. Suhl, E. Corenzwit, *Physical Review Letters* **1958**, *1*, 449-450.
- [2] R. Chevrel, M. Sergent, J. Prigent, *Journal of Solid State Chemistry* **1971**, *3*, 515-519.
- [3] B. T. Matthias, M. Marezio, E. Corenzwit, A. S. Cooper, H. E. Barz, *Science* **1972**, *175*, 1465-1466.
- [4] M. Ishikawa, Ø. Fischer, *Solid State Communications* **1977**, *24*, 747-751.
- [5] J. W. Lynn, D. E. Moncton, W. Thomlinson, G. Shirane, R. N. Shelton, *Solid State Communications* **1978**, *26*, 493-496.
- [6] W. A. Fertig, D. C. Johnston, L. E. DeLong, R. W. McCallum, M. B. Maple, B. T. Matthias, *Physical Review Letters* **1977**, *38*, 987-990.
- [7] J. W. Lynn, S. Skanthakumar, Q. Huang, S. K. Sinha, Z. Hossain, L. C. Gupta, R. Nagarajan, C. Godart, *Physical Review B* **1997**, *55*, 6584-6598.
- [8] J. W. Lynn, B. Keimer, C. Ulrich, C. Bernhard, J. L. Tallon, *Physical Review B* **2000**, *61*, R14964-R14967.
- [9] G. Cao, S. Xu, Z. Ren, S. Jiang, C. Feng, Z. a. Xu, *Journal of Physics: Condensed Matter* **2011**, *23*, 464204.
- [10] S. Nandi, W. T. Jin, Y. Xiao, Y. Su, S. Price, D. K. Shukla, J. Stremper, H. S. Jeevan, P. Gegenwart, T. Brückel, *Physical Review B* **2014**, *89*, 014512.

- [11] J. Wen-He, B. Jin-Ke, T. Qian, J. Hao, F. Chun-Mu, X. Zhu-An, C. Guang-Han, *Journal of Physics: Conference Series* **2012**, *400*, 022038.
- [12] D. Aoki, A. Huxley, E. Ressouche, D. Braithwaite, J. Flouquet, J.-P. Brison, E. Lhotel, C. Paulsen, *Nature* **2001**, *413*, 613-616.
- [13] A. Huxley, I. Sheikin, E. Ressouche, N. Kernavanois, D. Braithwaite, R. Calemczuk, J. Flouquet, *Physical Review B* **2001**, *63*, 144519.
- [14] S. S. Saxena, P. Agarwal, K. Ahilan, F. M. Grosche, R. K. W. Haselwimmer, M. J. Steiner, E. Pugh, I. R. Walker, S. R. Julian, P. Monthoux, G. G. Lonzarich, A. Huxley, I. Sheikin, D. Braithwaite, J. Flouquet, *Nature* **2000**, *406*, 587-592.
- [15] T. Herrmannsdörfer, R. Skrotzki, J. Wosnitza, D. Köhler, R. Boldt, M. Ruck, *Physical Review B* **2011**, *83*, 140501.
- [16] X. Zhu, H. Lei, C. Petrovic, Y. Zhang, *Physical Review B* **2012**, *86*, 024527.
- [17] X. F. Lu, N. Z. Wang, G. H. Zhang, X. G. Luo, Z. M. Ma, B. Lei, F. Q. Huang, X. H. Chen, *Physical Review B* **2014**, *89*, 020507.
- [18] H. Dachs, *Zeitschrift für Kristallographie* **1959**, *112*, 60-67.
- [19] T. M. McQueen, Q. Huang, V. Ksenofontov, C. Felser, Q. Xu, H. Zandbergen, Y. S. Hor, J. Allred, A. J. Williams, D. Qu, J. Checkelsky, N. P. Ong, R. J. Cava, *Physical Review B* **2009**, *79*, 014522.
- [20] R. D. Shannon, C. T. Prewitt, *Acta Crystallographica Section B* **1969**, *25*, 925-946.
- [21] S. Mair, *Acta Crystallographica Section A* **1978**, *34*, 542-547.
- [22] C. P. Bean, *Physical Review Letters* **1962**, *8*, 250-253.
- [23] W. Buckel, R. Kleiner, *Superconductivity. Fundamentals and Applications*, Vol. 6, Wiley-VCH, Weinheim, **2004**.
- [24] H. S. Greenside, E. I. Blount, C. M. Varma, *Physical Review Letters* **1981**, *46*, 49-53.
- [25] G. J. Rees, S. T. Orr, L. O. Barrett, J. M. Fisher, J. Houghton, G. H. Spikes, B. R. C. Theobald, D. Thompsett, M. E. Smith, J. V. Hanna, *Physical Chemistry Chemical Physics* **2013**, *15*, 17195-17207.
- [26] M. Sunagawa, T. Ishiga, K. Tsubota, T. Jabuchi, J. Sonoyama, K. Iba, K. Kudo, M. Nohara, K. Ono, H. Kumigashira, T. Matsushita, M. Arita, K. Shimada, H. Namatame, M. Taniguchi, T. Wakita, Y. Muraoka, T. Yokoya, *Scientific Reports* **2014**, *4*, 4381.
- [27] M. Burrard-Lucas, D. G. Free, S. J. Sedlmaier, J. D. Wright, S. J. Cassidy, Y. Hara, A. J. Corkett, T. Lancaster, P. J. Baker, S. J. Blundell, S. J. Clarke, *Nature Materials* **2013**, *12*, 15-19.
- [28] S. J. Sedlmaier, S. J. Cassidy, R. G. Morris, M. Drakopoulos, C. Reinhard, S. J. Moorhouse, D. O'Hare, P. Manuel, D. Khalyavin, S. J. Clarke, *Journal of the American Chemical Society* **2014**, *136*, 630-633.

-
- [29] S. V. Carr, D. Louca, J. Siewenie, Q. Huang, A. Wang, X. Chen, P. Dai, *Physical Review B* **2014**, *89*, 134509.
- [30] T. Ying, X. Chen, G. Wang, S. Jin, X. Lai, T. Zhou, H. Zhang, S. Shen, W. Wang, *Journal of the American Chemical Society* **2013**, *135*, 2951-2954.
- [31] T. P. Ying, X. L. Chen, G. Wang, S. F. Jin, T. T. Zhou, X. F. Lai, H. Zhang, W. Y. Wang, *Scientific Reports* **2012**, *2*, 426.
- [32] T. Hatakeda, T. Noji, T. Kawamata, M. Kato, Y. Koike, *Journal of the Physical Society of Japan* **2013**, *82*, 123705.

4.2 Upper critical field of $[(\text{Li}_{0.8}\text{Fe}_{0.2})\text{OH}]\text{FeSe}$

4.2.1 Introduction

Type II superconductors show ideal diamagnetism for magnetic fields smaller than the lower critical field H_{c1} . For fields larger than the upper critical field H_{c2} , superconductivity is completely suppressed. In between H_{c1} and H_{c2} , the so-called Shubnikov-phase, the magnetic field partially penetrates the sample. Additionally to the superconducting currents responsible for the Meissner effect, circulating superconducting screening currents create vortices. These vortices enable a quantum of magnetic flux to go through them and thus allow part of the applied magnetic field to go through the superconducting sample. Owing to the vortices the superconductor can bear much larger magnetic fields. Thereby, the electric resistance remains zero as the electric current can flow unhindered through the sample by simply avoiding the vortices. The upper critical field is thus one of the fundamental parameters in type II superconductors, especially with regard to applications.

In the precedent chapter $[(\text{Li}_{0.8}\text{Fe}_{0.2})\text{OH}]\text{FeSe}$ was shown to be a ferromagnetic superconductor, where ferromagnetism and superconductivity can coexist because the ferromagnetic dipole field is smaller than the upper critical field of the superconductor. The latter is not reached at 5 T, where the magnetization makes a typical jump. The following chapter presents the investigation of the upper critical field of $[(\text{Li}_{0.8}\text{Fe}_{0.2})\text{OH}]\text{FeSe}$.

4.2.2 Experimental details

The polycrystalline sample was prepared as described in chapter 4.1.2. The synthesized compound was pressed into a pellet with a diameter of 4 mm. Owing to the temperature sensibility of the compounds, the cold pressed pellets had to be used without sintering. As no glove box was available at the Walther-Meißner-Institut where the measurements were carried out, the pellet was wired in air with 20 μm gold wires and silver conductive paint. The resistivity was measured while sweeping the temperature from 2.5 to 60 K in a fixed field of 0 to 15 T. The cooling in between two measurements was performed without applied field.

4.2.3 Results and discussion

First, the influence of exposure to air on the transport properties was examined to ensure that the wiring in air does not cause any serious problems for the subsequent measurements. In Fig. 1, the temperature dependent resistivity of $[(\text{Li}_{0.8}\text{Fe}_{0.2})\text{OH}]\text{FeSe}$ is shown for a pellet wired in air (black) and under argon atmosphere (blue). The exposure time in air was about 15 min.

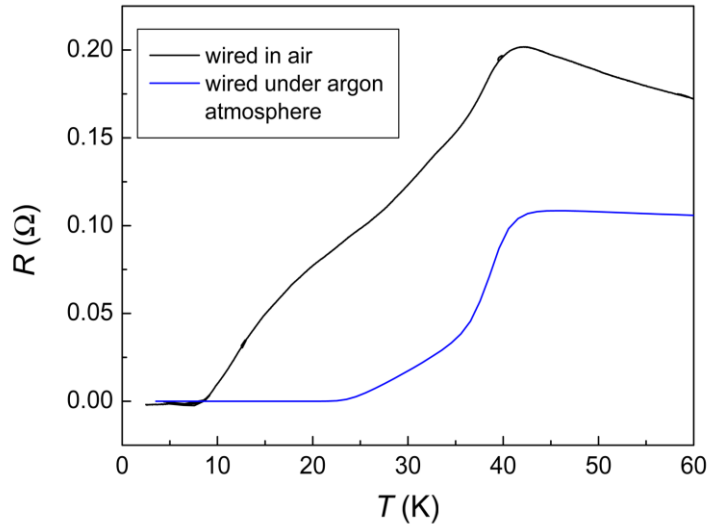


Fig. 1: Influence of exposure to air on the transport properties of $[(\text{Li}_{0.8}\text{Fe}_{0.2})\text{OH}]\text{FeSe}$.

The resistivity is enlarged and zero resistivity is reached only below 8 K in contrast to 23 K for the sample wired under argon atmosphere. However, the onset transition point where resistivity drops due to the onset of superconductivity is almost the same (about 43 K) for both pellets. This is understandable since the zero resistance point is determined by the weak links between the grains as well as the vortex flow behavior, while the onset transition is controlled by $T_c(H_{c2})$ of the individual grains.^[1] During exposure to air, the surface of the grains and by association the links between them will degrade first. Thus, the superconducting properties of the pellet wired in air are declined due to degraded links between the individual grains, but it is no problem to study the upper critical field on this pellet.

Fig. 2 shows the temperature dependence of resistivity of the $[(\text{Li}_{0.8}\text{Fe}_{0.2})\text{OH}]\text{FeSe}$ sample under different magnetic fields. The upper critical field $H_{c2}(T)$ can be determined by taking a criterion of 99 % R_n where R_n is the extrapolated normal state resistivity (dashed line in Fig. 2). The onset transition point is taken as the upper critical point $T_c(H_{c2})$ where almost

all Cooper pairs are broken.^[1] It continuously shifts to lower temperatures with magnetic field.

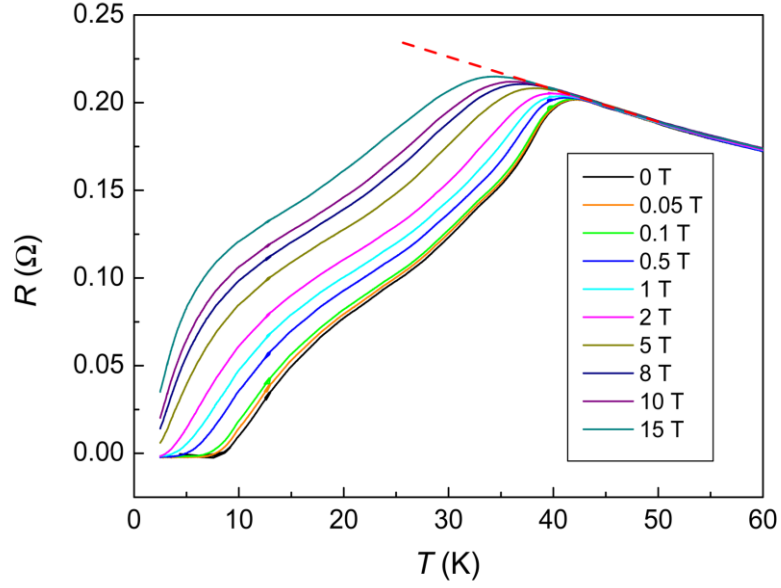


Fig. 2: Temperature dependence of resistivity of $[(\text{Li}_{0.8}\text{Fe}_{0.2})\text{OH}]\text{FeSe}$ under different magnetic fields. The onset transition point shifts weakly with magnetic field. The dashed line indicates the extrapolation of the normal state resistivity.

There are two possibilities to determine the upper critical field $H_{c2}(0)$ based on the measured data. The Werthamer-Helfand-Hohenberg (WHH) formula^[2] estimates the zero-temperature upper critical field $H_{c2}(0)$ by

$$H_{c2}(0) = -0.693 T_c \left(\frac{dH_{c2}}{dT} \right)_{T=T_c}. \quad (1)$$

The slope of $H_{c2}(T)$, i.e. dH_{c2}/dT near T_c is determined in Fig. 3 to about -2.66 T K^{-1} . With $T_c = 43.3 \text{ K}$, $H_{c2}(0)$ is about 80 T.

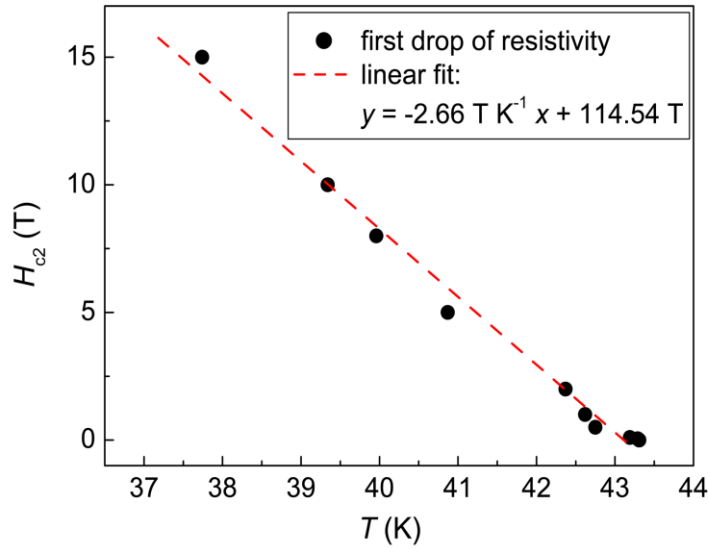


Fig. 3: Temperature dependent upper critical field derived from resistive transition curves. The dashed line represents the linear fit of the onset transition points.

The value of 80 T coincides with observations of Dong *et al.* on large crystals of $[(\text{Li}_{0.8}\text{Fe}_{0.2})\text{OH}]\text{FeSe}$. For the crystals, $H_{c2}(0)$ was estimated to 79 T for the field along c axis and 313 T for the field in the ab plane.^[3] This anisotropy of the superconducting state cannot be examined for polycrystalline samples where the individual crystallites are oriented arbitrarily.

Another possibility to determine H_{c2} is based on the Ginzburg-Landau (GL) equation. In GL theory, the connectedness $H_{c2} = \Phi_0/2\pi\xi^2$ and $\xi \propto \sqrt{(1+t^2)/(1-t^2)}$, with Φ_0 the flux quanta, ξ the coherence length and $t = T/T_c$ the reduced temperature is known,^[1] thus

$$H_{c2}(T) = H_{c2}(0) \frac{1-t^2}{1+t^2}.^{[1]} \quad (2)$$

The GL theory is especially applicable near T_c . However, equation (2) has been shown to be satisfied in a much wider temperature regime.^[1, 4] In Fig. 4 the above equation was used to fit (dashed line) the experimental data. The zero-temperature upper critical field $H_{c2}(0)$ determined in this way is $H_{c2}(0) \approx 104$ T.

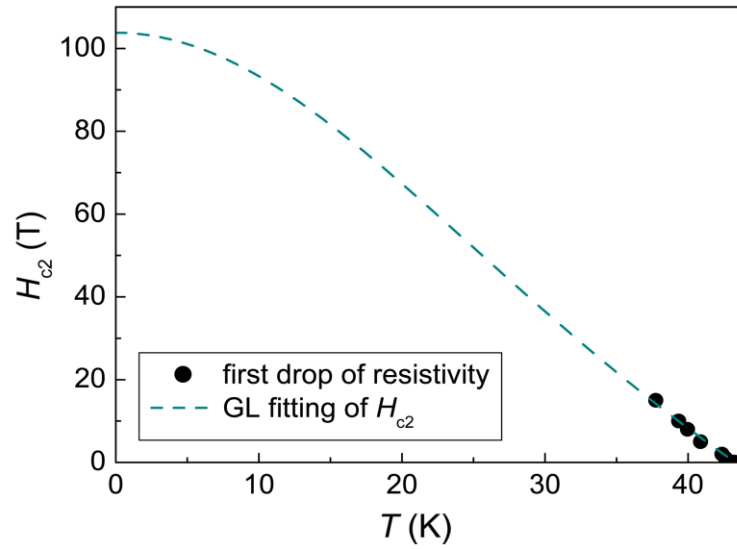


Fig. 4: Temperature dependent upper critical field derived from resistive transition curves. The dashed line shows the theoretical curve based on GL theory (equation (2)).

Analogously to the observations of Zhu *et al.* as well as Fang *et al.*, the value obtained from GL theory is about 20 % larger than the one obtained using the WHH formula. In general, the values have to be seen as a rough estimation due to the limit of available magnetic fields and inevitable inaccuracies during the determination of $H_{c2}(T)$. However, the result gives a rough dimension of $H_{c2}(0)$ and shows that the upper critical field of $[(\text{Li}_{0.8}\text{Fe}_{0.2})\text{OH}]\text{FeSe}$ is in the same large magnitude as for other iron based superconductors.^[5, 6]

4.2.4 Conclusion

In summary, the temperature dependence of resistivity under different magnetic fields was measured in the layered superconductor $[(\text{Li}_{0.8}\text{Fe}_{0.2})\text{OH}]\text{FeSe}$. Based on these measurements, the upper critical field of $[(\text{Li}_{0.8}\text{Fe}_{0.2})\text{OH}]\text{FeSe}$ was determined roughly to be about 80–100 T. This large magnitude coincides with values obtained for other iron based superconductors.

4.2.5 References

- [1] X. Zhu, H. Yang, L. Fang, G. Mu, H.-H. Wen, *Superconductor Science and Technology* **2008**, *21*, 105001.
- [2] N. R. Werthamer, E. Helfand, P. C. Hohenberg, *Physical Review* **1966**, *147*, 295-302.

-
- [3] X. Dong, K. Jin, D. Yuan, H. Zhou, J. Yuan, Y. Huang, W. Hua, J. Sun, P. Zheng, W. Hu, Y. Mao, M. Ma, G. Zhang, F. Zhou, Z. Zhao, *Physical Review B* **2015**, 92, 064515.
- [4] L. Fang, Y. Wang, P. Y. Zou, L. Tang, Z. Xu, H. Chen, C. Dong, L. Shan, H. H. Wen, *Physical Review B* **2005**, 72, 014534.
- [5] Z.-S. Wang, H.-Q. Luo, C. Ren, H.-H. Wen, *Physical Review B* **2008**, 78, 140501.
- [6] J.-l. Zhang, L. Jiao, Y. Chen, H.-q. Yuan, *Frontiers of Physics* **2011**, 6, 463-473.

4.3 Investigations on the real structure of $[(\text{Li}_{0.8}\text{Fe}_{0.2})\text{OH}]\text{FeX}$ ($X = \text{Se}, \text{S}$)

4.3.1 Introduction

The crystalline state of a solid is the regular arrangement of atoms that can be generated by periodic translations of the unit cell.^[1] This three dimensional periodic array is the basis for the occurrence of discrete diffraction peaks, called *Bragg* reflections, which in turn are the basis for crystal structure determination. However, the real state is generally different from these ideal crystals. Several types of crystal imperfections do exist, and very often the physical properties of the solids are caused by such imperfections. There are many demonstrations that the deviations from regular structure such as grains, blocks, boundaries, point defects, etc. define the distinguishing properties of a given material, so these various types of disorder are the basis for all semiconductor physics, the physics of strength and plasticity, magnetic materials, etc.^[2]

The impact of disorder with respect to diffraction intensities depends on the nature and density of the defects. A single point defect, for example occupational or positional disorder, will not produce detectable effects on diffraction maxima, whereas a large number of them strongly affect diffraction. For a large number of point defects also some kind of an ‘ordered’ form of disorder is possible, where the structure can be derived from a basic structure with translational symmetry. The point defects order in a commensurate or incommensurate manner leading to a superstructure respectively a modulation, which can be described by modulation waves complementing the description of the basic structure.^[3] In diffraction patterns, satellite reflections appear additionally to the Bragg reflections of the basic structure.

For layered compounds, one dimensional or stacking disorder is a common phenomenon regarding crystal imperfections. In this case, the lack of three-dimensional translation symmetry is caused by different possible layer arrangements, thus faults in the stacking sequence. This stacking disorder leads to diffuse scattering contributions along the stacking direction.

The additional scattering contributions caused by the various types of disorder can be of very low intensity (e.g. typical diffuse scattering intensities are $\sim 10^3$ – 10^4 times lower than those of Bragg peaks).^[4] A conventional structure determination in defiance of the disorder, thus based only on the Bragg reflections of the appropriate ordered structure is mostly successful but results only in average structure models. In such a case, the disorder often becomes apparent in abnormally large, strongly anisotropic displacement ellipsoids and

possibly in chemically unreasonable atomic arrangements. However, as mentioned above, the defects are a critical point with regard to physical properties in many cases. Thus, analysis of the real structure is often of vital importance for a better understanding of the relationship between crystal structure and physical properties.

The recently discovered $[(\text{Li}_{0.8}\text{Fe}_{0.2})\text{OH}]\text{FeSe}$ in which iron-selenide layers are separated by lithium-iron hydroxide layers shows outstanding physical properties, namely the coexistence of superconductivity and magnetism.^[5-8] The magnetism is caused by iron atoms in the $(\text{Li}_{0.8}\text{Fe}_{0.2})\text{OH}$ layers. The concrete type of magnetic ordering is controversial in literature. While we observe clear signatures of ferromagnetism with a possible spontaneous vortex state,^[7, 9] other groups claimed canted antiferromagnetism.^[6] Neutron diffraction and small angle scattering experiments confirmed the coexistence of ferromagnetism and superconductivity in $[(\text{Li}_{0.8}\text{Fe}_{0.2})\text{OH}]\text{FeSe}$.^[10]

Another still unsettled issue is the true structure of the magnetic $(\text{Li}_{0.8}\text{Fe}_{0.2})\text{OH}$ layer. Previous X-ray and neutron diffraction experiments consistently locate lithium/iron atoms statistically distributed in flattened oxygen tetrahedra. However, the component of the mean-square displacement at the Li/Fe site is as large as 800 pm² perpendicular to the layer (U_{33}), but has normal values around 100 pm² within the layer (U_{11}/U_{22}). This large anisotropy exclusively concerns the Li/Fe position while the displacements of all other atoms are nearly spherical (Fig. 1).

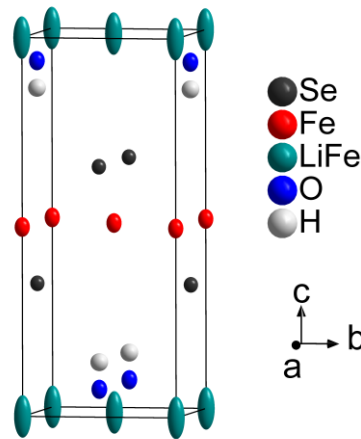


Fig. 1: Unit cell of $[(\text{Li}_{0.8}\text{Fe}_{0.2})\text{OH}]\text{FeSe}$. The displacement ellipsoids represent 50 % localization probability.

The large U_{33} displacement indicates either enhanced thermal motion in this direction, incorrect space group symmetry, a superstructure, or a modulation caused by Li/Fe ordering in the $(\text{Li}_{0.8}\text{Fe}_{0.2})\text{OH}$ layer. Superstructure spots at $\mathbf{q} = \frac{1}{2}(1,1,0)$ have been observed in electron diffraction experiments,^[5] but the underlying ordering remained unresolved. These weak spots are not detectable with laboratory X-ray diffraction.

All previous studies settled for average structures, either by accepting the large U_{33} ,^[8] by using split-atom approximations,^[7, 9] or by getting around the problem through fixing the displacement parameter of this site.^[6] This is quite unsatisfactory given the outstanding superconducting and magnetic properties. The isostructural compound $[(\text{Li}_{0.8}\text{Fe}_{0.2})\text{OH}]\text{FeS}$ exhibits the same phenomenon of elongated displacement ellipsoids at the Li/Fe position, thus crystals of both compounds are investigated in this chapter. Experimental details as well as chemical and physical properties of $[(\text{Li}_{0.8}\text{Fe}_{0.2})\text{OH}]\text{FeS}$ will be discussed in chapter 4.5. In this chapter the real structure of $[(\text{Li}_{0.8}\text{Fe}_{0.2})\text{OH}]\text{FeX}$ ($X = \text{Se}, \text{S}$) is investigated in terms of the strongly anisotropic displacement ellipsoids in the magnetic $(\text{Li}_{0.8}\text{Fe}_{0.2})\text{OH}$ layer.

4.3.2 Experimental details

Single crystals of $[(\text{Li}_{0.8}\text{Fe}_{0.2})\text{OH}]\text{FeSe}$ were isolated from polycrystalline samples prepared under the hydrothermal conditions described in chapter 4.1.2. Additionally, single crystals of the sulfur compound $[(\text{Li}_{0.8}\text{Fe}_{0.2})\text{OH}]\text{FeS}$ were isolated from polycrystalline samples prepared under the hydrothermal conditions described in chapter 4.5.2.

4.3.3 Results and discussion

Static displacements can be distinguished from thermal motion by the temperature dependence of the mean square displacements (MSD), obtained from the diagonalized U_{ij} matrix. To exclude enhanced thermal motion as a reason for the enlarged U_{33} displacement at the Li/Fe site, low temperature single crystal measurements were performed between 300 and 100 K. Upon cooling, U_{33} decreases to 120 pm² at $T \rightarrow 0$ (extrapolated, Fig. 2) suggesting static disorder of the Li/Fe z -coordinates. In contrast, the extrapolation of the component within the layer (U_{11}) as well as the components of the mean-square displacement of the Fe site in the FeSe layer are almost zero at $T \rightarrow 0$. Thus, thermal motion can be excluded as reason for the strongly anisotropic displacement ellipsoid.

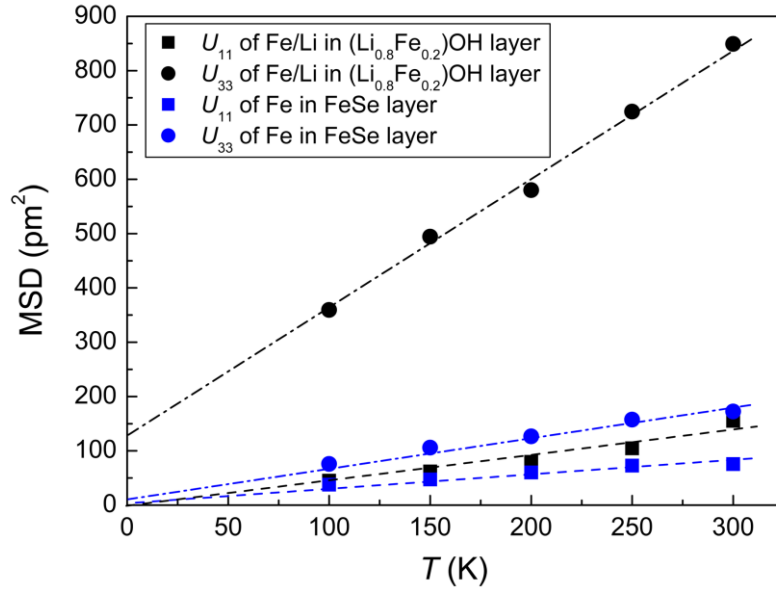


Fig. 2: Mean square displacements of the Li/Fe site in the $(\text{Li}_{0.8}\text{Fe}_{0.2})\text{OH}$ layer (black) and the Fe site in the FeSe layer (blue).

In a next step, transmission electron microscopy (TEM) was applied to confirm the superstructure spots at $\mathbf{q} = \frac{1}{2}(1,1,0)$ observed in Ref. [5] for the samples presented in this thesis and to further investigate possible reasons for the elongated displacement ellipsoid in the $(\text{Li}_{0.8}\text{Fe}_{0.2})\text{OH}$ layer. The TEM measurements confirm the presumed unit cell as well as the superstructure spots at $\mathbf{q} = \frac{1}{2}(1,1,0)$, which correspond to a $\sqrt{2}a \times \sqrt{2}a$ superstructure in a^*b^* plane (Fig. 3). No additional spots or diffuse streaks were detected in this direction. An analogue superstructure is observed in the superconducting phase of $\text{K}_y\text{Fe}_{2-x}\text{Se}_2$, which might give a hint to an association with the intrinsic electronic states for superconductivity as discussed by Dong *et al.*[5] The origin of this superstructure, whether and how it is microscopically correlated with spin- and/or charge-ordered states remains nevertheless unknown.[5]

The completion of high-resolution TEM, which could help to identify respectively exclude structural factors as reason for the observed superstructure spots was not successful due to a lack of sample stability.

TEM-EDX at multiple spots of the crystals showed that the distribution of iron is homogeneous, thus there is no hint for an accumulation of the iron in the $(\text{Li}_{0.8}\text{Fe}_{0.2})\text{OH}$ layers.

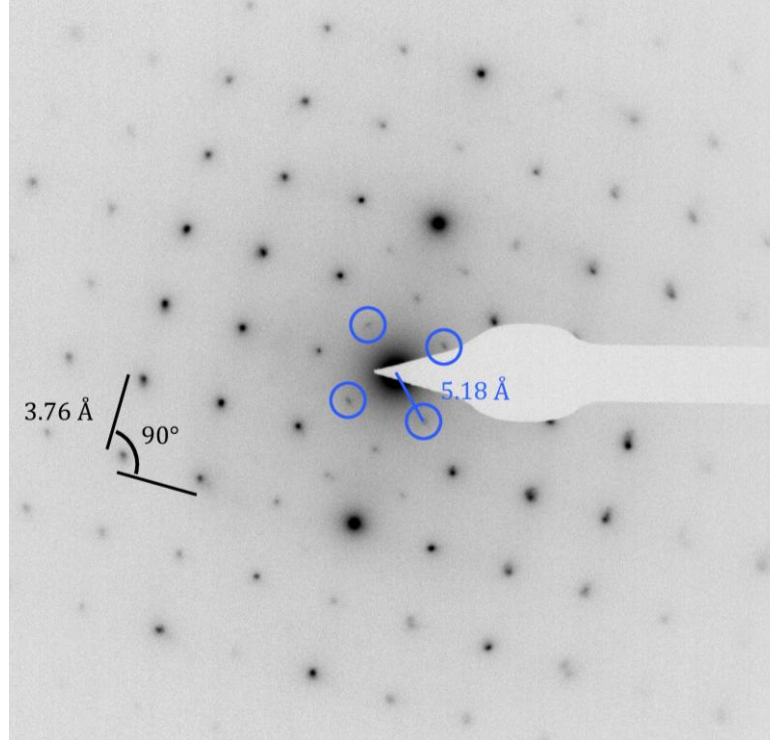


Fig. 3: Selected area diffraction pattern taken along $[001]$ zone axis direction. The blue circles exemplarily highlight superstructure spots, characterized by the modulation wave vector $\mathbf{q} = \frac{1}{2}(1,1,0)$.

Synchrotron single crystal X-ray diffraction measurements with a small wavelength $\lambda = 18.9722$ pm and small swivel angel were performed in order to achieve high resolution and maximum intensity. Several single crystals of $[(\text{Li}_{0.8}\text{Fe}_{0.2})\text{OH}]\text{FeX}$ ($X = \text{Se}, \text{S}$) were investigated at temperatures between 300 and 120 K. Fig. 4 shows the $h0l$ and $h1l$ cross sections of a $[(\text{Li}_{0.8}\text{Fe}_{0.2})\text{OH}]\text{FeSe}$ single crystal measured at 120 K. For all single crystals, diffuse scattering contributions appear along l (highlighted in Fig. 4), thus along the stacking direction c^* . The diffuse scattering is present for the entire temperature range 300–120 K in $nk l$ as well as hnl cross sections, indicating stacking disorder in $[(\text{Li}_{0.8}\text{Fe}_{0.2})\text{OH}]\text{FeX}$ compounds. As diffuse streaks are observed for all $h, k \in \mathbf{Z}$ no ordered substructures exist. In hkn cross sections exclusively sharp Bragg reflections occur, which accounts for the absence of disorder within the layers.

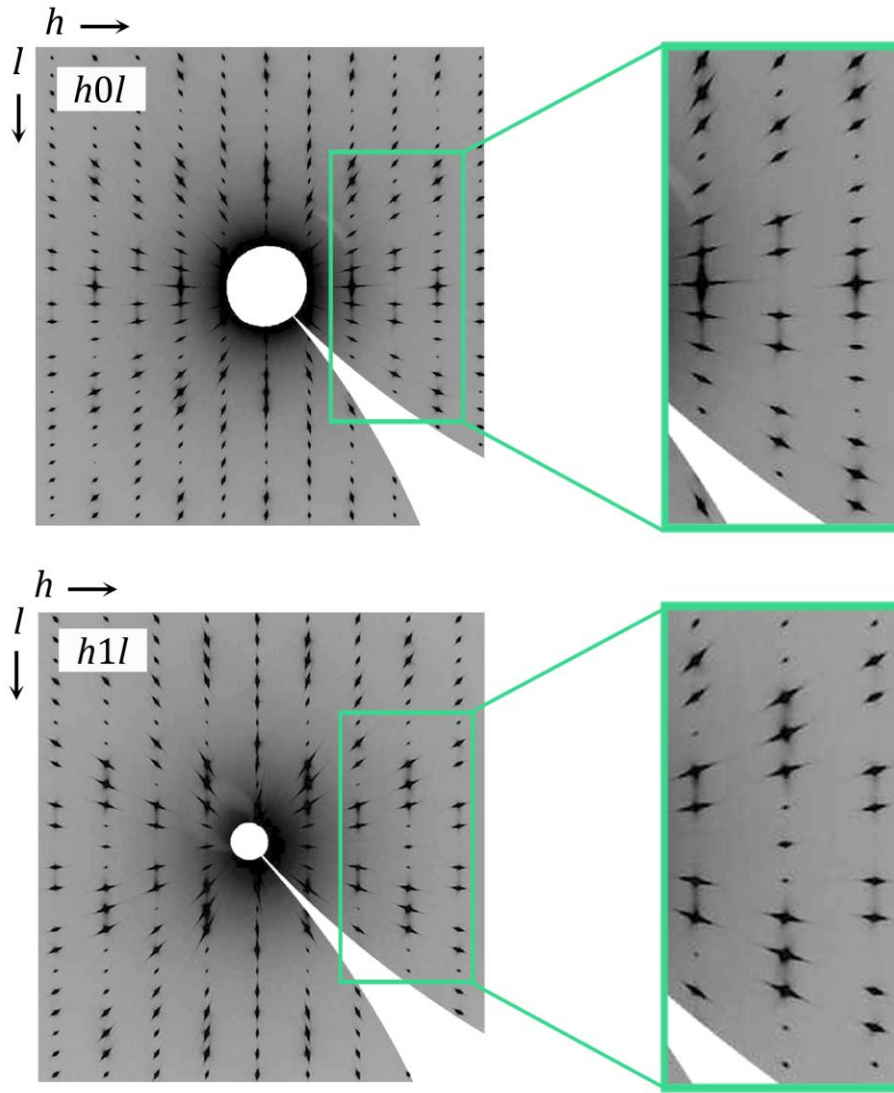


Fig. 4: $h0l$ (top) and $h1l$ (bottom) cross sections of a $[(\text{Li}_{0.8}\text{Fe}_{0.2})\text{OH}]\text{FeSe}$ single crystal.

The origin of diffuse scattering contributions can be examined by an empirical evaluation of diffraction data. By means of the simulation program DIFFaX,^[11] several disordered stacking models were tested and the simulated selected area diffraction patterns were compared to the experimentally obtained cross sections of the synchrotron X-ray diffraction measurements. There is one stacking disorder model where experimental and simulated data coincide very well (Fig. 5): the stacking transition probability that two identical layers FeSe respectively $(\text{Li}_{0.8}\text{Fe}_{0.2})\text{OH}$ follow each other is not zero but roughly 0.2 % in contrast to the ideally ordered structure where the two layers alternate without exception. This slight deviation from translational symmetry has noticeable impact on the observed diffraction data, resulting in diffuse streaks.

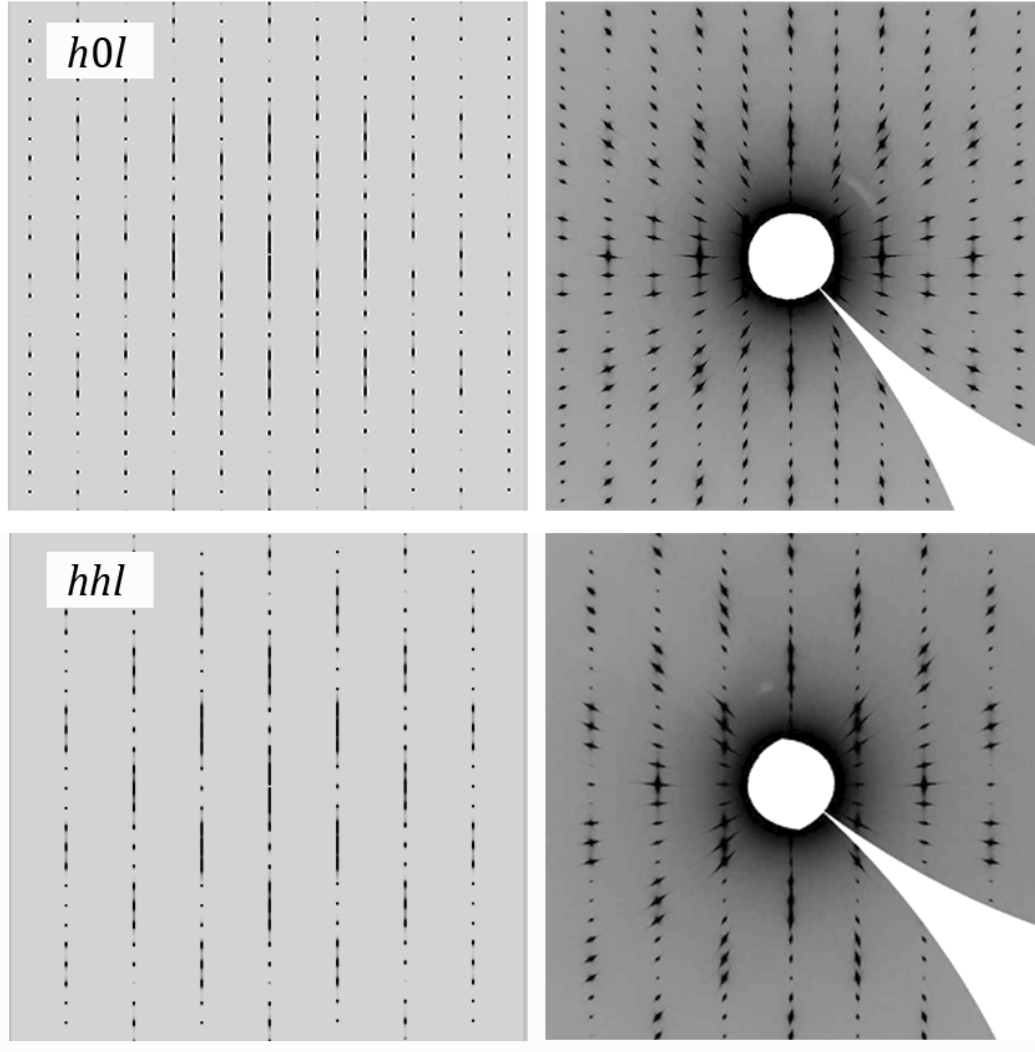


Fig. 5: $h0l$ (top) and hhl (bottom) simulated selected area diffraction patterns (left) respectively cross sections (right) of a $[(\text{Li}_{0.8}\text{Fe}_{0.2})\text{OH}]\text{FeSe}$ single crystal.

The present model of stacking disorder fits the data very well and is chemically reasonable. Both underlying structures of the layers, $\beta\text{-FeX}$ ($X = \text{Se}, \text{S}$) and LiOH crystallize in *anti*-PbO type structure with similar lattice parameters a (376.8 pm for $\beta\text{-FeSe}$,^[12] 368.2 pm for $\beta\text{-FeS}$,^[13] 354.9 pm for LiOH ^[14]). In these base structures the layers are consecutively stacked without any other layers, thus it is highly plausible that the above-mentioned scenario, namely the direct succession of two layers FeX respectively $(\text{Li}_{0.8}\text{Fe}_{0.2})\text{OH}$ occurs in $[(\text{Li}_{0.8}\text{Fe}_{0.2})\text{OH}]\text{FeX}$ ($X = \text{Se}, \text{S}$) with a certain probability.

The synchrotron data, together with results from NMR measurements and TEM analysis show that an ordering of lithium and iron within the $(\text{Li}_{0.8}\text{Fe}_{0.2})\text{OH}$ layer of $[(\text{Li}_{0.8}\text{Fe}_{0.2})\text{OH}]\text{FeX}$ is rather improbable. ^7Li NMR spectra assume a random distribution of Li

and Fe atoms in the $(\text{Li}_{0.8}\text{Fe}_{0.2})\text{OH}$ layer where Li with zero and one nearest-neighboring (NN) Fe atoms has a probability of $P_0 = P_1 = 0.41$ and Li with two NN Fe atoms a probability of $P_2 = 0.15$ (probability for three and four NN Fe atoms is negligible).^[15] Based on these values, no $\sqrt{2} a \times \sqrt{2} a$ superstructure which results from an ordering of Li and Fe atoms can be found. Furthermore, in synchrotron X-ray diffraction measurements no superstructure reflections are observed in any direction in contrast to weak diffuse scattering. This might support that the $\sqrt{2} a \times \sqrt{2} a$ superstructure observed in the electron diffraction measurements originates rather from possible charge ordering which can not be detected in the X-ray diffraction measurements. Conclusively, an ordering of lithium and iron in the $(\text{Li}_{0.8}\text{Fe}_{0.2})\text{OH}$ layer was not observed and seems improbable as reason for the elongated displacement ellipsoid.

The diffuse scattering which was observed in synchrotron X-ray diffraction measurements is due to a stacking disorder as shown above. Generally, diffuse scattering contributions prevent an accurate measurement of separated hkl intensities, which often leads to artefacts or average structure models. In our case, the diffuse scattering contributions are weak and we do not observe any systematic influence on the respective Bragg intensities. Thus, the appearance of artefacts is rather implausible. The average structure model arises from projection of the disordered structure in the unit cell. In $[(\text{Li}_{0.8}\text{Fe}_{0.2})\text{OH}]\text{FeX}$, only the Li/Fe site in the $(\text{Li}_{0.8}\text{Fe}_{0.2})\text{OH}$ layer shows an anomal displacement ellipsoid. Given the fact that the displacement ellipsoids in the FeSe layer and especially the one of oxygen show no perceptible anomalies, it seems improbable that the impact of diffuse scattering contributions is the reason for the elongated displacement ellipsoid.

Based on these investigations on the real structure of $[(\text{Li}_{0.8}\text{Fe}_{0.2})\text{OH}]\text{FeX}$ ($X = \text{Se}, \text{S}$), a split-atom approximation seems most probable. In the split-atom model, lithium is shifted off the center of the oxygen tetrahedron along the c -direction. This displacement results in a reduction of two out of four Li–O distances which otherwise would be significantly larger than the respective distance in LiOH.^[7] Possible investigations to confirm this deviation from tetrahedral site symmetry, for example by means of electron energy loss spectroscopy (EELS) or NMR measurements are aggravated by the multiplicity of Li surroundings due to the various numbers of NN Fe atoms. These different surroundings of Li lead to broad signals, which in turn hinder a more detailed analysis.

4.3.4 Conclusion

The real structure of $[(\text{Li}_{0.8}\text{Fe}_{0.2})\text{OH}]\text{FeX}$ ($X = \text{Se}, \text{S}$) was investigated in order to find reasons for the strongly anisotropic displacement ellipsoid at the Li/Fe position of the magnetic $(\text{Li}_{0.8}\text{Fe}_{0.2})\text{OH}$ layer. Even if no proof of a certain scenario was gained, several reasons were excluded leading to a split-atom approximation as favorite real structure model. Apart from this, synchrotron single crystal X-ray diffraction measurements revealed stacking disorder in $[(\text{Li}_{0.8}\text{Fe}_{0.2})\text{OH}]\text{FeX}$ where two identical layers FeX respectively $(\text{Li}_{0.8}\text{Fe}_{0.2})\text{OH}$ follow each other with a certain probability. Finally, a $\sqrt{2} a \times \sqrt{2} a$ superstructure which previously was observed in TEM measurements was confirmed. Given the absence of respective superstructure reflections in the presence of weak diffuse scattering contributions in synchrotron X-ray diffraction measurements, the hypothesis of underlying charge-ordered states was supported.

4.3.5 References

- [1] C. Giovacazzo, H. L. Monaco, G. Artioli, D. Viterbo, M. Milanesio, G. Ferraris, G. Gilli, P. Gilli, G. Zanotti, M. Catti, *Fundamentals of Crystallography*, Oxford University Press, Oxford, **2011**.
- [2] V. S. Shekhtman, *The Real Structure of High-Tc Superconductors*, Springer-Verlag Berlin Heidelberg GmbH, **1993**.
- [3] S. v. Smaalen, *Incommensurate Crystallography*, 1 ed., Oxford University Press, Oxford, **2007**.
- [4] T. R. Welberry, *Diffuse X-ray Scattering and Models of Disorder*, 1 ed., Oxford University Press, Oxford, **2004**.
- [5] X. Dong, H. Zhou, H. Yang, J. Yuan, K. Jin, F. Zhou, D. Yuan, L. Wei, J. Li, X. Wang, G. Zhang, Z. Zhao, *Journal of the American Chemical Society* **2014**, *137*, 66-69.
- [6] X. F. Lu, N. Z. Wang, H. Wu, Y. P. Wu, D. Zhao, X. Z. Zeng, X. G. Luo, T. Wu, W. Bao, G. H. Zhang, F. Q. Huang, Q. Z. Huang, X. H. Chen, *Nature Materials* **2015**, *14*, 325-329.
- [7] U. Pachmayr, F. Nitsche, H. Luetkens, S. Kamusella, F. Brückner, R. Sarkar, H.-H. Klauss, D. Johrendt, *Angewandte Chemie International Edition* **2015**, *54*, 293-297.
- [8] H. Sun, D. N. Woodruff, S. J. Cassidy, G. M. Allcroft, S. J. Sedlmaier, A. L. Thompson, P. A. Bingham, S. D. Forder, S. Cartenet, N. Mary, S. Ramos, F. R. Foronda, B. H. Williams, X. Li, S. J. Blundell, S. J. Clarke, *Inorganic Chemistry* **2015**, *54*, 1958-1964.
- [9] U. Pachmayr, D. Johrendt, *Chemical Communications* **2015**, *51*, 4689-4692.

-
- [10] J. W. Lynn, X. Zhou, C. K. H. Borg, S. R. Saha, J. Paglione, E. E. Rodriguez, *Physical Review B* **2015**, 92, 060510.
- [11] M. M. J. Treacy, M. W. Deem, J. M. Newsam, *DIFFaX*, 1.812 ed., **2005**.
- [12] F.-C. Hsu, J.-Y. Luo, K.-W. Yeh, T.-K. Chen, T.-W. Huang, P. M. Wu, Y.-C. Lee, Y.-L. Huang, Y.-Y. Chu, D.-C. Yan, M.-K. Wu, *Proceedings of the National Academy of Sciences* **2008**, 105, 14262-14264.
- [13] U. Pachmayr, N. Fehn, D. Johrendt, *Chemical Communications* **2016**, 52, 194-197.
- [14] S. Mair, *Acta Crystallographica Section A* **1978**, 34, 542-547.
- [15] Y. P. Wu, D. Zhao, X. R. Lian, X. F. Lu, N. Z. Wang, X. G. Luo, X. H. Chen, T. Wu, *Physical Review B* **2015**, 91, 125107.

4.4 Crystal growing of large $[(\text{Li}_{0.8}\text{Fe}_{0.2})\text{OH}]\text{FeSe}$ crystals

4.4.1 Introduction

Crystal growth is an ancient scientific activity. As early as 1500 BC, humankind practiced crystal growth and/or crystallization processes in the form of salt and sugar crystallization.^[1] The scientific approach started in 1611 when Kepler correlated crystal morphology and structure.^[1] Since then, crystal growth has evolved steadily to attain its present status where large-scale applications for devices are realized. Apart from this application-oriented significance, large crystals carry vital weight on analytical issues as well. Single crystals large enough for physical measurements are of great interest to better measure and understand physical properties. ARPES (angle-resolved photoemission spectroscopy) is one example for a powerful technique for which atomically defined, clean surfaces are required, which generally are obtained by cleavage of single crystals in high vacuum. In the study of high-temperature superconductors, the technique provides access to experimentally map out Fermi surfaces and to explore the superconducting gap as a function of temperature and momentum, for example.^[2] Large crystals are often highly desired especially for materials with anisotropic structure to obtain information about the behavior along discrete crystallographic orientations. For layered compounds for example, the physical properties parallel and perpendicular to the layers can be investigated. Contrary to powder samples where only average values can be extracted, large crystals offer the opportunity to directly investigate the phenomena along the different directions. Furthermore, single crystals have an advantage over polycrystalline samples due to the absence of grain boundaries and the higher homogeneity in most cases.

Various techniques like solution growth, melt growth, flux growth, hydrothermal growth etc. have been developed, depending on the chemical process involved.^[1] In this chapter, large crystals $[(\text{Li}_{0.8}\text{Fe}_{0.2})\text{OH}]\text{FeSe}$ are prepared via hydrothermal ion-exchange method, where one solid is chemically transformed to another via exchange of ions. The existing crystal lattice of the precursor crystals is used as template for the desired product as described by Dong *et al.*^[3] The K^+ ions in between the $\text{Fe}_{2-y}\text{Se}_2$ layers of $\text{K}_x\text{Fe}_{2-y}\text{Se}_2$ are replaced by layers of $[(\text{Li}_{0.8}\text{Fe}_{0.2})\text{OH}]^{0.2+}$.

Within this chapter the hydrothermal ion-exchange synthesis and the superconducting properties of large crystals $[(\text{Li}_{0.8}\text{Fe}_{0.2})\text{OH}]\text{FeSe}$ (edge length up to 8 mm) are reported.

Superconducting as well as non-superconducting crystals of $\text{K}_x\text{Fe}_{2-y}\text{Se}_2$ are prepared as precursor crystals and influences on the superconducting properties of the $[(\text{Li}_{0.8}\text{Fe}_{0.2})\text{OH}]\text{FeSe}$ crystals are investigated.

4.4.2 Experimental details

Crystal growth of $\text{K}_x\text{Fe}_{2-y}\text{Se}_2$ precursors

Crystals of $\text{K}_x\text{Fe}_{2-y}\text{Se}_2$ were prepared as precursors in a solid state synthesis similar to Ref. [4]. First, $\text{Fe}_{1.1}\text{Se}$ was pre-synthesized by reacting powders of Fe (1.32 g, 23.6 mmol) and Se (1.68 g, 21.3 mmol). The educts were mixed and ground, loaded in an alumina crucible, sealed in a quartz tube under argon atmosphere and heated at 750 °C for 20 h, followed by annealing at 320 °C for 55–65 h. The obtained product was ground, loaded in an alumina crucible together with 0.40 respectively 0.45 equivalents of K and sealed in a quartz tube under argon atmosphere. For additional protection, the quartz tube was sealed in a second quartz tube. The sample was put in a tubular resistance furnace, slowly heated to 1050 °C and held at this temperature for 3 h. Afterwards it was slowly cooled to 750 °C within 200 h to grow the crystals. A natural cooling to room temperature followed. The obtained, air-sensitive crystals with sizes up to 8 mm have a platelet form with shiny surfaces and were obtained through easy cleavage of the as-grown ingots.

Hydrothermal ion-exchange synthesis of $[(\text{Li}_{0.8}\text{Fe}_{0.2})\text{OH}]\text{FeSe}$ crystals

Similar to Ref. [3], $[(\text{Li}_{0.8}\text{Fe}_{0.2})\text{OH}]\text{FeSe}$ crystals were prepared by hydrothermal ion-exchange synthesis starting from $\text{K}_x\text{Fe}_{2-y}\text{Se}_2$ precursor crystals. 6–8 crystals $\text{K}_x\text{Fe}_{2-y}\text{Se}_2$ were selected and cautiously mixed with 0.15 g (2.7 mmol) Fe, 0.50 g (4.1 mmol) selenourea, 3 g (0.1 mol) $\text{LiOH}\cdot\text{H}_2\text{O}$ and 10 mL distilled water. The selenourea is added to create appropriate reducing conditions. The starting mixtures were tightly sealed in a teflon-lined steel autoclave (50 mL) and heated at 155 °C for 3–9 days. The obtained crystals were washed several times with distilled water and ethanol and stored at –25 °C under argon atmosphere.

4.4.3 Results and discussion

$K_x\text{Fe}_{2-y}\text{Se}_2$ precursor

Fig. 1 shows photographs of the grown $K_x\text{Fe}_{2-y}\text{Se}_2$ crystals with a size up to 8 mm. The layered structure of $K_x\text{Fe}_{2-y}\text{Se}_2$ is clearly visible in Fig. 2 where the corners of two large crystals are shown in a SEM image.

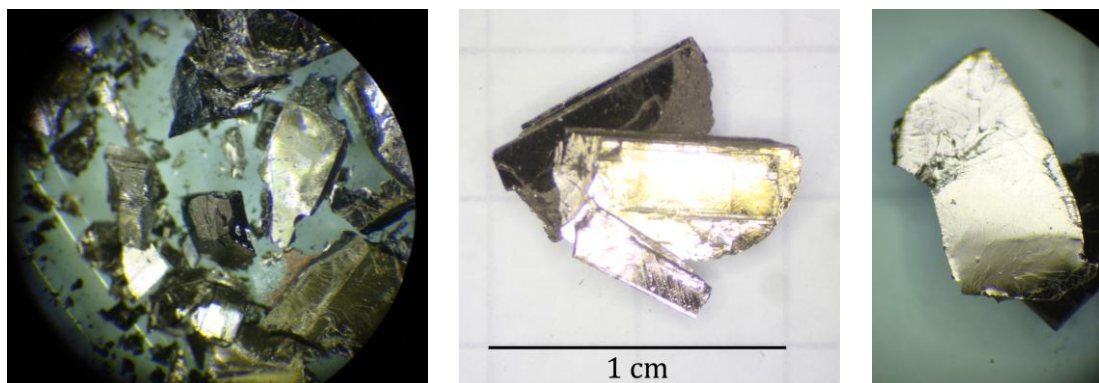


Fig. 1: Photographs of the grown $K_x\text{Fe}_{2-y}\text{Se}_2$ crystals.

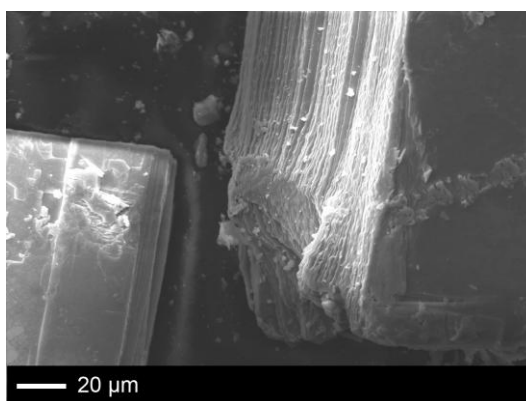


Fig. 2: SEM image of two corners of large $K_x\text{Fe}_{2-y}\text{Se}_2$ crystals, showing the layered structure.

The chemical composition of the two samples with different weighed portion of potassium was examined via EDX measurements. The studies uncover compositions of $\text{K}_{0.84(4)}\text{Fe}_{1.74(6)}\text{Se}_2$ and $\text{K}_{0.92(6)}\text{Fe}_{1.71(4)}\text{Se}_2$ for the samples with less and larger amount of nominal K, respectively. Some of the crystals were ground for powder X-ray diffractometry. Rietveld-refinement of the X-ray powder pattern (Fig. 3) confirms the structure of $K_x\text{Fe}_{2-y}\text{Se}_2$ and reveals a composition $\text{K}_{0.8(1)}\text{Fe}_{1.7(1)}\text{Se}_2$ and $\text{K}_{0.9(1)}\text{Fe}_{1.6(1)}\text{Se}_2$ respectively, which is in accordance with the results from EDX-measurements.

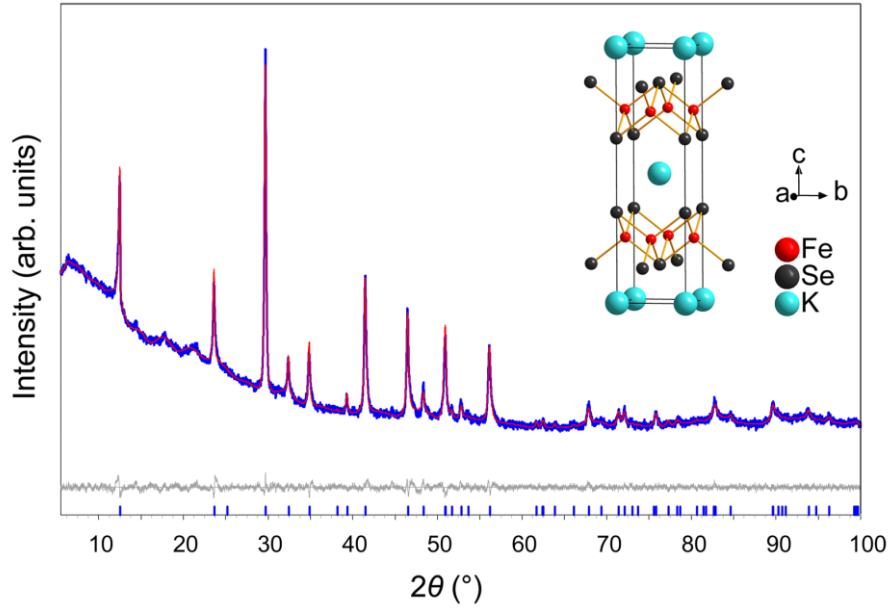


Fig. 3: X-ray powder pattern (blue) with Rietveld-fit (red) and difference curve (gray) of a ground crystal of $\text{K}_{0.9(1)}\text{Fe}_{1.6(1)}\text{Se}_2$. Inset: crystal structure of $\text{K}_x\text{Fe}_{2-y}\text{Se}_2$.

Even if the two compositions coincide within the error, such a slight difference might be responsible for differences in the transport properties. The composition as well as the microstructure of the non-stoichiometric compound $\text{K}_x\text{Fe}_{2-y}\text{Se}_2$ plays a crucial role on transport properties.^[4-7] Wang *et al.* showed that an increase of Fe concentrations (corresponding to the decrease of Fe deficiency) seems to be decisive for the appearance of superconductivity.^[4] Large concentrations of K are counterproductive and lead to a decreased Fe content. Microstructural analysis indicates that superconducting $\text{K}_x\text{Fe}_{2-y}\text{Se}_2$ consists of superconducting, Fe vacancy free filamentary paths in an antiferromagnetic $\text{K}_2\text{Fe}_4\text{Se}_5$ major phase with ordered Fe vacancies.^[7,8]

Here, superconducting as well as non-superconducting crystals as precursor for the synthesis of large superconducting $[(\text{Li}_{0.8}\text{Fe}_{0.2})\text{OH}]\text{FeSe}$ crystals are prepared. Susceptibility measurements (Fig. 4) reveal that the sample $\text{K}_{0.8(1)}\text{Fe}_{1.7(1)}\text{Se}_2$ with lower K and higher Fe content is bulk superconducting with $T_c = 31$ K whereas the sample $\text{K}_{0.9(1)}\text{Fe}_{1.6(1)}\text{Se}_2$ shows no sign of diamagnetism which is in accordance with literature.^[4]

By comparison of the resulting products after ion-exchange synthesis, the influence of the respective matrix crystals on the properties of the crystals $[(\text{Li}_{0.8}\text{Fe}_{0.2})\text{OH}]\text{FeSe}$ can be investigated.

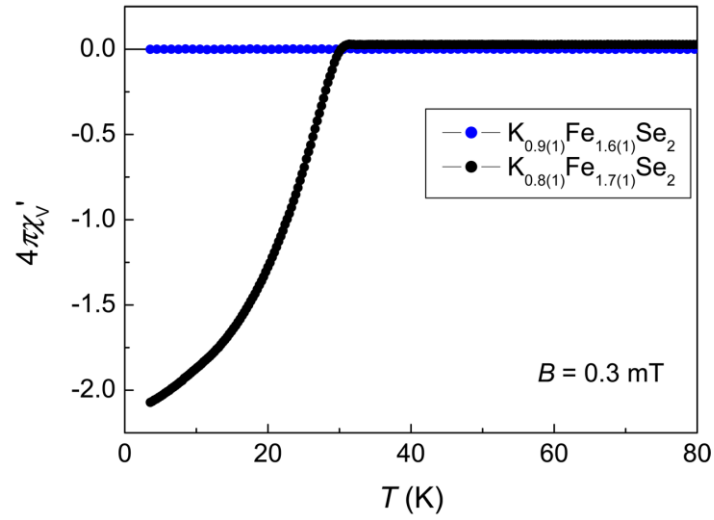


Fig. 4: Low-temperature AC-susceptibility of non-superconducting $\text{K}_{0.9(1)}\text{Fe}_{1.6(1)}\text{Se}_2$ (blue) and superconducting $\text{K}_{0.8(1)}\text{Fe}_{1.7(1)}\text{Se}_2$ (black) precursor crystals.

$[(\text{Li}_{0.8}\text{Fe}_{0.2})\text{OH}]\text{FeSe}$ crystals

Fig. 5 shows photographs of the synthesized $[(\text{Li}_{0.8}\text{Fe}_{0.2})\text{OH}]\text{FeSe}$ crystals in comparison to the precursor crystals.

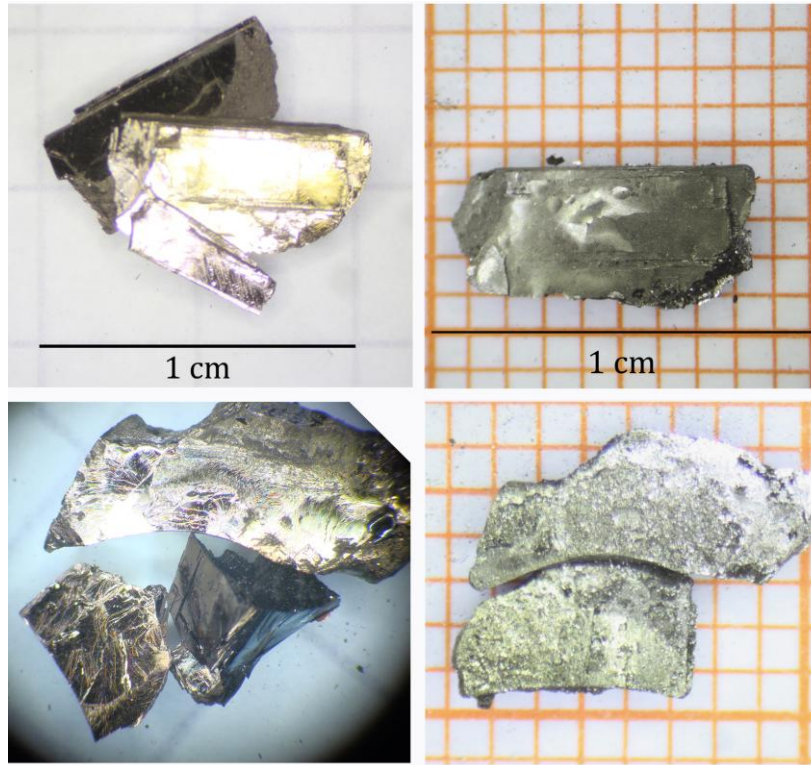


Fig. 5: Photographs of $[(\text{Li}_{0.8}\text{Fe}_{0.2})\text{OH}]\text{FeSe}$ crystals (right) in comparison to the precursor crystals $\text{K}_x\text{Fe}_{2-y}\text{Se}_2$ (left).

The $\text{K}_x\text{Fe}_{2-y}\text{Se}_2$ crystals serve as a kind of matrix for the hydrothermal ion exchange reaction and the resulting $[(\text{Li}_{0.8}\text{Fe}_{0.2})\text{OH}]\text{FeSe}$ crystals roughly inherit the original shape and size.^[3]

Rietveld-refinement of the X-ray powder pattern (Fig. 6) of some ground crystals confirms the structure of $[(\text{Li}_{0.8}\text{Fe}_{0.2})\text{OH}]\text{FeSe}$. A maximum of 2 % iron vacancies in the iron-selenide layer was refined. The obtained composition of $[(\text{Li}_{0.82(1)}\text{Fe}_{0.18(1)})\text{OH}]\text{Fe}_{0.98(1)}\text{Se}$ is in accordance with the results from EDX-measurements. Within the accuracy of EDX measurement and Rietveld-refinement no difference was observed in crystals resulting from superconducting and non-superconducting precursor crystals $\text{K}_{0.8(1)}\text{Fe}_{1.7(1)}\text{Se}_2$ and $\text{K}_{0.9(1)}\text{Fe}_{1.6(1)}\text{Se}_2$, respectively. The absence of K in EDX measurements reveals a complete transformation of the precursor crystals $\text{K}_x\text{Fe}_{2-y}\text{Se}_2$.

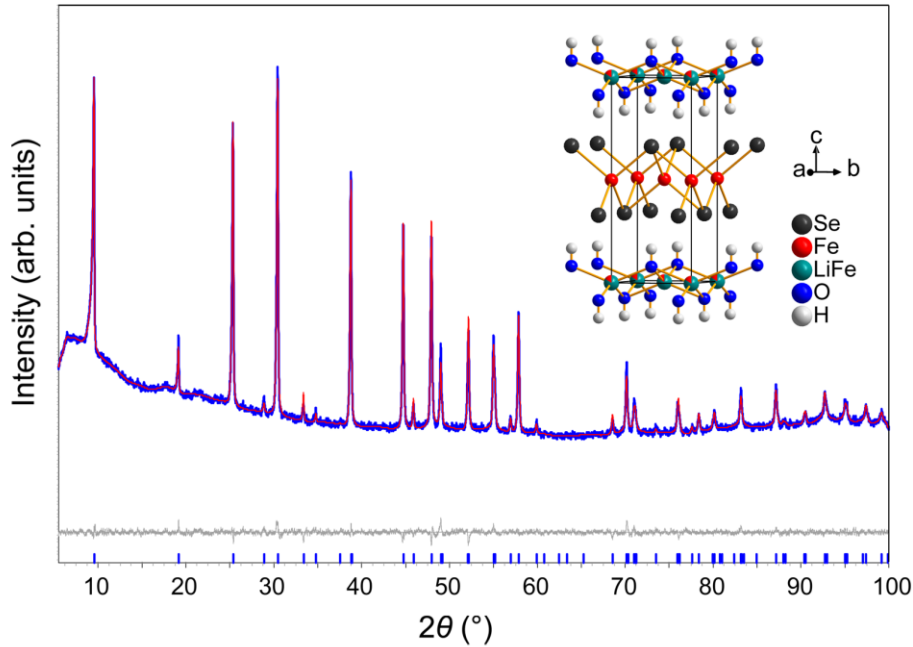


Fig. 6: X-ray powder pattern (blue) with Rietveld-fit (red) and difference curve (gray) of a ground $[(\text{Li}_{0.8}\text{Fe}_{0.2})\text{OH}]\text{FeSe}$ crystal. Inset: crystal structure of $[(\text{Li}_{0.8}\text{Fe}_{0.2})\text{OH}]\text{FeSe}$.

Fig. 7 exemplarily shows the AC-susceptibilities of two crystals $[(\text{Li}_{0.8}\text{Fe}_{0.2})\text{OH}]\text{FeSe}$ resulting from superconducting (black) and non-superconducting (blue) precursor crystals. Both susceptibilities show a sharp superconducting transition at about 41 K, in accordance with results from polycrystalline samples. The superconducting volume fractions of -8 respectively -17 at 3.5 K are unreasonably large and result from neglect of demagnetization effects. The large crystals have a thin, platelet shaped habit with a distinct aspect ratio.

According to

$$\chi_{\text{exp}} = \frac{\chi_{\text{intr}}}{1+N\chi_{\text{intr}}} \quad (1)$$

with χ_{exp} is the experimentally observed susceptibility, χ_{intr} the intrinsic susceptibility and N the shape-dependent demagnetizing factor of the sample,^[9] the impact of the sample's shape on the measured data can be estimated. In the full Meissner state, i.e. for $\chi_{\text{intr}} = -1$, one obtains

$$\chi_{\text{exp}} = -\frac{1}{1-N}. \quad (2)$$

For infinitely flat platelets with H perpendicular to the broad surface, the demagnetizing factor approaches one. Accordingly, it becomes obvious that χ_{exp} is largely overrated for thin, platelet shaped crystals oriented perpendicular to the magnetic field.

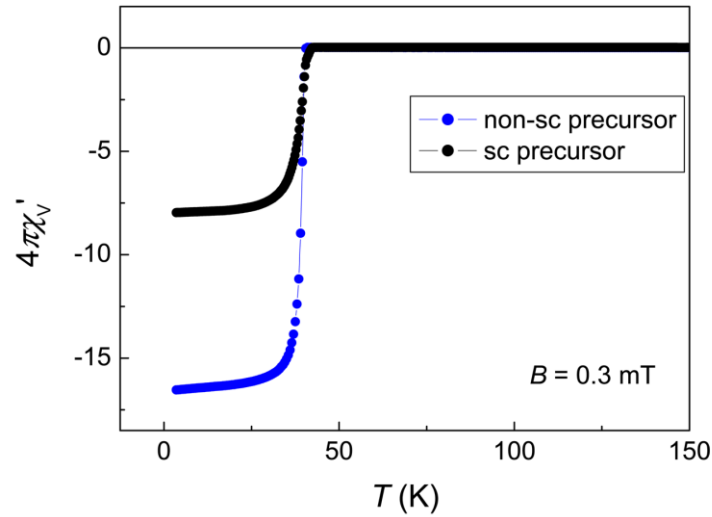


Fig. 7: Low-temperature AC-susceptibility of $[(\text{Li}_{0.8}\text{Fe}_{0.2})\text{OH}]\text{FeSe}$ crystals obtained from non-superconducting (blue) and superconducting (black) precursor crystals $\text{K}_x\text{Fe}_{2-y}\text{Se}_2$.

As both values exceed 100 % in the measurement, the difference in the superconducting volume fraction of both samples is most probably due to a difference in the aspect ratio and/or the orientation of the platelets in terms of the magnetic field. Apart from this, no distinct difference in the susceptibility of both samples is observed. Thus, the superconducting or non-superconducting properties, correlated with the microstructure of the precursor crystals seem to be of no distinct importance for the properties of the $[(\text{Li}_{0.8}\text{Fe}_{0.2})\text{OH}]\text{FeSe}$ crystals. Obviously, most of the vacancies in the FeSe layer of $\text{K}_x\text{Fe}_{2-y}\text{Se}_2$

are filled during hydrothermal reaction leading to more or less intact layers without the above mentioned phase separation of superconducting filaments and antiferromagnetic matrix.

In contrast to the polycrystalline samples described in chapter 4.1, the AC-susceptibility of the large crystals $[(\text{Li}_{0.8}\text{Fe}_{0.2})\text{OH}]\text{FeSe}$ does not show a ferromagnetic signal in the temperature range around 10 K. This can be explained by the orientation of the platelet shaped crystals in terms of the magnetic field and the magnetic anisotropy. Fig. 8 illustrates this magnetic anisotropy showing the AC-susceptibility of a ground crystal $[(\text{Li}_{0.8}\text{Fe}_{0.2})\text{OH}]\text{FeSe}$ where the ferromagnetic signal is visible.

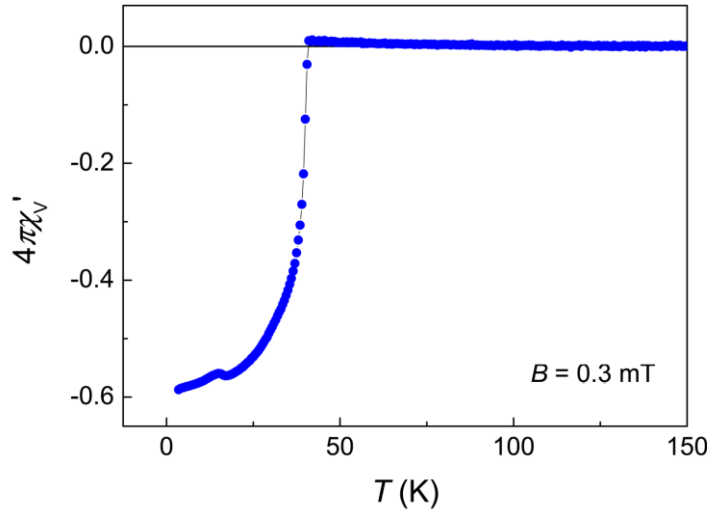


Fig. 8: Low-temperature AC-susceptibility of a ground $[(\text{Li}_{0.8}\text{Fe}_{0.2})\text{OH}]\text{FeSe}$ crystal.

Fig. 9 shows the influence of reaction time during hydrothermal ion-exchange reaction on the superconducting transition temperature of the $[(\text{Li}_{0.8}\text{Fe}_{0.2})\text{OH}]\text{FeSe}$ crystals. It is obvious that T_c decreases with reaction times longer than 3 days, thus a short heating time is preferable in order to optimize T_c . The reason for this decline of the superconducting properties might be a continuous increase of iron vacancies in the FeSe layer of $[(\text{Li}_{0.8}\text{Fe}_{0.2})\text{OH}]\text{FeSe}$.^[10]

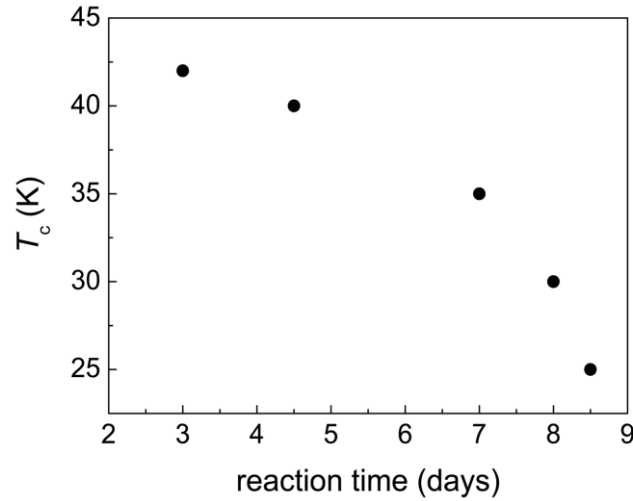


Fig. 9: Development of T_c with hydrothermal ion-exchange reaction time.

4.4.4 Conclusion

Large crystals of $[(\text{Li}_{0.8}\text{Fe}_{0.2})\text{OH}]\text{FeSe}$ with a size up to 8 mm were prepared by hydrothermal ion-exchange synthesis, starting from $\text{K}_x\text{Fe}_{2-y}\text{Se}_2$ precursor crystals. The obtained crystals are well applicable for future physical measurements like ARPES or orientation dependent μSR measurements.

The presence or absence of superconductivity, correlated with the microstructure in the precursor crystals, is of no distinct importance for the properties of the $[(\text{Li}_{0.8}\text{Fe}_{0.2})\text{OH}]\text{FeSe}$ crystals. In contrast, hydrothermal ion-exchange reaction times longer than 3 days lead to a continuous decrease of T_c .

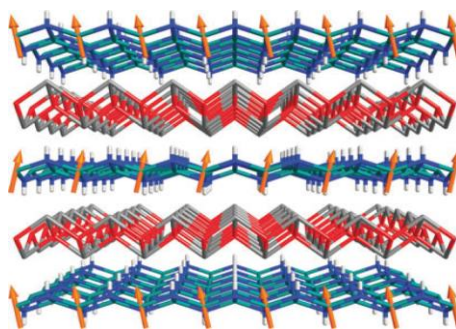
4.4.5 References

- [1] G. Dhanaraj, K. Byrappa, V. Prasad, M. Dudley, *Springer Handbook of Crystal Growth, Vol. 1*, Springer-Verlag Berlin Heidelberg, **2010**.
- [2] A. Damascelli, Z. Hussain, Z.-X. Shen, *Reviews of Modern Physics* **2003**, 75, 473-541.
- [3] X. Dong, K. Jin, D. Yuan, H. Zhou, J. Yuan, Y. Huang, W. Hua, J. Sun, P. Zheng, W. Hu, Y. Mao, M. Ma, G. Zhang, F. Zhou, Z. Zhao, *Physical Review B* **2015**, 92, 064515.
- [4] D. M. Wang, J. B. He, T. L. Xia, G. F. Chen, *Physical Review B* **2011**, 83, 132502.
- [5] P. Cai, C. Ye, W. Ruan, X. Zhou, A. Wang, M. Zhang, X. Chen, Y. Wang, *Physical Review B* **2012**, 85, 094512.
- [6] S. V. Carr, D. Louca, J. Siewenie, Q. Huang, A. Wang, X. Chen, P. Dai, *Physical Review B* **2014**, 89, 134509.

-
- [7] X. Ding, D. Fang, Z. Wang, H. Yang, J. Liu, Q. Deng, G. Ma, C. Meng, Y. Hu, H.-H. Wen, *Nature Communications* **2013**, *4*, 1897.
- [8] S. C. Speller, T. B. Britton, G. M. Hughes, A. Krzton-Maziopa, E. Pomjakushina, K. Conder, A. T. Boothroyd, C. R. M. Grovenor, *Superconductor Science and Technology* **2012**, *25*, 084023.
- [9] M. Wacenovsky, H. W. Weber, O. B. Hyun, D. K. Finnemore, K. Mereiter, *Physica C* **1989**, *160*, 55-64.
- [10] H. Sun, D. N. Woodruff, S. J. Cassidy, G. M. Allcroft, S. J. Sedlmaier, A. L. Thompson, P. A. Bingham, S. D. Forder, S. Cartenet, N. Mary, S. Ramos, F. R. Foronda, B. H. Williams, X. Li, S. J. Blundell, S. J. Clarke, *Inorganic Chemistry* **2015**, *54*, 1958-1964.

4.5 $[(\text{Li}_{0.8}\text{Fe}_{0.2})\text{OH}]\text{FeS}$ and the ferromagnetic superconductors $[(\text{Li}_{0.8}\text{Fe}_{0.2})\text{OH}]\text{Fe}(\text{S}_{1-x}\text{Se}_x)$

Ursula Pachmayr and Dirk Johrendt



published in: *Chemical Communications* **2015**, 51, 4689.

Copyright 2015, Royal Society of Chemistry.

Abstract

Superconductivity up to 43 K and ferromagnetic ordering coexist in the iron chalcogenides $[(\text{Li}_{0.8}\text{Fe}_{0.2})\text{OH}]\text{Fe}(\text{S}_{1-x}\text{Se}_x)$ ($0 < x \leq 1$). Substitution of sulfur for selenium gradually suppresses superconductivity while ferromagnetism persists up to non-superconducting $[(\text{Li}_{0.8}\text{Fe}_{0.2})\text{OH}]\text{FeS}$.

4.5.1 Introduction

A conclusive understanding of unconventional superconductivity in correlated electron systems is among the most challenging topics in contemporary solid state chemistry and physics.^[1] In copper-oxide^[2] and iron-based^[3] materials, superconductivity emerges close to the disappearance of an antiferromagnetically ordered ground state,^[4, 5] leading to the assumption that magnetism plays a crucial role in the formation of the cooper pairs.^[6] In contrast, superconductivity is generally considered incompatible with ferromagnetism. The latter generates magnetic flux, while superconductivity expels magnetic flux from the interior of a solid. Nevertheless, a few examples where both forms of order coexist are

known (see Ref. 1-14 in Ref. [7]). However, a detailed examination of these fascinating coexistence phenomena is mostly aggravated by extremely low transition temperatures, as well as by the chemical inertness of the rare-earth $4f$ shell.

Recently we reported the ferromagnetic iron selenide superconductor $[(\text{Li}_{0.8}\text{Fe}_{0.2})\text{OH}]\text{FeSe}$.^[7] The crystal structure exhibits alternately stacked lithium-iron-hydroxide layers and iron selenide layers, and was contemporaneously observed by Lu *et al.*^[8] and Sun *et al.*^[9] Electron doping of the FeSe layer is most probably the main reason for the enormous increase of T_c from 8 K in $\beta\text{-FeSe}$ ^[10] to 43 K in $[(\text{Li}_{0.8}\text{Fe}_{0.2})\text{OH}]\text{FeSe}$. Similar effects were found in other intercalated iron selenides like $\text{Li}_x(\text{NH}_2)_y(\text{NH}_3)_{1-y}\text{Fe}_2\text{Se}_2$ ^[11] or $\text{Li}_x(\text{C}_5\text{H}_5\text{N})_y\text{F}_{2-z}\text{Se}_2$.^[12] However, the coexistence of unconventional superconductivity and ferromagnetism in $[(\text{Li}_{0.8}\text{Fe}_{0.2})\text{OH}]\text{FeSe}$ is exceptional. Even though the internal dipole field of the ferromagnet acts on the superconductor, superconductivity is not suppressed. Control over one of these order parameters would give the opportunity to examine the fascinating interplay i.e. the competition, coexistence and coupling of ferromagnetism and superconductivity in more detail.

In this communication we present the chalcogenides $[(\text{Li}_{0.8}\text{Fe}_{0.2})\text{OH}]\text{Fe}(\text{S}_{1-x}\text{Se}_x)$ ($0 \leq x < 1$). We show that the gradual substitution of selenium by sulfur continuously reduces the critical temperature until superconductivity is absent in the pure sulfide. This allows studying the influence of chemical pressure, and in particular possible effects on the coexistence of superconductivity and ferromagnetism.

4.5.2 Experimental details

Polycrystalline samples of $[(\text{Li}_{0.8}\text{Fe}_{0.2})\text{OH}]\text{Fe}(\text{S}_{1-x}\text{Se}_x)$ were synthesized under hydrothermal conditions.^[7] Iron metal (0.0851 g, 1.524 mmol), $\text{LiOH}\cdot\text{H}_2\text{O}$ (3 g, 0.1 mmol) and appropriate amounts of thiourea respectively selenourea were mixed with distilled water (10 mL). The starting mixtures were tightly sealed in a teflon-lined steel autoclave (50 mL) and heated at 155 °C for 7 days. After washing with distilled water and ethanol, the polycrystalline products were dried at room temperature under dynamic vacuum and stored at -25 °C under argon atmosphere.

4.5.3 Results and discussion

Structural characterization by X-ray powder diffraction (PXRD) revealed single phase samples of $[(\text{Li}_{0.8}\text{Fe}_{0.2})\text{OH}]\text{Fe}(\text{S}_{1-x}\text{Se}_x)$ which is isostructural to the selenide.^[7-9] Fig. 1 shows

the X-ray powder pattern with Rietveld-fit as well as the crystal structure of $[(\text{Li}_{0.8}\text{Fe}_{0.2})\text{OH}]\text{FeS}$.

The tetragonal structure consists of *anti*-PbO type layers of lithium-iron-hydroxide alternating with FeS layers. X-ray single crystal analysis confirms the structure (see Tab. 1 in chapter 8.3).

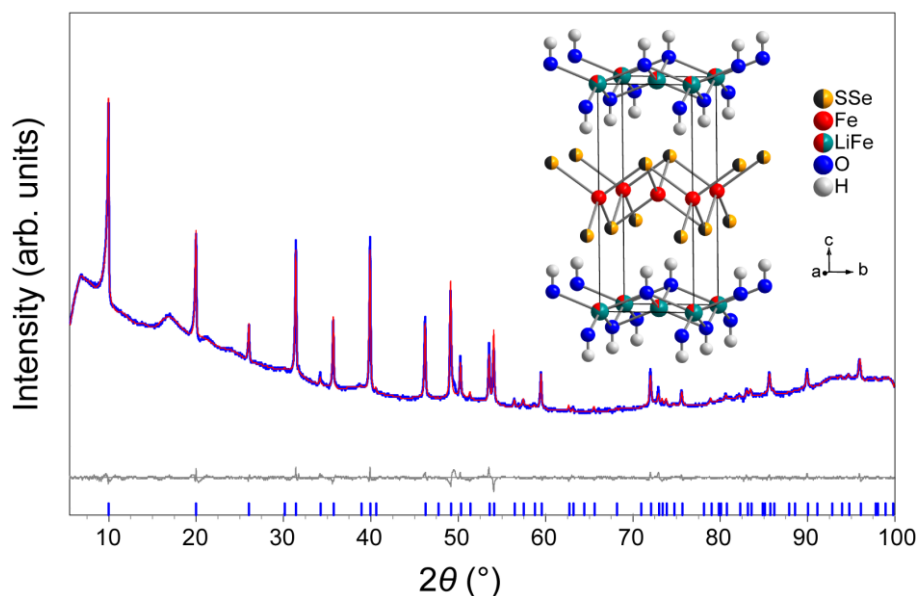


Fig. 1: X-ray powder pattern of $[(\text{Li}_{0.8}\text{Fe}_{0.2})\text{OH}]\text{FeS}$ (blue) with Rietveld-fit (red) and difference curve (gray). Inset: crystal structure of $[(\text{Li}_{0.8}\text{Fe}_{0.2})\text{OH}]\text{Fe}(\text{S}_{1-x}\text{Se}_x)$.

Fig. 2 gives an overview of some X-ray powder patterns of $[(\text{Li}_{0.8}\text{Fe}_{0.2})\text{OH}]\text{Fe}(\text{S}_{1-x}\text{Se}_x)$ ($0 \leq x \leq 1$). The compositions of all compounds were confirmed combining energy dispersive X-ray spectroscopy (EDX) measurements, inductively coupled plasma (ICP) analysis and elementary analysis. Remarkably, the composition of the $(\text{Li}_{1-x}\text{Fe}_x)\text{OH}$ layer is the same as for $[(\text{Li}_{0.8}\text{Fe}_{0.2})\text{OH}]\text{FeSe}$ ^[7-9] which means that the same charge transfer of 0.2 electrons takes place in the sulfide.

An open issue regarding the crystal structure is the large U_{33} component of the thermal displacement ellipsoid at the Fe/Li mixed site. This was also observed by Sun *et al.*,^[9] and may be interpreted as a split position with Li shifted off the center of the oxygen tetrahedra along $[001]$ (see chapter 4.3). Contrary to $[(\text{Li}_{0.8}\text{Fe}_{0.2})\text{OH}]\text{FeSe}$ where iron vacancies in the FeSe layer exist,^[7] refinements of X-ray single crystal diffraction data give no indication of iron vacancies in sulfur doped compounds. Sun *et al.* suggested that the lattice parameter a decreases with decreasing amount of Fe vacancies in the FeSe layer.^[9] The lattice parameter

a of $[(\text{Li}_{0.8}\text{Fe}_{0.2})\text{OH}]\text{FeS}$ is 370 pm, distinctly smaller compared to the selenides with $a = 378\text{--}382$ pm,^[9] thus iron vacancies in the FeS layer are rather unlikely.

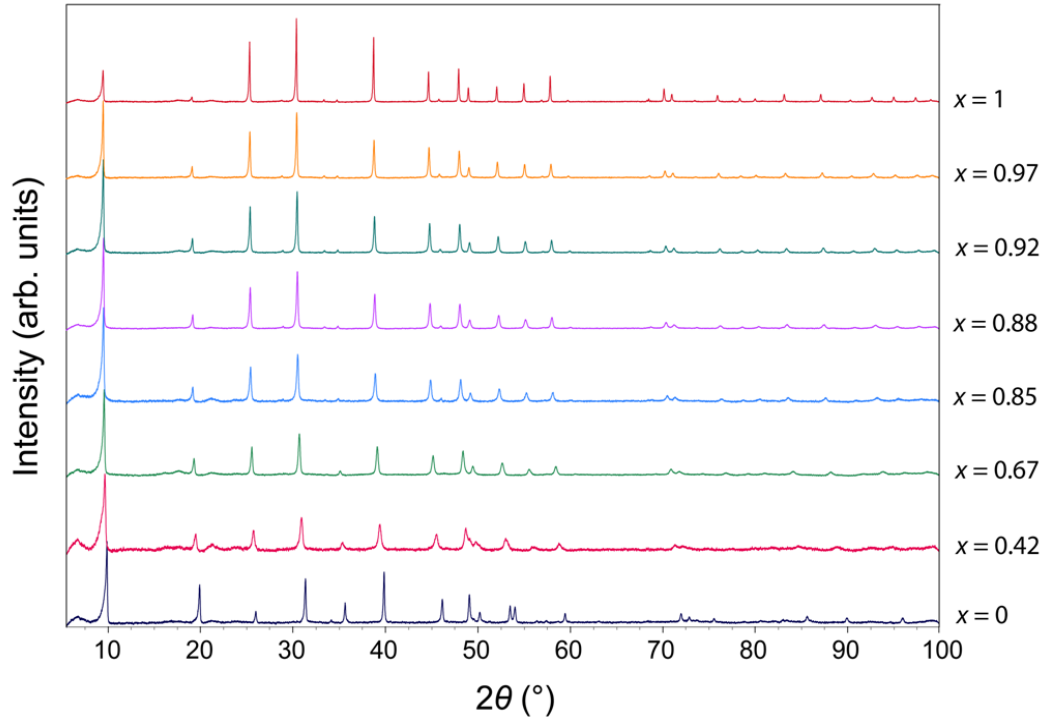


Fig. 2: X-ray powder patterns of $[(\text{Li}_{0.8}\text{Fe}_{0.2})\text{OH}]\text{Fe}(\text{S}_{1-x}\text{Se}_x)$ ($0 \leq x \leq 1$).

The lattice parameters as well as the unit cell volumes of $[(\text{Li}_{0.8}\text{Fe}_{0.2})\text{OH}]\text{Fe}(\text{S}_{1-x}\text{Se}_x)$ increase linearly with the doping level x as shown in Fig. 3. The linear behavior of a and c within the whole doping range $0 \leq x < 1$ indicates homogeneous doping of sulfur, however, the pure sulfide slightly deviates from linearity. The shrinking of the unit cell due to the smaller ionic radius of sulfur is also known from *anti*-PbO type $\text{Fe}(\text{Se}_{1-z}\text{S}_z)$ ($z = 0\text{--}0.5$) with a possible solubility limit of $z \approx 0.3$.^[13]

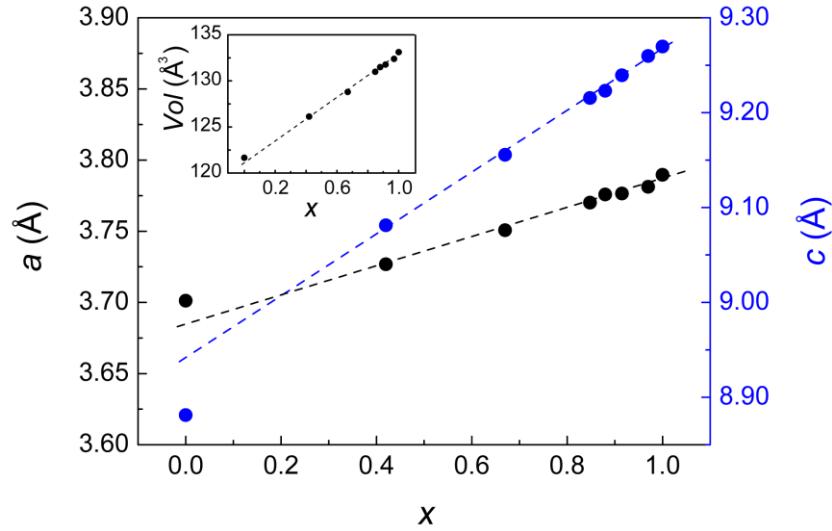


Fig. 3: Lattice parameters a (black) and c (blue) of $[(\text{Li}_{0.8}\text{Fe}_{0.2})\text{OH}]\text{Fe}(\text{S}_{1-x}\text{Se}_x)$. Inset: unit cell volume. Dashed lines are guides to the eye.

The critical temperature of $\text{Fe}(\text{Se}_{1-x}\text{S}_x)$ increases up to 15.5 K for $x \leq 0.2$ due to chemical pressure.^[13] T_c decreases again at $x \geq 0.3$, thus it remains much smaller under chemical than under physical pressure (36 K).^[14] In contrast, sulfur-doping of $[(\text{Li}_{0.8}\text{Fe}_{0.2})\text{OH}]\text{Fe}(\text{S}_{1-x}\text{Se}_x)$ continuously decreases T_c linearly, until superconductivity is completely suppressed in the pure sulfide, as seen from the DC electrical transport measurements in Fig. 4. The DC-resistivity of the pure selenide compound is weakly temperature dependent until it drops abruptly at 43 K (lower panel in Fig. 4). For $x = 0.88$ the resistivity drop is shifted to 37 K, and a shoulder appears at about 20 K, which is most probably due to the magnetic ordering of the Fe moments in the $(\text{Li}_{0.8}\text{Fe}_{0.2})\text{OH}$ layer (see below). The relatively large increase of resistivity above the superconducting transition is due to grain boundary effects, because cold pressed pellets have to be used owing to the temperature sensibility of the compounds. For $x = 0.42$ a distinct drop in resistivity is discernible at about 15 K, which is in good agreement with magnetic susceptibility measurements. As in this case the superconducting transition temperature coincides with the temperature range where the ferromagnetic ordering arises, the decrease in resistivity is rather broad. A tiny residual resistivity is observed, caused by grain boundary effects of the cold pressed pellets. Undoped $[(\text{Li}_{0.8}\text{Fe}_{0.2})\text{OH}]\text{FeS}$ shows no sign of a superconducting transition, which is in line with the magnetic susceptibility measurements. However, a slight increase in resistivity can be observed at low temperatures, which might be again due to the gradual magnetic ordering in the $(\text{Li}_{0.8}\text{Fe}_{0.2})\text{OH}$ layer.

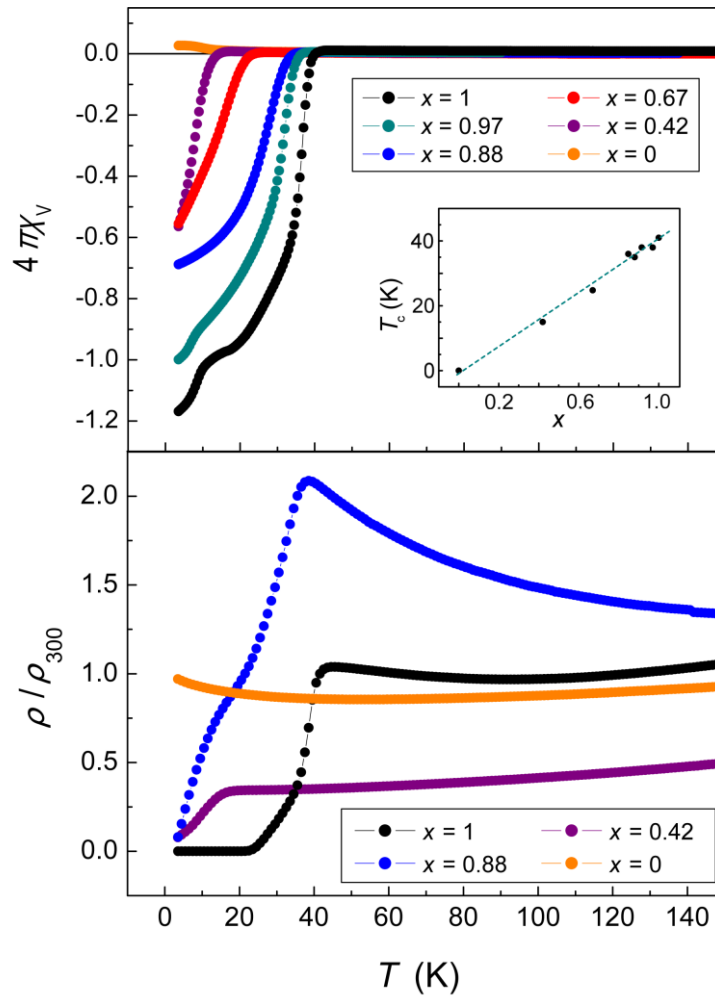


Fig. 4: Top: AC-susceptibility of $[(\text{Li}_{0.8}\text{Fe}_{0.2})\text{OH}]\text{Fe}(\text{S}_{1-x}\text{Se}_x)$. Inset: development of T_c with x . Bottom: DC resistivity for $x = 0$ (orange), 0.42 (magenta), 0.88 (blue) and 1 (black).

The enormous increase of T_c in $[(\text{Li}_{0.8}\text{Fe}_{0.2})\text{OH}]\text{FeSe}$ (43 K) in comparison to $\beta\text{-FeSe}$ (8 K) can be explained by electron doping from the hydroxide to the selenide layer.^[7] By substituting Se by S this electron doping doesn't change as Se and S ions have the same valence and the composition of the hydroxide layer remains constant. Though, the smaller S atoms lead to a chemical pressure effect, which additionally influences superconductivity. Contrary to $\text{Fe}(\text{Se}_{1-x}\text{S}_x)$ where chemical pressure enhances superconductivity, we observe a decrease of T_c with increasing chemical pressure. Apparently in our case the geometry of the tetrahedral $\text{Fe}(\text{S}_{1-x}\text{Se}_x)$ layer is not further optimized. With increasing amount of S the unit cell volume and the Fe-Fe as well as the Fe-(Se,S) distances shrink. Contemplating the $Ch\text{-Fe-}Ch$ bond angles of the FeCh_4 tetrahedra, a flattening of the $\text{Fe}(\text{S}_{1-x}\text{Se}_x)$ layers with increasing sulfur doping is observed (Fig. 5). A definitive clue which parameter is crucial with respect to T_c

cannot be given at this point. However, an enlargement of the unit cell with the respective opposite evolutions in geometry of the FeSe layer by substituting Se by Te seems quite promising in view of an enhancement of T_c .

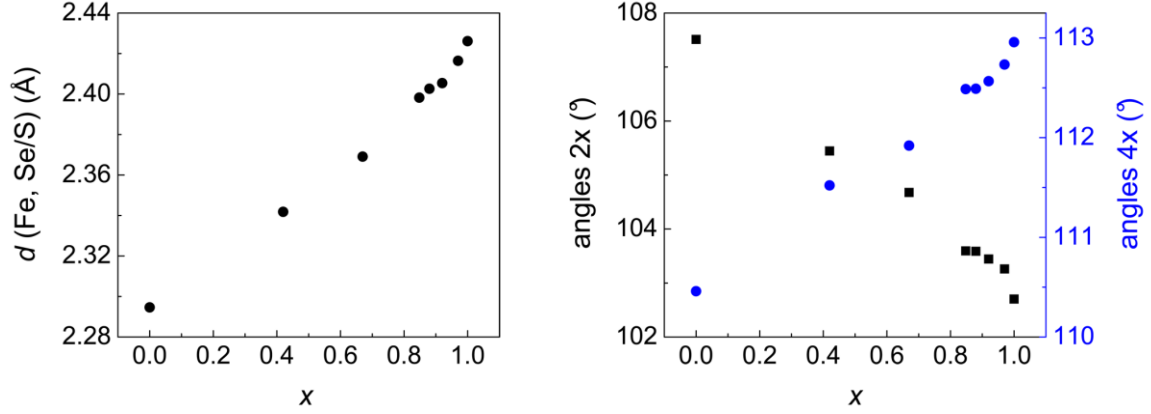


Fig. 5: Evolution of Fe–Oh distances (left) and Oh–Fe–Oh bond angles (right) in $[(\text{Li}_{0.8}\text{Fe}_{0.2})\text{OH}]\text{Fe}(\text{S}_{1-x}\text{Se}_x)$ ($0 \leq x \leq 1$).

The possible coexistence of superconductivity and ferromagnetism in the series $[(\text{Li}_{0.8}\text{Fe}_{0.2})\text{OH}]\text{Fe}(\text{S}_{1-x}\text{Se}_x)$ is of particular interest. In $[(\text{Li}_{0.8}\text{Fe}_{0.2})\text{OH}]\text{FeSe}$ magnetic ordering emerges from the iron ions in the hydroxide layer at about 10 K, well below the superconducting transition temperature at 43 K. In contrast to the suppression of the critical temperature with increasing sulfur doping, ferromagnetism persists over the whole substitution range. Fig. 6 shows the magnetic susceptibility of $[(\text{Li}_{0.8}\text{Fe}_{0.2})\text{OH}]\text{FeS}$ (black) and doped samples. Selenium rich compounds show a strong diamagnetic signal in a 3 mT field analogous to $[(\text{Li}_{0.8}\text{Fe}_{0.2})\text{OH}]\text{FeSe}$ in the zero-field cooled mode (zfc, Fig. 6) where the shielding effect is strong. After field-cooling (fc, Fig. 6) the susceptibility becomes merely slightly negative below T_c owing to the Meissner-Ochsenfeld effect before increasing to positive values at lower temperatures. This behavior is known from $[(\text{Li}_{0.8}\text{Fe}_{0.2})\text{OH}]\text{FeSe}$ and a result of the coexistence of ferromagnetism and superconductivity.^[7]

The susceptibility of undoped $[(\text{Li}_{0.8}\text{Fe}_{0.2})\text{OH}]\text{FeS}$ is throughout positive as superconductivity is completely suppressed. Nevertheless, for low temperatures we also observe a different signal in zfc and fc mode, respectively (see inset in Fig. 6). This splitting is typical for ferromagnetic ordering and caused by different domain formations in fc and zfc modes. Below $T_c \approx 10$ K, the magnetic moments order spontaneously leading to an increase

in magnetic susceptibility. In zfc mode, the domains are randomly distributed. Switching on the external field the domains tend to orientate along the field which is only partially accomplished. As a result the signal is lower compared to fc mode where the domains can align in the field during the cooling cycle.

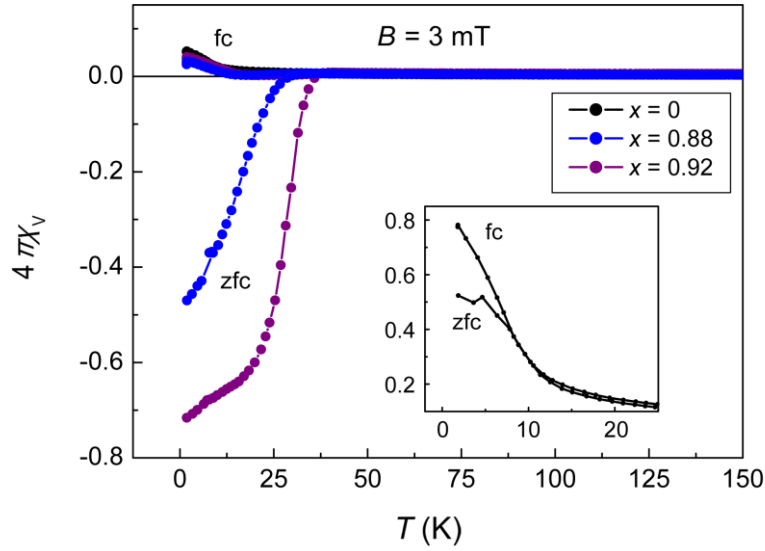


Fig. 6: Magnetic DC-susceptibility of $[(\text{Li}_{0.8}\text{Fe}_{0.2})\text{OH}]\text{Fe}(\text{S}_{1-x}\text{Se}_x)$ for $x = 0$ (black), 0.88 (blue) and 0.92 (magenta). Inset: magnification of the low-temperature part for $x = 0$.

The inverse susceptibility of $[(\text{Li}_{0.8}\text{Fe}_{0.2})\text{OH}]\text{FeS}$ at 2 T obeys the Curie-Weiss law with an effective paramagnetic moment of $4.98(1) \mu_B$ (see Fig. 7).

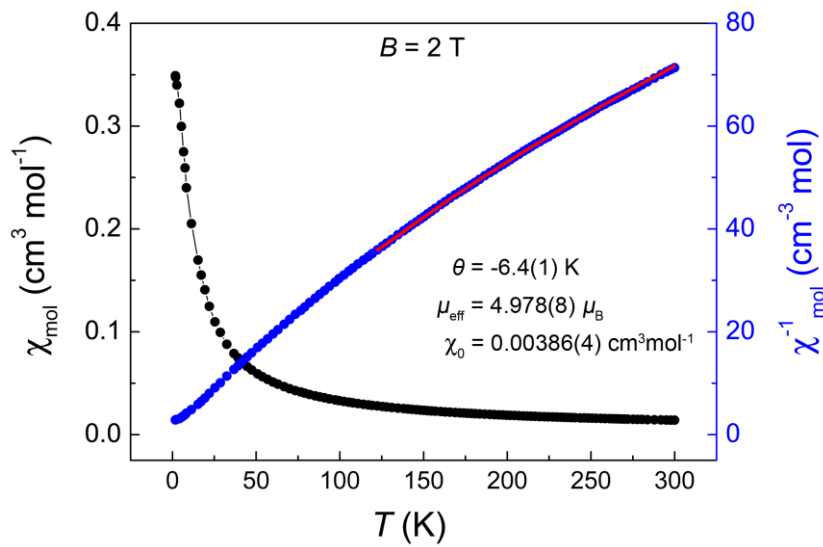


Fig. 7: Susceptibility (black) and inverse susceptibility (blue) at 2 T with Curie-Weiss fit (red line) for $\text{Li}_4\text{Fe}(\text{OH})_5(\text{FeS})_5$.

This value is in good agreement with the theoretically expected one of $4.90 \mu_B$ for Fe^{2+} contrary to the one of Fe^{3+} ($5.92 \mu_B$).^[15] Thus, the situation of the iron ions in the hydroxide layer is unchanged. The electron transfer to the $\text{Fe}(\text{S}_{1-x}\text{Se}_x)$ layer and magnetic ordering in the $(\text{Li}_{0.8}\text{Fe}_{0.2})\text{OH}$ layer persist in $[(\text{Li}_{0.8}\text{Fe}_{0.2})\text{OH}]\text{Fe}(\text{S}_{1-x}\text{Se}_x)$ in the whole substitution range.

The interplay of magnetism and superconductivity is further confirmed by magnetization measurements (Fig. 8). The ferromagnetic hysteresis of $[(\text{Li}_{0.8}\text{Fe}_{0.2})\text{OH}]\text{Fe}(\text{S}_{1-x}\text{Se}_x)$ with $x > 0$ is superimposed by the magnetization known for hard type-II superconductors.^[7] The initial curves prove superconductivity in the Se containing compounds, which is in line with susceptibility measurements. Decreasing the amount of Se, the superconducting hysteresis continuously diminishes. As expected from susceptibility measurements, $[(\text{Li}_{0.8}\text{Fe}_{0.2})\text{OH}]\text{FeS}$ shows only the ferromagnetic ordering with a very narrow hysteresis typical for a soft ferromagnet. We suppose that the reason for this is the dilution of the magnetic iron ions in the hydroxide layer leading to small coupling.

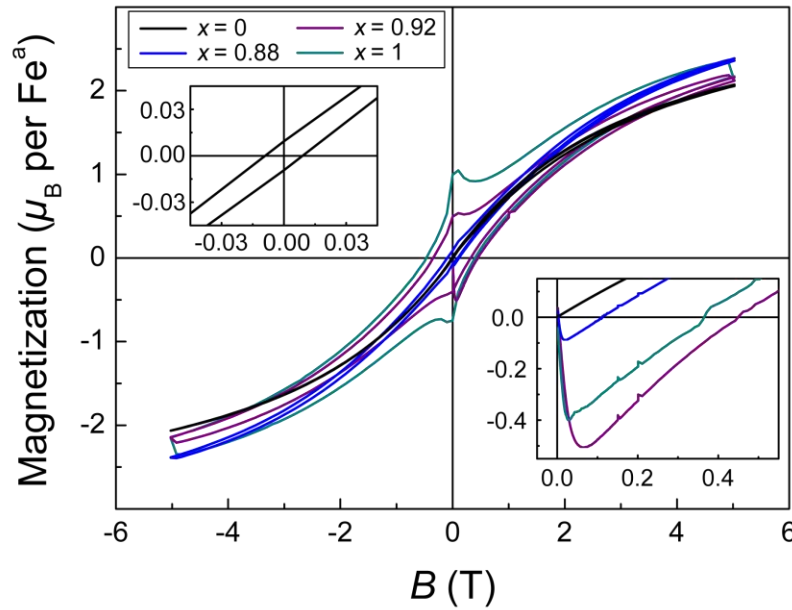


Fig. 8: Isothermal magnetization at 1.8 K of $[(\text{Li}_{0.8}\text{Fe}_{0.2})\text{OH}]\text{Fe}(\text{S}_{1-x}\text{Se}_x)$ for $x = 0$ (black), 0.88 (blue), 0.92 (magenta) and 1 (dark cyan). Inset: magnification of the low-field part showing the hysteresis for $x = 0$ (left inset) and the initial curves (right inset).

4.5.4 Conclusion

$[(\text{Li}_{0.8}\text{Fe}_{0.2})\text{OH}]\text{FeS}$ and the series $[(\text{Li}_{0.8}\text{Fe}_{0.2})\text{OH}]\text{Fe}(\text{S}_{1-x}\text{Se}_x)$ were synthesized by hydrothermal methods and characterized by X-ray single crystal and powder diffraction, EDX and chemical analysis. Selenium-rich compounds show coexistence of magnetic ordering with superconductivity as known from the pure selenium compound. Sulfur doping decreases the critical temperature through chemical pressure until superconductivity is completely absent in $[(\text{Li}_{0.8}\text{Fe}_{0.2})\text{OH}]\text{FeS}$, while ferromagnetism persists in the $(\text{Li}_{0.8}\text{Fe}_{0.2})\text{OH}$ layers. The Li:Fe ratio in the hydroxide layer and thus the charge transfer of 0.2 electrons from the hydroxide to the iron chalcogenide layers remains unchanged in $[(\text{Li}_{0.8}\text{Fe}_{0.2})\text{OH}]\text{Fe}(\text{S}_{1-x}\text{Se}_x)$, which indicates that the chemical pressure effect of the smaller sulfide ions impedes superconductivity in $[(\text{Li}_{0.8}\text{Fe}_{0.2})\text{OH}]\text{FeS}$.

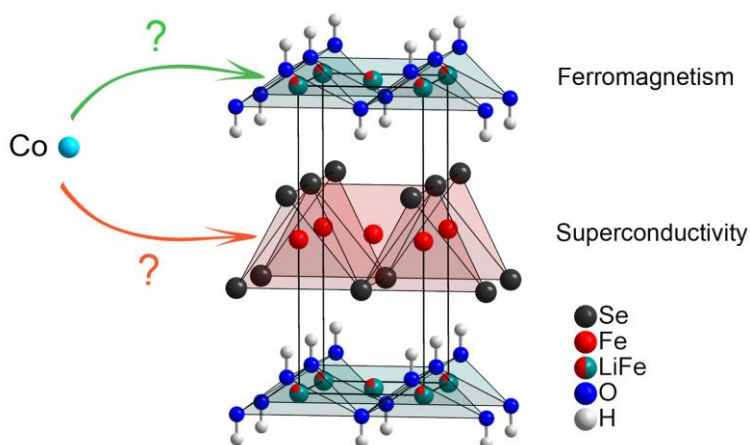
4.5.5 References

- [1] M. Sigrist, K. Ueda, *Reviews of Modern Physics* **1991**, 63, 239-311.
- [2] R. Hackl, *Zeitschrift für Kristallographie* **2011**, 226, 323.
- [3] D. Johrendt, R. Pöttgen, *Angewandte Chemie International Edition* **2008**, 47, 4782-4784.
- [4] D. Johrendt, *Journal of Materials Chemistry* **2011**, 21, 13726-13736.
- [5] G. Stewart, *Reviews of Modern Physics* **2011**, 83, 1589-1652.
- [6] Y. Shun-Li, L. Jian-Xin, *Chinese Physics B* **2013**, 22, 87411-087411.
- [7] U. Pachmayr, F. Nitsche, H. Luetkens, S. Kamusella, F. Brückner, R. Sarkar, H.-H. Klauss, D. Johrendt, *Angewandte Chemie International Edition* **2015**, 54, 293-297.
- [8] X. F. Lu, N. Z. Wang, H. Wu, Y. P. Wu, D. Zhao, X. Z. Zeng, X. G. Luo, T. Wu, W. Bao, G. H. Zhang, F. Q. Huang, Q. Z. Huang, X. H. Chen, *Nature Materials* **2015**, 14, 325-329.
- [9] H. Sun, D. N. Woodruff, S. J. Cassidy, G. M. Allcroft, S. J. Sedlmaier, A. L. Thompson, P. A. Bingham, S. D. Forder, S. Cartenet, N. Mary, S. Ramos, F. R. Foronda, B. H. Williams, X. Li, S. J. Blundell, S. J. Clarke, *Inorganic Chemistry* **2015**, 54, 1958-1964.
- [10] F.-C. Hsu, J.-Y. Luo, K.-W. Yeh, T.-K. Chen, T.-W. Huang, P. M. Wu, Y.-C. Lee, Y.-L. Huang, Y.-Y. Chu, D.-C. Yan, M.-K. Wu, *Proceedings of the National Academy of Sciences* **2008**, 105, 14262-14264.
- [11] M. Burrard-Lucas, D. G. Free, S. J. Sedlmaier, J. D. Wright, S. J. Cassidy, Y. Hara, A. J. Corkett, T. Lancaster, P. J. Baker, S. J. Blundell, S. J. Clarke, *Nature Materials* **2013**, 12, 15-19.

-
- [12] A. Krzton-Maziopa, E. V. Pomjakushina, V. Y. Pomjakushin, F. v. Rohr, A. Schilling, K. Conder, *Journal of Physics: Condensed Matter* **2012**, 24, 382202.
- [13] Y. Mizuguchi, F. Tomioka, S. Tsuda, T. Yamaguchi, Y. Takano, *Journal of the Physical Society of Japan* **2009**, 78, 074712.
- [14] S. Medvedev, T. M. McQueen, I. A. Troyan, T. Palasyuk, M. I. Erements, R. J. Cava, S. Naghavi, F. Casper, V. Ksenofontov, G. Wortmann, C. Felser, *Nature Materials* **2009**, 8, 630-633.
- [15] H. Lueken, *Magnetochemie: Eine Einführung in Theorie und Anwendung*, Teubner, Stuttgart, **1999**.

4.6 Effect of cobalt substitution in the ferromagnetic superconductor $[(\text{Li}_{0.8}\text{Fe}_{0.2})\text{OH}]\text{FeSe}$

Ursula Pachmayr, Sirko Kamusella, Hans-Henning Klauss, and Dirk Johrendt



parts of this chapter are published in:

Zeitschrift für anorganische und allgemeine Chemie **2016**, 642, 989-996.

Copyright 2016, Wiley-VCH Verlag GmbH & Co. KGaA, Weinheim.

Abstract

The ferromagnetic superconductor $[(\text{Li}_{0.8}\text{Fe}_{0.2})\text{OH}]\text{FeSe}$ ($T_c \approx 43 \text{ K}$, $T_c \approx 10 \text{ K}$) provides a rare opportunity to further investigate the unusual coexistence of superconductivity and ferromagnetism.^[1] A recent density functional study predicts a positive effect on superconductivity for a substitution of iron by cobalt in the hydroxide layer, i.e. the hypothetical $[(\text{Li}_{0.8}\text{Co}_{0.2})\text{OH}]\text{FeSe}$.^[2] Two samples with the nominal composition $[(\text{Li}_{0.8}\text{Co}_{0.2})\text{OH}]\text{FeSe}$ respectively $[(\text{Li}_{0.8}\text{Co}_{0.3})\text{OH}]\text{FeSe}$ were prepared by hydrothermal synthesis. EDX measurements confirmed 0.24(5) and 0.34(4) cobalt per formula unit as expected, but no superconductivity emerged. ^{57}Fe -Mössbauer spectroscopy identified a third signal beside two main iron sites, which indicates that the iron environment in the FeSe layer is slightly disturbed. Thus cobalt has been incorporated in the hydroxide and in the FeSe-layers. The latter probably suppresses superconductivity similar to $\text{Fe}_{1-x}\text{Co}_x\text{Se}$.^[3]

4.6.1 Introduction

Doping or substitution is a popular method to pointedly modify structural or physical characteristics of solids. In the research of superconductivity for example, indications of the critical parameters for the emergence of superconductivity can be worked out. In the precedent chapter, the substitution of Se by S in the ferromagnetic superconductor $[(\text{Li}_{0.8}\text{Fe}_{0.2})\text{OH}]\text{FeSe}$ showed that S doping continuously decreases the superconducting transition temperature through chemical pressure. In contrast, S doping has no impact on the ferromagnetic ordering in the $(\text{Li}_{0.8}\text{Fe}_{0.2})\text{OH}$ layers. To further investigate the coexistence of ferromagnetism and superconductivity in $[(\text{Li}_{0.8}\text{Fe}_{0.2})\text{OH}]\text{FeSe}$ the magnetically ordered Fe in the hydroxide layer could be replaced by other transition metals like Co for example. Indeed, a recent density functional study predicts that a substitution of iron by cobalt in the hydroxide layer, i.e. the hypothetical $[(\text{Li}_{0.8}\text{Co}_{0.2})\text{OH}]\text{FeSe}$ will have a positive effect on superconductivity.^[2] The calculations of Chen *et al.* indicate that $[(\text{Li}_{0.8}\text{Co}_{0.2})\text{OH}]\text{FeSe}$ is stable with lattice constants similar to those of $[(\text{Li}_{0.8}\text{Fe}_{0.2})\text{OH}]\text{FeSe}$. It appears that the Co atoms do not contribute to the charge injection of FeSe as much as Fe but significantly facilitate more electron transfer from the O atoms in the spacer.^[2] This larger charge transfer might result in an increase of T_c . However, Co substitution in $\beta\text{-FeSe}$ is known and reduces T_c .^[3] Thus, experimental efforts are necessary to favor the incorporation of Co in the spacing layer over the one in the FeSe layer.

This chapter reports the experimental results of Co incorporation in the ferromagnetic superconductor $[(\text{Li}_{0.8}\text{Fe}_{0.2})\text{OH}]\text{FeSe}$.

4.6.2 Experimental details

Polycrystalline samples of cobalt substituted $[(\text{Li}_{0.8}\text{Fe}_{0.2})\text{OH}]\text{FeSe}$ were synthesized under hydrothermal conditions. To favor a specific substitution of Fe by Co in $[(\text{Li}_{0.8}\text{Fe}_{0.2})\text{OH}]\text{FeSe}$ in the hydroxide and not the selenide layer, pre-synthesized FeSe was used as a starting material. The synthesis of FeSe is described in chapter 3.2.2. The pre-synthesized FeSe (0.40 g, 7.2 mmol), additional iron metal (0.050 g, 0.90 mmol), cobalt metal (0.032 g, 0.54 mmol and 0.050 g, 0.85 mmol respectively), and $\text{LiOH}\cdot\text{H}_2\text{O}$ (3 g, 0.1 mmol) were mixed with distilled water, sealed in a teflon-lined steel autoclave and heated at 155 °C for 11 days. The addition of iron metal yields an improvement of sample crystallinity and was employed to prevent the emergence of Fe vacancies in the iron-selenide layer. The obtained black precipitates were washed with distilled water and ethanol, dried at room temperature under dynamic vacuum and stored at -25 °C under argon atmosphere.

Another hydrothermal synthesis strategy where large crystals of $[(\text{Li}_{0.8}\text{Fe}_{0.2})\text{OH}]\text{FeSe}$ (see chapter 4.4) were used as matrix crystals wasn't successful.

4.6.3 Results and discussion

Rietveld-refinement of the X-ray powder pattern (Fig. 1) applying the structure model of $[(\text{Li}_{0.8}\text{Fe}_{0.2})\text{OH}]\text{FeSe}$ shows that the sample was obtained phase pure within the experimental limits ($\sim 1\%$ of a crystalline phase). SEM-EDX measurements confirmed 0.24(5) and 0.34(4) Co per formula unit $[(\text{Li}_{0.8}\text{Fe}_{0.2})\text{OH}]\text{FeSe}$ for the two weighed portions of Co, respectively. However, the position of the incorporated Co cannot be clarified from conventional X-ray diffraction analysis.

As the physical and structural properties of the both samples with different amount of Co are analogously, solely the sample with 0.3 Co per formula unit $[(\text{Li}_{0.8}\text{Fe}_{0.2})\text{OH}]\text{FeSe}$, will be discussed. In comparison to unsubstituted $[(\text{Li}_{0.8}\text{Fe}_{0.2})\text{OH}]\text{FeSe}$ ($a = 380.4(1)$ pm, $c = 922.1(1)$ pm, $c/a = 2.42$), the unit cell is slightly elongated along the c axis ($a = 376.7(1)$ pm, $c = 931.8(1)$ pm, $c/a = 2.47$).

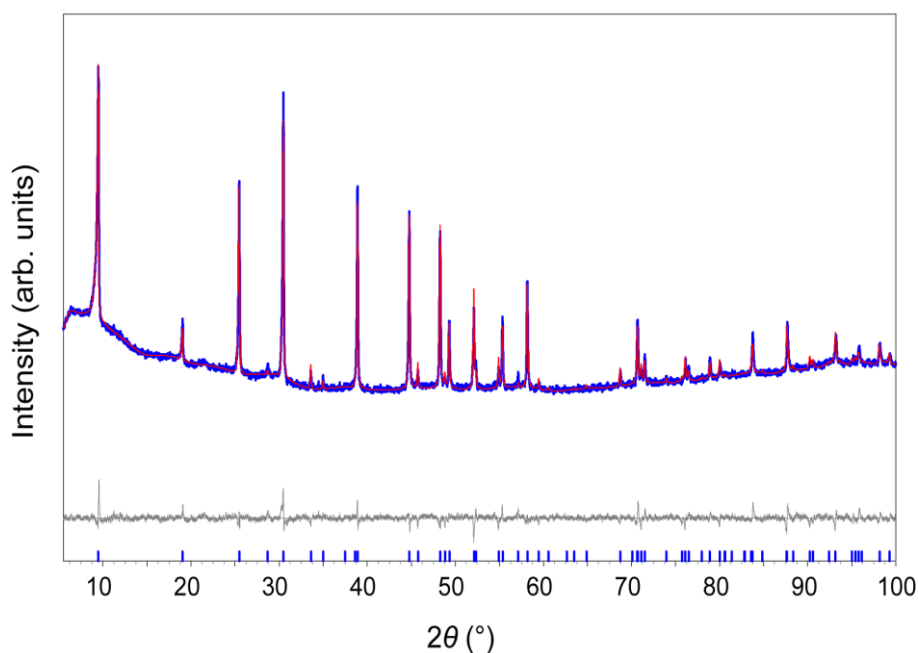


Fig. 1: X-ray powder pattern (blue) with Rietveld-fit (red) and difference curve (gray) for $[(\text{Li}_{0.8}\text{Fe}_{0.2})\text{OH}]\text{FeSe}$ substituted with 0.3 Co.

^{57}Fe -Mössbauer spectroscopy was performed to clarify the position of the incorporated Co. The spectrum (Fig. 2) shows two main Fe sites, one in the selenide (blue) and one in the hydroxide (magenta) layer.

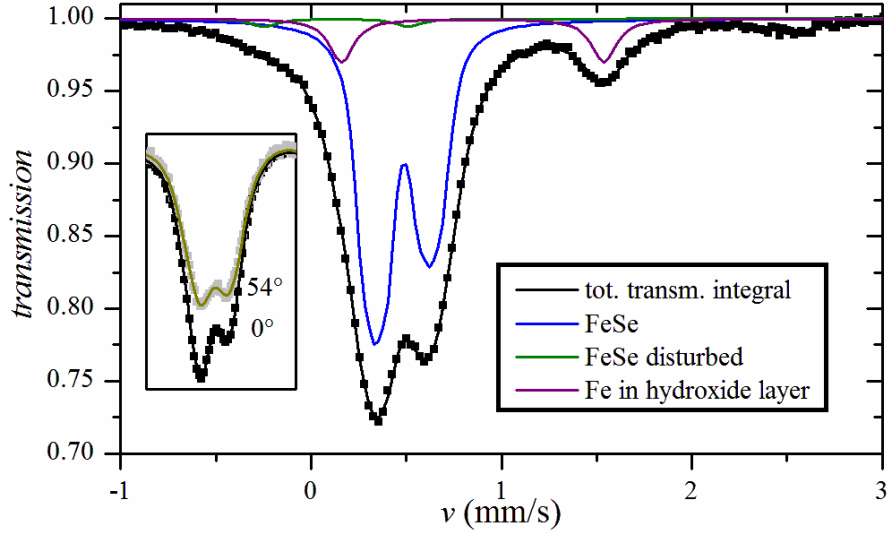


Fig. 2: ^{57}Fe -Mössbauer spectrum at 20 K detects two main iron sites and indicates that the FeSe layer is disturbed by cobalt. Inset: the anisotropy of the spectrum results from texture.

The amount of Fe in the hydroxide layer can be estimated to about 12(5) %. The sample was additionally rotated by 54° to show that the anisotropy of the spectrum results from texture (inset). A third doublet (green) indicates that the iron environment in the FeSe layer is slightly disturbed. This can be explained either by ‘vacant neighbor’ sites or the insertion of Co in the FeSe layer. The doublet shows an enhanced negative isomer shift which indicates that Co has been incorporated in the FeSe layer. Thus, together with the results from SEM-EDX measurement it can be concluded that Co has been incorporated in the hydroxide as well as in the FeSe-layer.

Apart from that the linewidth of the spectrum, especially that of the disturbed FeSe site is remarkably small. In contrast, the linewidth of unsubstituted $[(\text{Li}_{0.8}\text{Fe}_{0.2})\text{OH}]\text{FeSe}$ is larger, which might indicate that Co has a stabilizing effect on the structure.

Magnetic susceptibility and isothermal magnetization measurements are depicted in Fig. 3. The susceptibility is throughout positive revealing that superconductivity is completely suppressed by Co substitution, whereas a different signal in zfc and fc mode is observed below $T_c \approx 10$ K. This splitting is typical for a ferromagnetic ordering analogously to the results of $[(\text{Li}_{0.8}\text{Fe}_{0.2})\text{OH}]\text{FeS}$.^[4] Isothermal magnetization measurements confirm this

ferromagnetic ordering. The magnetization at 300 K is a straight line consistent with paramagnetism. The measurement at 1.8 K shows significantly larger values of μ and a very narrow hysteresis which indicates soft ferromagnetism.

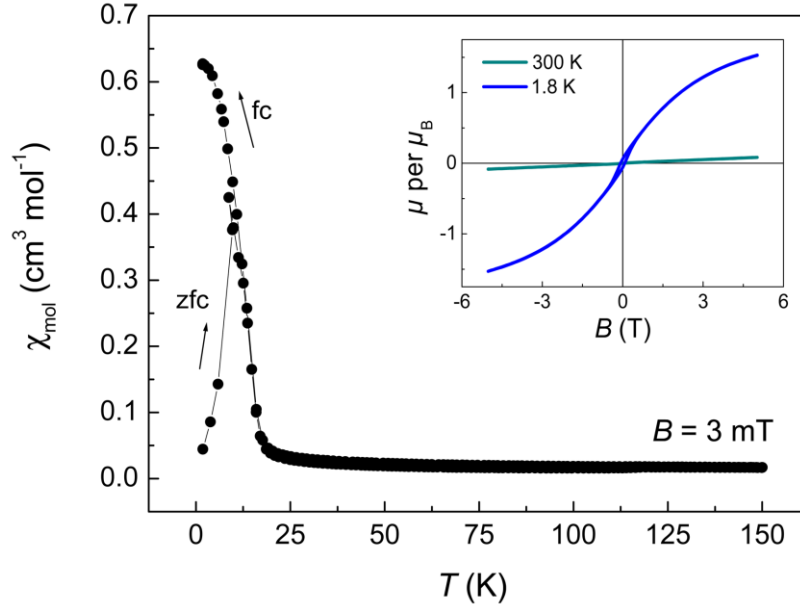


Fig. 3: Magnetic susceptibility of cobalt substituted $[(\text{Li}_{0.8}\text{Fe}_{0.2})\text{OH}]\text{FeSe}$ at $B = 3$ mT. Inset: isothermal magnetization at 1.8 K (dark cyan) and 300 K (blue).

As shown above, Co is incorporated in the hydroxide as well as the FeSe-layer. The latter probably suppresses superconductivity similar to $\text{Fe}_{1-x}\text{Co}_x\text{Se}$.^[3, 5] Perez *et al.* found that the incorporation of Co in FeSe injects free electrons into the system. The addition of these extra electrons along with the increase of the nuclear charge induces transitions in the electronic correlation strength and the spin state of the system, which in turn destroys the superconducting state.^[5] For $[(\text{Li}_{0.8}\text{Fe}_{0.2})\text{OH}]\text{FeSe}$ a similar scenario seems probable. The introduction of Co atoms in the FeSe layer might influence the electronic properties in a similar way and suppresses superconductivity.

4.6.4 Conclusion

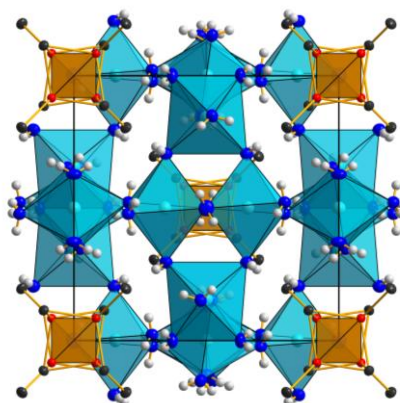
Magnetic susceptibility measurements show that superconductivity in $[(\text{Li}_{0.8}\text{Fe}_{0.2})\text{OH}]\text{FeSe}$ is suppressed by Co substitution whereas the ferromagnetic ordering below $T_c = 10$ K persists. Despite a directed synthesis strategy in which pre-synthesized β -FeSe was used as starting material, Co is incorporated in both, the hydroxide and the selenide layer. The latter probably suppresses superconductivity similar to $\text{Fe}_{1-x}\text{Co}_x\text{Se}$.

4.6.5 References

- [1] U. Pachmayr, F. Nitsche, H. Luetkens, S. Kamusella, F. Brückner, R. Sarkar, H.-H. Klauss, D. Johrendt, *Angewandte Chemie International Edition* **2015**, *54*, 293-297.
- [2] W. Chen, C. Zeng, E. Kaxiras, Z. Zhang, *Physical Review B* **2016**, *93*, 064517.
- [3] Y. Mizuguchi, F. Tomioka, S. Tsuda, T. Yamaguchi, Y. Takano, *Journal of the Physical Society of Japan* **2009**, *78*, 074712.
- [4] U. Pachmayr, D. Johrendt, *Chemical Communications* **2015**, *51*, 4689-4692.
- [5] I. Perez, J. A. McLeod, R. J. Green, R. Escamilla, V. Ortiz, A. Moewes, *Physical Review B* **2014**, *90*, 014510.

5 Hydrothermal synthesis of $\text{Na}_6(\text{H}_2\text{O})_{18}\text{Fe}_4\text{Se}_8$ and $\text{A}_2\text{Fe}_4\text{Se}_6$ ($\text{A} = \text{K}, \text{Rb}, \text{Cs}$)

Ursula Pachmayr, Stefan Datz, Sirko Kamusella, Hans-Henning Klauss, and Dirk Johrendt



parts of this chapter are in preparation for publication

5.1 Introduction

In the two precedent chapters, the effect of substitution in the hydroxide as well as the selenide layer of the ferromagnetic superconductor $[(\text{Li}_{0.8}\text{Fe}_{0.2})\text{OH}]\text{FeSe}$ was investigated. Continuing, one could try to replace the whole interlayer $(\text{Li}_{0.8}\text{Fe}_{0.2})\text{OH}$ by other metal hydroxide or metal oxide layers in order to further examine the properties of these layered iron selenide compounds. The replacement of the LiOH based layer by other alkaline metal hydroxide layers through simple variation of the educt AOH (A is alkaline metal) is one obvious possibility and subject of this chapter.

The obtained compounds consist of edge-sharing FeSe_4 tetrahedra as well, however they strongly differ from $[(\text{Li}_{0.8}\text{Fe}_{0.2})\text{OH}]\text{FeSe}$. Beside $\text{A}_2\text{Fe}_4\text{Se}_6$ ($\text{A} = \text{K}, \text{Rb}, \text{Cs}$) which is known in literature, a new compound $\text{Na}_6(\text{H}_2\text{O})_{18}\text{Fe}_4\text{Se}_8$ is prepared where the dimensionality of the FeSe fragment from two-dimensional FeSe layers to one-dimensional $[\text{FeSe}_2]^-$ chains^[1] is further reduced to zero-dimensional $[\text{Fe}_4\text{Se}_8]^{6-}$ clusters. The $[\text{Fe}_4\text{Se}_8]^{6-}$ clusters resemble well known protein-bound iron-sulfur clusters in the active sites of ferredoxins $[\text{Fe}_4(\mu_3\text{-S})_4]^{n+}(\text{S}_{\text{cys}})_4$ ($n = 1, 2$) where the sulfur atoms of cysteinate take the positions of the

four terminal sulfido ligands.^[2, 3] The metalloproteins are involved in biological oxidoreductive functions and play an important role for living creatures. To gain more detailed geometric and electronic structural data and an insight which properties are intrinsic to the iron-sulfur clusters themselves, synthetic model compounds that use organic thiolates in place of cysteine ligands from the protein were synthesized.^[4] Recently, Schwarz *et al.* reported the first $[\text{Fe}_4\text{S}_8]^{n-}$ ($n = 7$) cluster with pure S^{2-} ligands in $\text{Cs}_7[\text{Fe}_4\text{S}_8]$ and shortly afterwards the analogous selenide anion $[\text{Fe}_4\text{Se}_8]^{6-}$ was observed in $\text{K}_6[\text{Fe}_4\text{Se}_8]$.^[5, 6]

In contrast to these alkaline chalcogenido ferrates, the clusters in $\text{Na}_6(\text{H}_2\text{O})_{18}\text{Fe}_4\text{Se}_8$ are coordinated only via weak hydrogen bonds. This opens the opportunity that the isolated clusters might be easily dissolved in an appropriate solvent, which may facilitate further chemistry.

5.2 Experimental details

Polycrystalline samples were prepared under hydrothermal conditions. Iron metal (0.0851 g), Selenourea (0.50 g), and 3.0 g NaOH, KOH respectively RbOH·H₂O were mixed with distilled water (10 mL), sealed in a teflon-lined steel autoclave (50 mL) under argon atmosphere and heated at 155 °C for 7 days. 10 mL (17.2 g) of 50 wt% aqueous solution of CsOH was applied for the synthesis with Cs. The obtained black precipitates were collected by centrifugation and washed with distilled water and ethanol. The samples were dried at room temperature under dynamic vacuum and stored in a purified argon atmosphere glove box.

5.3 Results and discussion

$\text{A} = \text{K}, \text{Rb}, \text{Cs}$

When LiOH is replaced by KOH, RbOH or CsOH in the hydrothermal synthesis of $[(\text{Li}_{0.8}\text{Fe}_{0.2})\text{OH}]\text{FeSe}$, the alkaline metal iron selenides $\text{A}_2\text{Fe}_4\text{Se}_6$ ($\text{A} = \text{K}, \text{Rb}, \text{Cs}$) are formed. These compounds are known in literature and consist of double chains of $[\text{Fe}_2\text{Se}_3]^{1-}$ formed by edge-sharing FeSe_4 tetrahedra. The $[\text{Fe}_2\text{Se}_3]^{1-}$ chains extend along the *c* axis and show a stripelike magnetic order, whereby the channels are occupied by alkaline metal cations as shown in Fig. 1.^[7, 8] Here, the compounds are synthesized via hydrothermal method for the first time. The structural characterization via X-ray powder diffraction revealed phase pure samples of $\text{A}_2\text{Fe}_4\text{Se}_6$ ($\text{A} = \text{K}, \text{Rb}, \text{Cs}$). This extends the spectrum of compounds accessible via

hydrothermal synthesis and illustrates the potential of this synthesis strategy with regard to iron-chalcogenides.

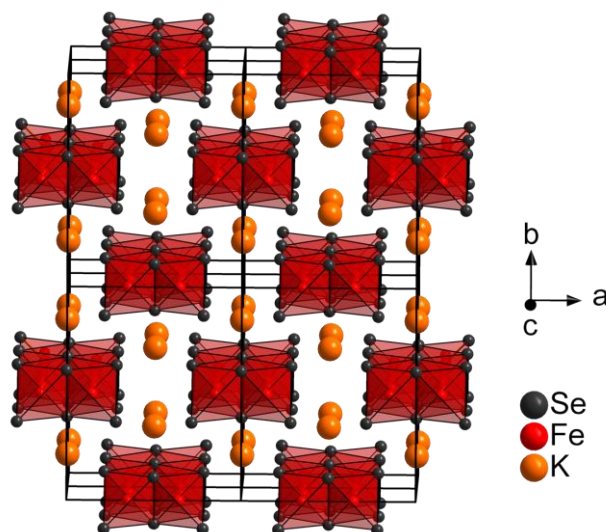


Fig. 1: Crystal structure of $\text{K}_2\text{Fe}_4\text{Se}_6$.

$\text{A} = \text{Na}$

The replacement of LiOH by NaOH in the hydrothermal synthesis of $[(\text{Li}_{0.8}\text{Fe}_{0.2})\text{OH}]\text{FeSe}$ yielded the new compound $\text{Na}_6(\text{H}_2\text{O})_{18}\text{Fe}_4\text{Se}_8$. The samples were characterized by single crystal as well as powder X-ray diffraction. The composition was confirmed by SEM-EDX ($\text{Na} : \text{Fe} : \text{Se} = 1.6(2) : 1 : 1.9(2)$), ICP-AES ($\text{Na} : \text{Fe} : \text{Se} = 1.4(1) : 1 : 2.0(1)$) and elementary analysis (2.6(1) wt% H).

Rietveld refinement of the X-ray powder diffractogram of $\text{Na}_6(\text{H}_2\text{O})_{18}\text{Fe}_4\text{Se}_8$ (Fig. 2) shows that the compound was obtained in a phase pure sample. For the refinement the structural data from single crystal X-ray analysis (Tab. 1) were applied.

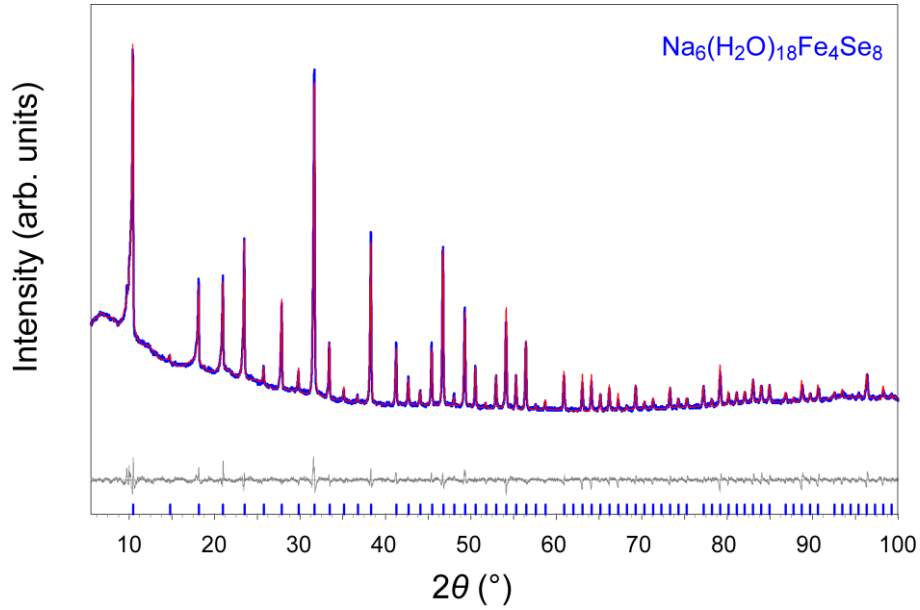


Fig. 2: X-ray powder pattern (blue) with Rietveld-fit (red) and difference curve (gray) of $\text{Na}_6(\text{H}_2\text{O})_{18}\text{Fe}_4\text{Se}_8$.

Tab. 1: Crystallographic data of $\text{Na}_6(\text{H}_2\text{O})_{18}\text{Fe}_4\text{Se}_8$ obtained by single crystal X-ray analysis.

| $\text{Na}_6(\text{H}_2\text{O})_{18}\text{Fe}_4\text{Se}_8$ | | | | | |
|------------------------------------------------------------------------------------|--------------------------------------------------------------|------------|-------------|------------|-----------------|
| Formula | $\text{Na}_6(\text{H}_2\text{O})_{18}\text{Fe}_4\text{Se}_8$ | | | | |
| Formula weight /g mol ⁻¹ | 329.3 | | | | |
| Crystal system | Cubic | | | | |
| Space group | $I23$ (No. 197) | | | | |
| a /pm | 119.707(2) | | | | |
| V /nm ³ | 1.71537(5) | | | | |
| Z | 8 | | | | |
| d_{calc} /gcm ³ | 2.55 | | | | |
| μ (Mo-K α) /mm ⁻¹ | 10.277 | | | | |
| Temperature /K | 293 | | | | |
| Radiation /pm | Mo-K α λ = 71.073 | | | | |
| θ range /deg. | 2.41–34.93 | | | | |
| hkl range | −18 → +19; −19 → +19; −14 → +19 | | | | |
| Tot., uniq. data | 18690, 1258 | | | | |
| $R_{\text{int}}, R_{\sigma}$ | 0.0418, 0.0236 | | | | |
| $N_{\text{Ref}}, N_{\text{Par}}$ | 1258, 38 | | | | |
| R_1, wR_2, S | 0.0271, 0.0410, 1.05 | | | | |
| $\Delta\rho_{\text{min}}, \Delta\rho_{\text{max}}$ /e [−] Å ^{−3} | −0.36, +0.32 | | | | |
| Atomic positions and displacement parameters | | | | | |
| Atom | Wyck. | x | y | z | U_{eq} |
| Se1 | 8c | 0.19636(1) | 0.19636(1) | 0.19636(1) | 0.02751(5) |
| Se2 | 8c | 0.11400(1) | −0.11400(1) | 0.11400(1) | 0.02276(4) |
| Fe | 8c | 0.08383(2) | 0.08383(2) | 0.08383(2) | 0.01825(5) |
| Na | 12e | 1/2 | 0.1565(1) | 0 | 0.0375(4) |
| O1 | 24f | 0.6517(1) | 0.2953(1) | 0.0218(1) | 0.0358(5) |

| | | | | | |
|----|-------------|----------|----------|-----------|-----------|
| O2 | 12 <i>d</i> | 1/2 | 1/2 | 0.1278(2) | 0.0456(8) |
| H1 | 24 <i>f</i> | 0.672(2) | 0.283(2) | 0.086(2) | 0.02 |
| H2 | 24 <i>f</i> | 0.690(2) | 0.269(2) | -0.020(2) | 0.02 |
| H3 | 24 <i>f</i> | 0.475(2) | 0.552(2) | 0.158(2) | 0.02 |

Selected bond lengths (/pm) and angles (/deg)

| | | | |
|--------|--------------------|------------|-------------------------------------------|
| Fe–Fe | 283.83(3) | | |
| Fe–Se1 | 233.31(3) | Se1–Fe–Se2 | 113.09(1) |
| Fe–Se2 | 242.26(3) | Se2–Fe–Se2 | 105.62(1) |
| Na–O1 | 246.5(1), 247.6(1) | O1–Na–O1 | 177.3(1), 95.68(5), 92.46(5), 89.35(5) |
| Na–O2 | 241.9(1) | O2–Na–O2 | 78.46(1) |
| | | O1–Na–O2 | 169.7(1), 93.21(3), 92.78(3), 85.12(3) |
| O1–H1 | 82.2(1) | H2–O1–H1 | 112(1) |
| O1–H2 | 74.9(1) | | |
| O2–H3 | 78.2(1) | H3–O2–H3 | 125(1) |
| Se1–H1 | 263(1) | Se1–H1–O1 | 161(1) |
| Se1–H2 | 266(1) | Se1–H2–O1 | 168(1) |
| Se2–H1 | 328(1) | Se2–H1–O1 | 116(1) |
| Se2–H3 | 328(1) | Se2–H3–O2 | 112(1) |
| Se1–O1 | 339.6(1) | | |
| Se1–O2 | 393.5(1) | | |
| Se2–O1 | 371.4(1) | | |
| Se2–O2 | 364.4(1) | | |

The crystal structure of $\text{Na}_6(\text{H}_2\text{O})_{18}\text{Fe}_4\text{Se}_8$ consists of $[\text{Fe}_4\text{Se}_8]^{6-}$ ‘stella quadrangula’ clusters which are embedded in a $[\text{Na}_6(\text{H}_2\text{O})_{18}]^{6+}$ network (Fig. 3). A similar structure is realized in the KSbO_3 and $\text{Cs}_{18}\text{Tl}_8\text{O}_6$ type structures where homoatomic clusters of K_8 respectively Tl_8 are embedded in a three-dimensional network of SbO_6 respectively OCs_6 octahedra.^[9, 10]

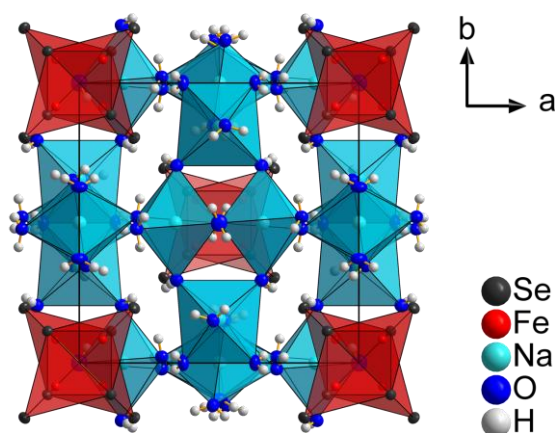


Fig. 3: Crystal structure of $\text{Na}_6(\text{H}_2\text{O})_{18}\text{Fe}_4\text{Se}_8$.

The $[\text{Na}_6(\text{H}_2\text{O})_{18}]^{6+}$ network is built of slightly distorted $[\text{Na}(\text{H}_2\text{O})_6]^+$ octahedra. Two edge-sharing octahedra are connected via common corners to two further octahedra, building a tetramer (Fig. 4A). The latter is assembled to form a hollow, cubic like network.

Analogous edge-sharing $[\text{Na}(\text{H}_2\text{O})_6]^+$ octahedra forming $[\text{Na}(\text{H}_2\text{O})_5]^{2+}$ dimers are known from alkaline metal salts. $\text{Na}_2\text{CO}_3 \cdot 10 \text{H}_2\text{O}$ for example can be considered as distorted NaCl-type structure composed of $[\text{Na}(\text{H}_2\text{O})_5]^{2+}$ and CO_3^{2-} ions.^[11] The sodium-water distances are comparable in both structures (241.9(1)–247.6(1) pm in $\text{Na}_6(\text{H}_2\text{O})_{18}\text{Fe}_4\text{Se}_8$, 231–251 pm in $\text{Na}_2\text{CO}_3 \cdot 10 \text{H}_2\text{O}$).

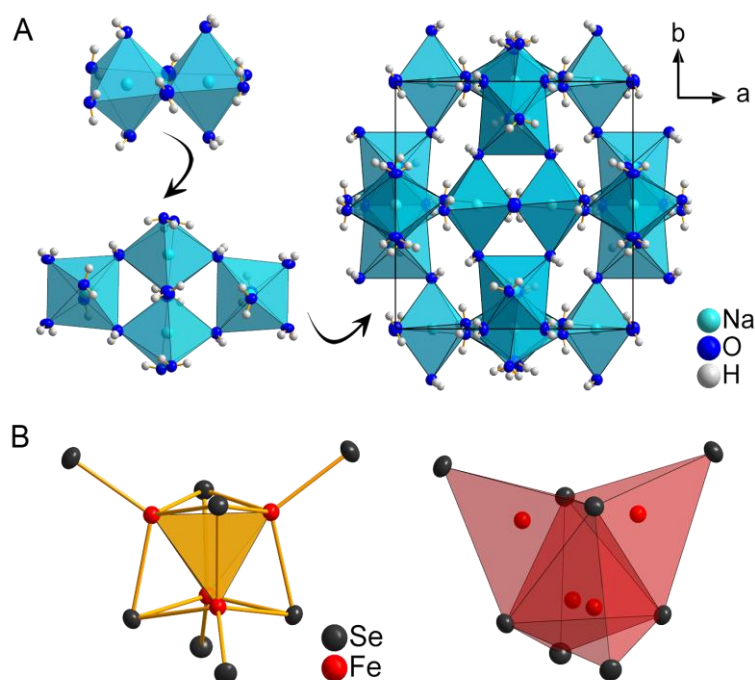


Fig. 4: Building blocks of $\text{Na}_6(\text{H}_2\text{O})_{18}\text{Fe}_4\text{Se}_8$: assemblage of $[\text{Na}(\text{H}_2\text{O})_6]^+$ octahedra to a three-dimensional network (A); ‘stella quadrangula’ $[\text{Fe}_4\text{Se}_8]^{6-}$ cluster (B).

The second structural unit, the $[\text{Fe}_4\text{Se}_8]^{6-}$ clusters (Fig. 4B), are located in the cavities of the $[\text{Na}_6(\text{H}_2\text{O})_{18}]^{6+}$ network. Four slightly distorted FeSe_4 tetrahedra are connected via three edges respectively to form a tetrahedral ‘stella quadrangula’ cluster with T_d symmetry and a $[\text{Fe}_4(\mu_3\text{-Se})_4]^{2+}$ heterocubane core. The terminal selenium atoms are H-acceptors in 2×3 weak $\text{Se} \cdots \text{H}-\text{O}$ hydrogen bonds ($d(\text{Se1}-\text{H1}) = 263(1)$ pm, $d(\text{Se1}-\text{H2}) = 266(1)$ pm) of H_2O ligands in the $[\text{Na}_6(\text{H}_2\text{O})_{18}]^{6+}$ network (see Fig. 5). For the μ_3 selenium atoms, a similar hydrogen bonding of 6 very weak $\text{Se} \cdots \text{H}-\text{O}$ bonds is observed with a bond length of $d(\text{Se2}-\text{H1}) = d(\text{Se2}-\text{H3}) = 328(1)$ pm.

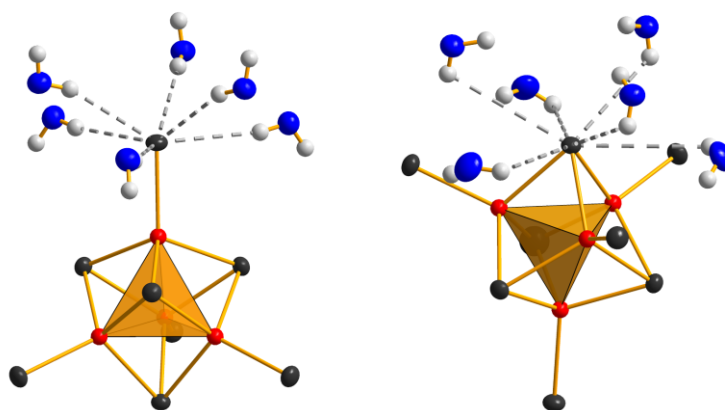


Fig. 5: Coordination of the terminal Se1 (left) and the μ_3 -Se2 (right) atoms via hydrogen bonds.

Hence, the clusters in $\text{Na}_6(\text{H}_2\text{O})_{18}\text{Fe}_4\text{Se}_8$ are coordinated only by hydrogen bonds to the H_2O ligands of the $[\text{Na}_6(\text{H}_2\text{O})_{18}]^{6+}$ network. This opens the opportunity that the isolated clusters might be easily obtained by solving the compound in an appropriate solvent.

Hydrogen bonding systems of type $\text{Se} \cdots \text{H}-\text{O}$ are exceptional but known in literature. Examples are $\text{Na}_3\text{AsSe}_4 \cdot 9 \text{H}_2\text{O}$, $\text{Na}_3\text{AsO}_3\text{Se} \cdot 12 \text{H}_2\text{O}$, $\text{Na}_4\text{GeSe}_4 \cdot 14 \text{H}_2\text{O}$, $\text{Na}_4\text{SnSe}_4 \cdot 16 \text{H}_2\text{O}$, $\text{Na}_4\text{Ge}_2\text{Se}_6 \cdot 16 \text{H}_2\text{O}$ and $\text{Na}_4\text{Sn}_2\text{Se}_6 \cdot 13 \text{H}_2\text{O}$.^[12–16] The $\text{Se} \cdots \text{H}$ distances of the terminal selenium (263(1)–266(1) pm) as well as the $\text{Se} \cdots \text{O}$ distances for both selenium atoms (339.6(1)–393.5(1) pm) in $\text{Na}_6(\text{H}_2\text{O})_{18}\text{Fe}_4\text{Se}_8$ are comparable to those found in the mentioned examples. The $\text{Se} \cdots \text{H}$ distances of the μ_3 -Se amounting to 328(1) pm should be considered as an edge case of weak hydrogen bonding.

The $[\text{Fe}_4\text{Se}_8]^{6-}$ clusters resemble well known protein-bound iron-sulfur clusters in the active site of ferredoxins $[\text{Fe}_4(\mu_3\text{-S})_4]^{n+}(\text{S}_{\text{cys}})_4$ ($n = 1, 2$) and are isotypic to the one in $\text{K}_6[\text{Fe}_4\text{Se}_8]$.^[2, 6] Iron shows an average oxidation state of 2.5+ thus a 1:1 proportion of $\text{Fe}^{2+}:\text{Fe}^{3+}$. This intermediate oxidation state is well-known from protein-bound $[\text{Fe}_4\text{S}_4]^{2+}$ clusters. The latter feature two parallel Fe–Fe pair spin vectors and four antiparallel, and correspondingly two delocalized $\text{Fe}^{2.5+}-\text{Fe}^{2.5+}$ pairs, each associated with a parallel spin Fe–Fe pair.^[17] The antiparallel coupling of the delocalized $\text{Fe}^{2.5+}-\text{Fe}^{2.5+}$ pairs yields a total spin $S_{\text{tot}} = 0$. An analogous magnetic ordering in $\text{Na}_6(\text{H}_2\text{O})_{18}\text{Fe}_4\text{Se}_8$ is suggested by Mössbauer and magnetic measurements.

Mössbauer measurements show a doublet with isomer shift $\delta = 0.37$ mm/s and a quadrupol splitting of 0.59 mm/s (Fig. 6). The doublet arises from one iron site with oxidation state between Fe^{2+} and Fe^{3+} , which confirms the model of delocalized $\text{Fe}^{2.5+}$ – $\text{Fe}^{2.5+}$ pairs.

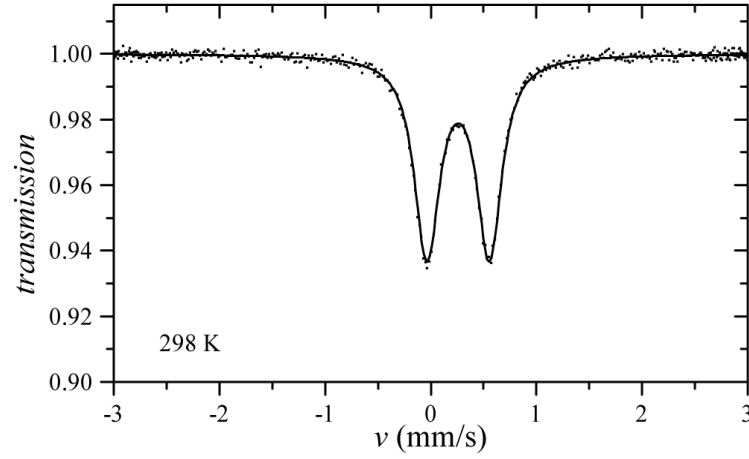


Fig. 6: Mössbauer spectrum of $\text{Na}_6(\text{H}_2\text{O})_{18}\text{Fe}_4\text{Se}_8$ shows one iron site between Fe^{2+} and Fe^{3+} .

Magnetic measurements show small values of χ_{mol} compared to those expected for paramagnetic $\text{Fe}^{2+}/\text{Fe}^{3+}$ (Fig. 7).

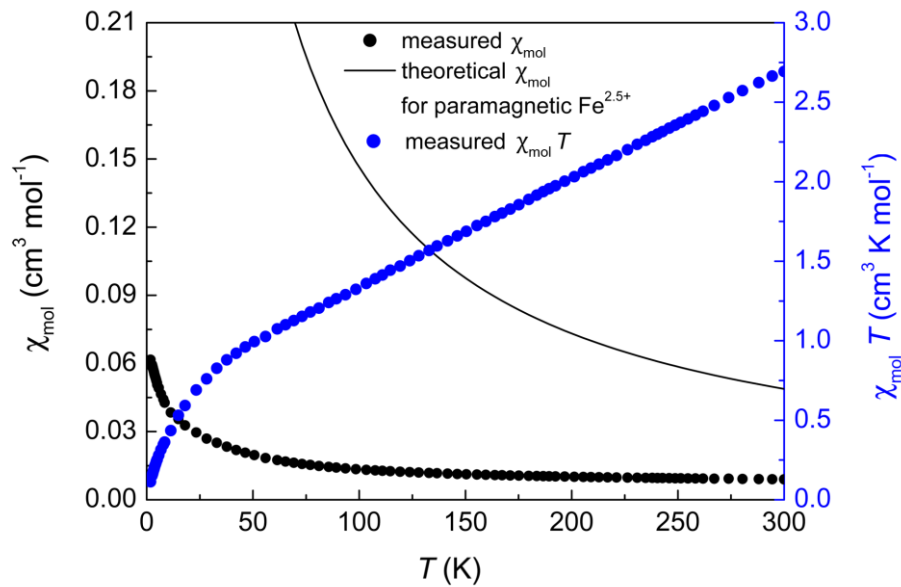


Fig. 7: Susceptibility of $\text{Na}_6(\text{H}_2\text{O})_{18}\text{Fe}_4\text{Se}_8$ at 2 T; the measured χ_{mol} (black dots) is distinctively smaller than the theoretically expected χ_{mol} for paramagnetic $\text{Fe}^{2+}/\text{Fe}^{3+}$ (black line); the decrease of $\chi_{\text{mol}} T$ (blue dots) with decreasing temperature indicates antiparallel ordering of the spins.

Analogously to the above mentioned protein-bound $[\text{Fe}_4\text{S}_4]^{2+}$ clusters we assume antiparallel ordering of the intervalent $\text{Fe}^{2.5+}-\text{Fe}^{2.5+}$ pairs already at room temperature. This is supported by the decrease of $\chi_{\text{mol}} T$ with decreasing temperature.

The Raman spectrum of $\text{Na}_6(\text{H}_2\text{O})_{18}\text{Fe}_4\text{Se}_8$ is shown in Fig. 8. It can be interpreted by comparing with Raman spectra from analogous protein bound iron-sulfur clusters where none, partial or total selenium substitutions were carried out.^[18, 19] The strong 233 cm^{-1} band can be attributed to the totally symmetric cluster breathing mode, the $\text{A}_1 \nu[\text{Fe}-\text{Se}^{\text{b}}]$ (b = bridging) stretch. The 443 cm^{-1} and 460 cm^{-1} bands presumably originate from $\nu[\text{Fe}-\text{Se}^{\text{t}}]$ (t = terminal) stretching modes. In contrast to the $\nu[\text{Fe}-\text{S}(\text{cysteine})]$ stretching modes at 360 cm^{-1} and 374 cm^{-1} in the $[\text{Fe}_4\text{Se}_4]^{n+}(\text{S}_{\text{cys}})_4$ ferredoxins from *Clostridium pasteurianum*, the modes are shifted to higher wavenumbers which can be explained by the coordination of Se^{t} via weak hydrogen bonds in contrast to the covalent bond of S^{t} in cysteine.

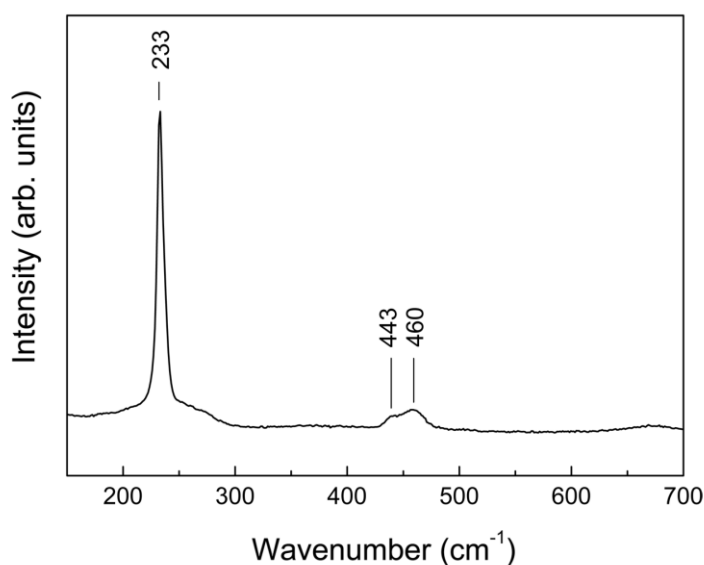


Fig. 8: Raman spectrum of $\text{Na}_6(\text{H}_2\text{O})_{18}\text{Fe}_4\text{Se}_8$.

5.4 Conclusion

By replacement of the alkaline metal in the hydrothermal synthesis of $[(\text{Li}_{0.8}\text{Fe}_{0.2})\text{OH}]\text{FeSe}$, the literature known alkaline metal iron selenides $\text{A}_2\text{Fe}_4\text{Se}_6$ ($\text{A} = \text{K}, \text{Rb}, \text{Cs}$) were prepared via hydrothermal method for the first time. For Na, the new iron-chalcogenide $\text{Na}_6(\text{H}_2\text{O})_{18}\text{Fe}_4\text{Se}_8$ was obtained. It consists of $[\text{Fe}_4\text{Se}_8]^{6-}$ ‘stella quadrangula’ clusters of edge-

sharing FeSe_4 tetrahedra which are embedded in a three-dimensional $[\text{Na}_6(\text{H}_2\text{O})_{18}]^{6+}$ network. Mössbauer and magnetic measurements suggest that the magnetic ordering of the iron-selenide clusters is analogous to the one observed in protein-bound $[\text{Fe}_4\text{S}_4]^{2+}$ clusters. It seems that two intervalent $\text{Fe}^{2.5+}-\text{Fe}^{2.5+}$ pairs with parallel spin show antiparallel coupling. The clusters in $\text{Na}_6(\text{H}_2\text{O})_{18}\text{Fe}_4\text{Se}_8$ are coordinated only via hydrogen bonds to the H_2O ligands of the $[\text{Na}_6(\text{H}_2\text{O})_{18}]^{6+}$ network, thus the isolated clusters might be easily obtained by solving the compound in an appropriate solvent.

5.5 References

- [1] C. Pak, S. Kamali, J. Pham, K. Lee, J. T. Greenfield, K. Kovnir, *Journal of the American Chemical Society* **2013**, *135*, 19111-19114.
- [2] H. Beinert, R. H. Holm, E. Münck, *Science* **1997**, *277*, 653-659.
- [3] P. Venkateswara Rao, R. H. Holm, *Chemical Reviews* **2004**, *104*, 527-560.
- [4] J. Ibers, R. Holm, *Science* **1980**, *209*, 223-235.
- [5] M. Schwarz, C. Röhr, *Inorganic Chemistry* **2015**, *54*, 1038-1048.
- [6] P. Stüble, A. Berroth, C. Röhr, *Zeitschrift für Naturforschung B* **2016**, *71*, 485.
- [7] J. M. Caron, J. R. Neilson, D. C. Miller, K. Arpino, A. Llobet, T. M. McQueen, *Physical Review B* **2012**, *85*, 180405.
- [8] F. Du, K. Ohgushi, Y. Nambu, T. Kawakami, M. Avdeev, Y. Hirata, Y. Watanabe, T. J. Sato, Y. Ueda, *Physical Review B* **2012**, *85*, 214436.
- [9] U. Wedig, V. Saltykov, J. Nuss, M. Jansen, *Journal of the American Chemical Society* **2010**, *132*, 12458-12463.
- [10] P. Spiegelberg, *Arkiv för Kemi, Mineralogi och Geologi* **1940**, *A 14*, 1-2.
- [11] T. Taga, *Acta Crystallographica Section B* **1969**, *25*, 2656-2658.
- [12] B. Krebs, H.-U. Hürter, *Zeitschrift für anorganische und allgemeine Chemie* **1980**, *462*, 143-151.
- [13] B. Krebs, H. U. Hürter, J. Enax, R. Fröhlich, *Zeitschrift für anorganische und allgemeine Chemie* **1990**, *581*, 141-152.
- [14] B. Krebs, H. J. Jacobsen, *Zeitschrift für anorganische und allgemeine Chemie* **1976**, *421*, 97-104.
- [15] B. Krebs, H. Müller, *Zeitschrift für anorganische und allgemeine Chemie* **1983**, *496*, 47-57.
- [16] B. Krebs, H. Uhlen, *Zeitschrift für anorganische und allgemeine Chemie* **1987**, *549*, 35-45.

-
- [17] L. Noodleman, C. Y. Peng, D. A. Case, J. M. Mouesca, *Coordination Chemistry Reviews* **1995**, *144*, 199-244.
- [18] R. S. Czernuszewicz, K. A. Macor, M. K. Johnson, A. Gewirth, T. G. Spiro, *Journal of the American Chemical Society* **1987**, *109*, 7178-7187.
- [19] J. M. Moulis, J. Meyer, M. Lutz, *Biochemical Journal* **1984**, *219*, 829-832.

6 Summary

In this thesis a new approach for the synthesis of layered iron-chalcogenide superconductors via hydrothermal method was developed. Insights into the critical parameters for these syntheses were acquired and several iron-selenide and -sulfide based compounds were prepared. The obtained compounds were properly examined concerning their structural, magnetic and electrical properties. A broad range of analytical methods like laboratory and synchrotron XRD, EDX, susceptibility, resistivity, Mössbauer, μ SR, NMR, TEM and Raman measurements were applied. The combination of appropriate methods allowed a detailed analysis of the compounds.

Influence of synthesis parameters on the hydrothermal synthesis of FeSe

A hydrothermal synthesis of β -FeSe was successfully developed starting from elementary iron and selenium.

The reduction potential and pH value of the solutions as well as reaction time and temperature have influence on the success of the synthesis. The optimal concentration of KOH and the reducing agent NaBH_4 was determined to 0.45 mol/L and at least 0.20 mol/L, respectively. The optimal heating time and temperature were determined to 6 days and 170 °C for the present synthesis. Temperatures, heating times and concentrations of KOH which exceed these optimal values favor the formation of Fe_3O_4 whereas no adverse effect was observed for a larger concentration of NaBH_4 .

At optimized conditions FeSe was obtained with a yield of about 70 mol% and residuals of the educt Fe were the only impurity phase. The latter can be removed applying a magnetic field.

Structural transition and superconductivity in hydrothermally synthesized FeX (X = S, Se)

Hydrothermally prepared FeSe was carefully examined with regard to crystal structure as well as superconducting properties and compared to FeSe from conventional solid-state synthesis. Astonishingly, only traces of superconductivity were detected in the sample from hydrothermal synthesis, while bulk superconductivity occurred in conventionally prepared samples as expected. No differences in composition or structure were detected at room temperature, however a lower lattice symmetry where iron zigzag chains are formed

instead of iron stripes by short and large Fe–Fe distances was observed in the low-temperature structure of hydrothermally prepared FeSe.

Intriguingly, the respective sulfide FeS is bulk superconducting when synthesized via hydrothermal method and non-superconducting from solid-state methods. Contrary to FeSe, superconductivity in FeS emerges without structural transition in the tetragonal phase, which may indicate that the iron sulfide may rather be a conventional BCS-type superconductor and thus quite different from the selenide.

The solid-solution $\text{FeSe}_{1-x}\text{S}_x$ prepared via hydrothermal synthesis

The solid-solution $\text{FeSe}_{1-x}\text{S}_x$ was successfully prepared via hydrothermal synthesis for the whole substitution range in contrast to solid state reaction where a solubility limit is reported at $x = 0.3$. The partial substitution of Se by S does not lead to a re-emergence of bulk superconductivity, the latter being only observed in the pure sulfur compound. The absence of bulk superconductivity for the samples $\text{FeSe}_{1-x}\text{S}_x$ with $0 \leq x < 1$ might be attributable to slight differences in the detailed crystal structure, for example vacancies, distortions or interstitial atoms, too weak to be detected by the standard analysis methods.

A difference in the size of the crystallites of $\text{FeSe}_{1-x}\text{S}_x$ with $0 \leq x < 1$ versus $x = 1$ is observed as well. The particles of FeS are more than one magnitude larger than those of the rest of the solid-solution. These different sizes can be excluded as reason for the decisive reduction of the superconducting volume fraction as bulk samples were employed for the measurements. Examination of residual magnetic particles gave indication of different growth processes of non-superconducting and superconducting samples. While FeS seems to grow directly on the surface of the iron educt particles, a mechanism where most of the elementary iron dissolves first under oxidation seems more plausible for the rest of the solid-solution.

Coexistence of 3d-ferromagnetism and superconductivity in $[(\text{Li}_{0.8}\text{Fe}_{0.2})\text{OH}]\text{FeSe}$

$[(\text{Li}_{0.8}\text{Fe}_{0.2})\text{OH}]\text{FeSe}$ was synthesized under hydrothermal conditions and thoroughly examined concerning the structural, magnetic and electrical properties. The layered crystal structure consists of ferromagnetic ($T_c \approx 10$ K) $(\text{Li}_{0.8}\text{Fe}_{0.2})\text{OH}$ layers and superconducting ($T_c = 43$ K) FeSe layers each with *anti*-PbO-type structures. Formally, 0.2 electrons are transferred from the hydroxide to the selenide layer. This electron doping of the FeSe layer is most probably the main reason for the enormous increase of T_c in comparison to β -FeSe.

Superconductivity and ferromagnetism coexist in spatial separation of the respective layers. However, the internal dipole field of the ferromagnet acts on the superconductor, which suggests the existence of a special state of matter called a spontaneous vortex phase. Magnetic measurements, ^{57}Fe -Mössbauer spectroscopy, ^7Li -NMR, and μSR measurements consistently support this conclusion. This rare phenomenon was so far confined to *f*-shell magnetism, while in $[(\text{Li}_{0.8}\text{Fe}_{0.2})\text{OH}]\text{FeSe}$ superconductivity coexists with 3*d*-ferromagnetism for the first time, and at the highest temperatures to date. In contrast to the chemically inert *f*-shells, 3*d*-magnetism is much more susceptible to the chemical environment, which opens new avenues for chemical modifications that can now directly couple to the magnetic and superconducting properties, thus allowing broader studies of such coexistence phenomena.

Upper critical field in $[(\text{Li}_{0.8}\text{Fe}_{0.2})\text{OH}]\text{FeSe}$

The upper critical field of $[(\text{Li}_{0.8}\text{Fe}_{0.2})\text{OH}]\text{FeSe}$ was determined by temperature dependent resistivity measurements under various magnetic fields. Applying the Werthamer-Helfand-Hohenberg formula, the zero-temperature upper critical field was estimated to $H_{c2}(0) \approx 80$ T, roughly. As known in literature, evaluation of the data based on the Ginzburg-Landau equation results in a zero-temperature upper critical field that is about 20 % larger. Even if the values have to be seen as a rough estimation, the large magnitude of $H_{c2}(0)$ coincides with the dimension of $H_{c2}(0)$ for other iron based superconductors.

Investigations on the real structure of $[(\text{Li}_{0.8}\text{Fe}_{0.2})\text{OH}]\text{FeX}$ ($X = \text{Se}, \text{S}$)

Investigations on the real structure of $[(\text{Li}_{0.8}\text{Fe}_{0.2})\text{OH}]\text{FeX}$ ($X = \text{Se}, \text{S}$) were accomplished with regard to a so far unsettled, strongly anisotropic displacement ellipsoid in the magnetic $(\text{Li}_{0.8}\text{Fe}_{0.2})\text{OH}$ layer. Low temperature single crystal analysis precluded enhanced thermal motion as reason for the enlarged displacement ellipsoid. By application of transmission electron microscopy, a $\sqrt{2}a \times \sqrt{2}a$ superstructure analogous to the superconducting phase of $\text{K}_y\text{Fe}_{2-x}\text{Se}_2$ was confirmed. The origin of this superstructure was nevertheless unknown, thus synchrotron single crystal X-ray diffraction measurements were performed. No superstructure reflections were observed, which indicates that the $\sqrt{2}a \times \sqrt{2}a$ superstructure observed in electron diffraction measurements originates rather from charge ordering. In contrast, weak diffuse scattering contributions appeared along *l*, thus along the stacking direction. By empirical evaluation of the diffraction data, a stacking disorder was revealed where the stacking transition probability of two identical layers FeSe

respectively $(\text{Li}_{0.8}\text{Fe}_{0.2})\text{OH}$ is unequal zero. However, it is improbable that the impact of these diffuse scattering contributions is the reason for the elongated displacement ellipsoid. Based on these results a split-atom approximation where lithium is shifted off the center of the oxygen tetrahedron in order to shorten the Li–O distance is the favorite real structure model.

Crystal growing of large $[(\text{Li}_{0.8}\text{Fe}_{0.2})\text{OH}]\text{FeSe}$ crystals

Hydrothermal ion-exchange synthesis was employed for the preparation of $[(\text{Li}_{0.8}\text{Fe}_{0.2})\text{OH}]\text{FeSe}$ crystals with an edge length of up to 8 mm. Superconducting as well as non-superconducting $\text{K}_x\text{Fe}_{2-y}\text{Se}_2$ crystals were prepared as precursor crystals via solid-state reaction. The existing crystal lattice served as template for the desired product, whereby the K^+ ions were replaced by layers of $[(\text{Li}_{0.8}\text{Fe}_{0.2})\text{OH}]^{0.2+}$.

The presence respectively absence of superconductivity, correlated with the microstructure in the precursor crystals was of no distinct importance for the properties of the resulting $[(\text{Li}_{0.8}\text{Fe}_{0.2})\text{OH}]\text{FeSe}$ crystals. Obviously, the vacancies in the iron-selenide layer of $\text{K}_x\text{Fe}_{2-y}\text{Se}_2$ are filled during the hydrothermal reaction. Hydrothermal ion-exchange reaction times longer than 3 days were detrimental to superconductivity and led to a continuous decrease of T_c .

The obtained crystals $[(\text{Li}_{0.8}\text{Fe}_{0.2})\text{OH}]\text{FeSe}$ are bulk superconducting with a T_c of about 41 K and thus applicable for future physical measurements like ARPES or orientation dependent μSR measurements.

$[(\text{Li}_{0.8}\text{Fe}_{0.2})\text{OH}]\text{FeS}$ and the ferromagnetic superconductors $[(\text{Li}_{0.8}\text{Fe}_{0.2})\text{OH}]\text{Fe}(\text{S}_{1-x}\text{Se}_x)$

$[(\text{Li}_{0.8}\text{Fe}_{0.2})\text{OH}]\text{FeS}$ and the series $[(\text{Li}_{0.8}\text{Fe}_{0.2})\text{OH}]\text{Fe}(\text{S}_{1-x}\text{Se}_x)$ were synthesized by hydrothermal method and characterized by X-ray single crystal and powder diffraction, EDX and chemical analysis as well as magnetic and resistivity measurements.

Selenium-rich compounds show coexistence of magnetic ordering with superconductivity as known from the pure selenium compound. Sulfur doping decreases the critical temperature until superconductivity is completely absent in $[(\text{Li}_{0.8}\text{Fe}_{0.2})\text{OH}]\text{FeS}$, while ferromagnetism persists in the $(\text{Li}_{0.8}\text{Fe}_{0.2})\text{OH}$ layers. The ferromagnetic ordering shows a very narrow hysteresis typical for a soft ferromagnet. This small coupling might be ascribed to the dilution of the magnetic iron ions in the hydroxide layer.

The Li:Fe ratio in the hydroxide layer and thus the charge transfer of 0.2 electrons from the hydroxide to the iron chalcogenide layers remains unchanged in $[(\text{Li}_{0.8}\text{Fe}_{0.2})\text{OH}]\text{Fe}(\text{S}_{1-x}\text{Se}_x)$, which indicates that the chemical pressure effect of the smaller sulfide ions impedes superconductivity in $[(\text{Li}_{0.8}\text{Fe}_{0.2})\text{OH}]\text{FeS}$. Apparently, for the present system the geometry of the tetrahedral $\text{Fe}(\text{S}_{1-x}\text{Se}_x)$ layer is not further optimized by sulfur doping in contrast to binary $\text{Fe}(\text{S}_{1-z}\text{Se}_z)$ where chemical pressure enhances superconductivity.

Effect of cobalt substitution in the ferromagnetic superconductor

$[(\text{Li}_{0.8}\text{Fe}_{0.2})\text{OH}]\text{FeSe}$

Experimental results of cobalt incorporation in the ferromagnetic superconductor $[(\text{Li}_{0.8}\text{Fe}_{0.2})\text{OH}]\text{FeSe}$ is reported. A recent density functional study predicted a positive effect on superconductivity for a substitution of iron by cobalt in the hydroxide layer, i.e. the hypothetical $[(\text{Li}_{0.8}\text{Co}_{0.2})\text{OH}]\text{FeSe}$. In order to favor a specific substitution of iron by cobalt only in the hydroxide and not in the selenide layer, a directed synthesis strategy was applied where pre-synthesized $\beta\text{-FeSe}$ was used as starting material.

In contrast to the theoretical predictions, magnetic susceptibility measurements revealed that superconductivity in $[(\text{Li}_{0.8}\text{Fe}_{0.2})\text{OH}]\text{FeSe}$ is suppressed by cobalt substitution whereas the ferromagnetic ordering below $T_c = 10$ K persists. X-ray powder diffraction data confirmed the structure model of $[(\text{Li}_{0.8}\text{Fe}_{0.2})\text{OH}]\text{FeSe}$ and EDX measurements the amount of cobalt within the latter. ^{57}Fe -Mössbauer spectroscopy revealed that despite the directed synthesis strategy, cobalt is incorporated in both, the hydroxide and the selenide layers. The latter probably suppresses superconductivity similar to $\text{Fe}_{1-x}\text{Co}_x\text{Se}$.

Hydrothermal synthesis of $\text{Na}_6(\text{H}_2\text{O})_{18}\text{Fe}_4\text{Se}_8$ and $A_2\text{Fe}_4\text{Se}_6$ ($A = \text{K}, \text{Rb}, \text{Cs}$)

By variation of the alkaline metal hydroxide in the hydrothermal synthesis of $[(\text{Li}_{0.8}\text{Fe}_{0.2})\text{OH}]\text{FeSe}$, the iron selenides $A_2\text{Fe}_4\text{Se}_6$ ($A = \text{K}, \text{Rb}, \text{Cs}$) were prepared. The compounds are known in literature and consist of double chains of $[\text{Fe}_2\text{Se}_3]^{1-}$, formed by edge-sharing FeSe_4 tetrahedra. Alkaline metal cations occupy the channels. The hydrothermal synthesis of these iron selenides extends the spectrum of compounds accessible via this method and illustrates the potential of this synthesis strategy with respect to iron chalcogenide compounds.

For a replacement of lithium hydroxide by sodium hydroxide in the synthesis, the new compound $\text{Na}_6(\text{H}_2\text{O})_{18}\text{Fe}_4\text{Se}_8$ was obtained. It was characterized by single crystal and powder X-ray diffraction, EDX, ICP and elementary analysis, Mössbauer and Raman spectroscopy as well as magnetic measurements. The compound consists of $[\text{Fe}_4\text{Se}_8]^{6-}$ ‘stella

quadrangula' clusters of edge-sharing FeSe_4 tetrahedra which are embedded in a three-dimensional $[\text{Na}_6(\text{H}_2\text{O})_{18}]^{6+}$ network. Mössbauer and magnetic measurements indicate that the magnetic ordering of the iron-selenide clusters is analogous to the one observed in protein-bound $[\text{Fe}_4\text{S}_4]^{2+}(\text{S}_{\text{cys}})_4$ clusters. It seems that two intervalent $\text{Fe}^{2.5+}-\text{Fe}^{2.5+}$ pairs with parallel spin show antiparallel coupling. The clusters in $\text{Na}_6(\text{H}_2\text{O})_{18}\text{Fe}_4\text{Se}_8$ are coordinated only via hydrogen bonds to the H_2O ligands of the $[\text{Na}_6(\text{H}_2\text{O})_{18}]^{6+}$ network, thus the isolated clusters might be easily obtained by solving the compound in an appropriate solvent.

7 Conclusion

This thesis provides a new preparative approach to iron-chalcogenide based superconductors. The hydrothermal synthesis of *anti*-PbO type FeSe, which can be seen as basis structure of the compounds of interest was successfully developed. Along with this, some insights regarding the influence of synthesis parameters were gained featuring a basis for further hydrothermal syntheses of new iron-chalcogenide compounds.

The potential of this method, primarily the extension of the so far limited accessibility of iron-chalcogenide based superconductors by solid-state sythesis, was revealed within the present work. The solid-solution $\text{FeSe}_{1-x}\text{S}_x$ was prepared for the whole substitution range, whereas solid-state synthesis exhibits a solubility limit at $x = 0.3$. Furthermore, the new compounds $[(\text{Li}_{0.8}\text{Fe}_{0.2})\text{OH}]\text{FeX}$ ($X = \text{Se}, \text{S}$) were synthesized which are exclusively accessible via hydrothermal method. The compounds, where layers of $(\text{Li}_{0.8}\text{Fe}_{0.2})\text{OH}$ alternate with FeX layers, feature exceptional physical properties, notably a coexistence of superconductivity and ferromagnetism. They were intensively studied within this work. By combination of solid-state and hydrothermal ion-exchange synthesis even large crystals necessary for subsequent physical measurements are accessible.

Apart from these layered iron-chalcogenide superconductors, further compounds which likewise exhibit building blocks of edge-sharing FeSe_4 tetrahedra were found via this synthesis method. The iron selenides $\text{A}_2\text{Fe}_4\text{Se}_6$ ($A = \text{K}, \text{Rb}, \text{Cs}$) consist of double chains of $[\text{Fe}_2\text{Se}_3]^{1-}$, whereas a new compound $\text{Na}_6(\text{H}_2\text{O})_{18}\text{Fe}_4\text{Se}_8$ exhibits $[\text{Fe}_4\text{Se}_8]^{6-}$ ‘stella quadrangula’ clusters.

This structural diversity as well as the associated physical properties of the compounds demonstrates the numerous capabilities of hydrothermal synthesis in the field of iron-chalcogenide compounds. In particular with regard to iron-chalcogenide based superconductors this synthesis strategy is encouraging. It seems probable that the insertion of appropriate layers in between the FeSe layers via hydrothermal reaction will lead to the final breakthrough in the field of iron-based superconductors.

8 Appendix

8.1 Crystallographic data of FeS

Tab. 1: Crystallographic data of FeS.

| FeS | | | | | | | |
|-----------------------------------------------------------------------|----------|------------------------------|-----|----------|-----------------|-----------------|-----------------|
| Formula | | FeS | | | | | |
| Formula weight /g mol ⁻¹ | | 87.9 | | | | | |
| Crystal system | | Tetragonal | | | | | |
| Space group | | P4/nmm O2 (No. 129) | | | | | |
| a, c /pm | | 368.06(3), 502.83(7) | | | | | |
| V /nm ³ | | 0.06812(1) | | | | | |
| Z | | 2 | | | | | |
| d _{calc} /g cm ⁻³ | | 4.29 | | | | | |
| μ (Mo-K _α) /mm ⁻¹ | | 11.809 | | | | | |
| Crystal size /μm ³ | | 20 × 20 × 2 | | | | | |
| Temperature /K | | 293 | | | | | |
| Radiation /pm | | Mo-K _α λ = 71.073 | | | | | |
| θ range /deg. | | 4.1–30.3 | | | | | |
| hkl range | | −4 → +5; −5 → +4; −7 → +7 | | | | | |
| Tot., uniq. data, R _{int} | | 1248, 81, 0.108 | | | | | |
| N _{Refl} , N _{Par} | | 81, 6 | | | | | |
| R ₁ , wR ₂ , S | | 0.0805, 0.0903, 1.99 | | | | | |
| Δρ _{min} , Δρ _{max} /e ⁻ Å ⁻³ | | −3.79, +3.92 | | | | | |
| Atomic positions and displacement parameters | | | | | | | |
| Atom | Wyck. | x | y | z | U ₁₁ | U ₂₂ | U ₃₃ |
| Fe | 2a | 0 | 0 | 0 | 0.0062(8) | 0.0062(8) | 0.014(1) |
| S | 2c | 0 | 1/2 | 0.255(1) | 0.009(1) | 0.009(1) | 0.011(2) |
| Selected bond lengths (/pm) and angles (/deg) | | | | | | | |
| Fe–Fe | 260.3(1) | | | S–Fe–S | 110.3(1) ×2 | 109.1(1) ×4 | |
| Fe–S | 224.3(1) | | | | | | |

8.2 Supplementary information of $[(\text{Li}_{0.8}\text{Fe}_{0.2})\text{OH}]\text{FeSe}$

8.2.1 Crystallographic data of $[(\text{Li}_{0.8}\text{Fe}_{0.2})\text{OH}]\text{FeSe}$

Tab. 1: Crystallographic data of $[(\text{Li}_{0.8}\text{Fe}_{0.2})\text{OH}]\text{FeSe}$.

| [(Li _{0.8} Fe _{0.2})OH]FeSe | | | | | | | | |
|-----------------------------------------------------------------------|-------------------------------------------------------------------------------|-----|--------------|-----------|------------|-----------------|------------------------|-----------------|
| Formula | [(Li _{0.795(5)} Fe _{0.205(5)})OH]Fe _{0.922(3)} Se | | | | | | | |
| Formula weight /g mol ⁻¹ | 164.5 | | | | | | | |
| Crystal system | Tetragonal | | | | | | | |
| Space group | P4/nmm O1 (No. 129) | | | | | | | |
| a, c /pm | 380.38(1), 922.10(6) | | | | | | | |
| V /nm ³ | 0.13342(1) | | | | | | | |
| Z | 2 | | | | | | | |
| d _{calc} /g cm ⁻³ | 4.09 | | | | | | | |
| μ (Mo-Kα) /mm ⁻¹ | 19.61 | | | | | | | |
| Crystal size /μm ³ | 50 × 40 × 5 | | | | | | | |
| Temperature /K | 293 | | | | | | | |
| Radiation /pm | Mo-K _α λ = 71.073 | | | | | | | |
| θ range /deg. | 2.21–33.1 | | | | | | | |
| hkl range | −5 → +5; −5 → +5; −10 → +14 | | | | | | | |
| Tot., uniq. data, R _{int} | 1611, 189, 0.0267 | | | | | | | |
| N _{Refl} , N _{Par} | 189, 15 | | | | | | | |
| R ₁ , wR ₂ , S | 0.0161, 0.0431, 1.35 | | | | | | | |
| Δρ _{min} , Δρ _{max} /e [−] Å ^{−3} | −0.58, +0.44 | | | | | | | |
| Atomic positions and displacement parameters | | | | | | | | |
| Atom | Wyck. | x | y | z | occ. | U ₁₁ | U ₂₂ | U ₃₃ |
| Li | 4f | 0 | 0 | 0.043(6) | 0.795(5) | 0.016(1) | 0.016(1) | 0.061(8) |
| Fe ^a | 2a | 0 | 0 | 0 | 0.205(5) | 0.016(1) | 0.016(1) | 0.061(8) |
| O | 2c | 0 | 1/2 | 0.0716(4) | 1.0 | 0.016(1) | 0.016(1) | 0.027(2) |
| H | 2c | 0 | 1/2 | 0.152(6) | 1.0 | | U _{eq} = 0.02 | |
| Fe ^b | 2b | 0 | 0 | 1/2 | 0.922(3) | 0.0120(3) | 0.0120(3) | 0.0213(3) |
| Se | 2c | 1/2 | 0 | 0.3387(1) | 1.0 | 0.0146(1) | 0.0146(1) | 0.0168(2) |
| Selected bond lengths (/pm) and angles (/deg) | | | | | | | | |
| Li–O | 192.0(7) ×2 | | 218(2) ×2 | | | | | |
| Fe ^a –O | 201.3(1) ×4 | | | | | | | |
| Fe ^b –Se | 241.42(2) ×4 | | | | | | | |
| O–Li–O | 164(1) | | 121(1) | | 93.8(1) ×4 | | | |
| O–Fe ^a –O | 141.7(1) ×2 | | 96.2(1) ×4 | | | | | |
| Se–Fe ^b –Se | 103.96(1) ×2 | | 112.30(1) ×4 | | | | | |

8.2.2 Mössbauer spectroscopy

^{57}Fe -Mössbauer spectroscopy was performed with a standard Wissel setup in transmission geometry using a Co/Rh source with an experimental line width (HWHM) $\omega_{\text{exp}} = 0.13$ mm/s. Spectra were recorded in a warming series and analyzed using a static Hamiltonian approach

$$H_s = \frac{eQ_{zz}V_{zz}}{4I(2I-1)}[(3I_z^2 - I^2)] - g_I\mu_N B \left(\frac{I_+ e^{-i\Phi} + I_- e^{+i\Phi}}{2} \sin \Theta + I_z \cos \Theta \right)$$

setting the field gradient asymmetry to zero. The a- and b-site alone do not sufficiently reproduce the asymmetry of the main b-doublet. Rather appear 20 % of the b-site to have different hyperfine parameters, thus enlarging the left peak. These 20 % perfectly coincide with a 7 % Fe/Li mixing or iron vacancies, which leads to around 20 % disturbed iron surroundings considering randomly distributed Li respectively vacancies in a binomial distribution. However a full distribution of field gradients would be the correct physical interpretation, especially with regard on the bigger line width of the b-doublet compared to the a-doublet in the paramagnetic state. A different interpretation of the missing asymmetry is a texture effect, which could account for a more pronounced left peak in both subspectra, caused by the flaky shape of the crystallites. The absolute value of quadrupole splitting of 0.41 mm/s is relatively large compared to the 0.29 mm/s for the pure FeSe^[1], which might be easily explained by the additional interlayer and the orientation of the principal axis in *c*-direction. The quadrupole splitting of 1.41 mm/s of the a-site was fitted globally.

The Fe^b site does not contain magnetic hyperfine field contribution whereas Fe^a needs a real magnetic splitting to sufficiently describe the subspectrum in the ferromagnetic regime additionally to the huge line broadening. The temperature dependencies of the principal component V_{zz} of the field gradient and the line widths ω are shown in Fig. S1. They indicate experimentally the transition temperatures of the superconductivity and the ferromagnetism, although these parameters are correlated, i.e. they partially compensate each other.

Both, the quadratic Doppler effect and Debye Waller factor do not show any anomaly and can roughly be fitted simultaneously in a Debye approximation with a Debye temperature of 192 K.

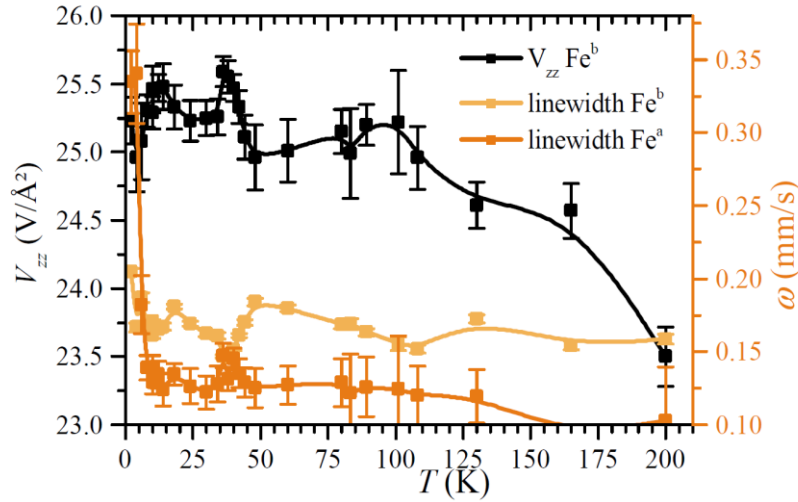


Fig. S1: The changes of the b-doublet shape indicate the superconducting transition at 40 K. While the ferromagnetism at the Fe^a leads to a huge line broadening and a hyperfine field of ≈ 3 T, the doublet of the Fe^b in the FeSe layer only slightly broadens.

- [1] A. Błachowski, K. Ruebenbauer, J. Żukrowski, J. Przewoźnik, K. Wojciechowski, Z. M. Stadnik, *Journal of Alloys and Compounds* **2010**, 494, 1-4.

8.2.3 μ SR

μ SR experiments were carried out at the GPS spectrometer at the π M3.2 beamline of the Swiss Muon Source at the Paul Scherrer Institut. Zero field (ZF) time spectra (Fig. S2) reveal an almost 100 % magnetic fraction at base temperature with regard on the 1/3-tail of the lowest temperature spectrum.

The asymmetry $A(t)$ in the whole temperature range was fitted using the following two fraction model.

$$\frac{A_{ZF}(t)}{A_0} = f_{fm} \left(\frac{2}{3} e^{\lambda_T t} + \frac{1}{3} e^{\lambda_L t} \right) + (1 - f_{fm}) \left[\frac{2}{3} (1 - \sigma_{LGKT}^2 t^2 - \lambda t) e^{-\sigma_{LGKT}^2 t^2 / 2 - \lambda t} + \frac{1}{3} \right]$$

The parameter λ was fixed to the 100 K value, whereas σ_{LGKT} represents the damping due to static stray fields, which was presented in the main text. The transverse damping rate of the magnetic fraction ranges between 6 and 10 μs^{-1} , peaking at 5 K, whereas the longitudinal rate λ_L stays almost close to zero except some barely significant increase at 10 K.

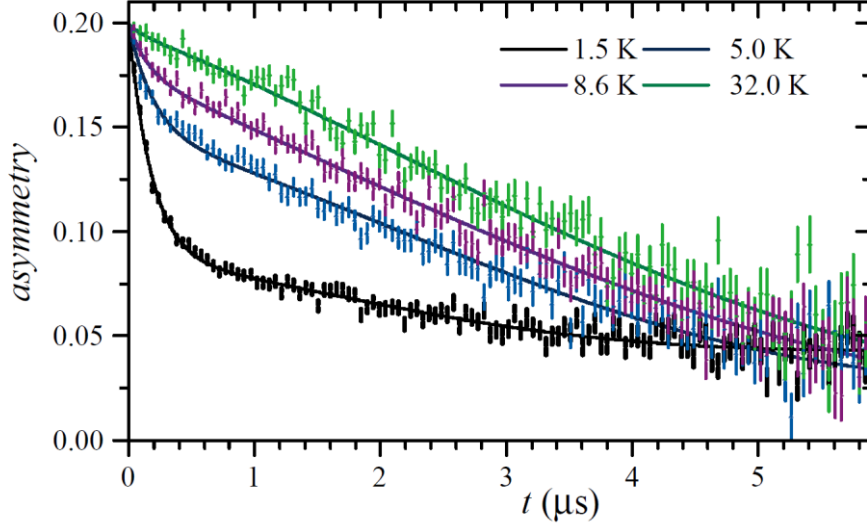


Fig. S2: The virtual constant 1/3-tail of the 1.5 K spectrum reveals almost 100 % magnetic fraction. The nonmagnetic fraction is considerably influenced by stray fields.

Transverse field (TF) experiments were done to deduce superconducting volume fractions and order parameters. Usually the superconducting order parameter is deduced from the Gaussian damping rate of the precession signal. As a matter of fact the signal at 1.5 K is damped exponentially due to ferromagnetism, but there is some considerable Gaussian fraction at temperatures between 10 K and 40 K. The change of damping behavior can be displayed by a stretched exponential fit, however this is not physically reasonable. A three fraction (ferromagnetic, superconducting, paramagnetic) fit only works with fixed ferromagnetic fractions f_{fm} from the zero field analysis:

$$\begin{aligned} \frac{A_{TF}(t)}{A_0} = & f_{fm,ZF} \cos(\gamma(B_{ex} + dB_{fm})t + \phi_0) e^{-\lambda_{FM}t} \\ & + f_{SC} \cos(\gamma(B_{ex} + dB_{SC})t + \phi_0) e^{-\sigma_{SC}^2 t^2/2} \\ & + (1 - f_{fm} - f_{SC}) \cos(\gamma B_{ex}t + \phi_0) e^{-\lambda_{pm}t} \end{aligned}$$

The ferromagnetic damping λ_{FM} stays almost constant at $\approx 7 \mu s^{-1}$, the paramagnetic damping λ_{pm} was fixed to the 45 K value. The damping rate σ_{SC} , which is assigned mainly to superconductivity but might also include additional ferromagnetic damping, increases from 42 K to 27 K from zero to $0.6 \mu s^{-1}$. As the ferromagnetic and superconducting fractions are not clearly distinguishable by these TF measurements we resign to interpret the superconducting order parameter.

In Fig. S3 the temperature dependence of the volume fractions is shown. A superconducting volume fraction of 40 % maximum can be deduced from this 200 G-TF data. Additional 700 G measurements were even worse to analyse.

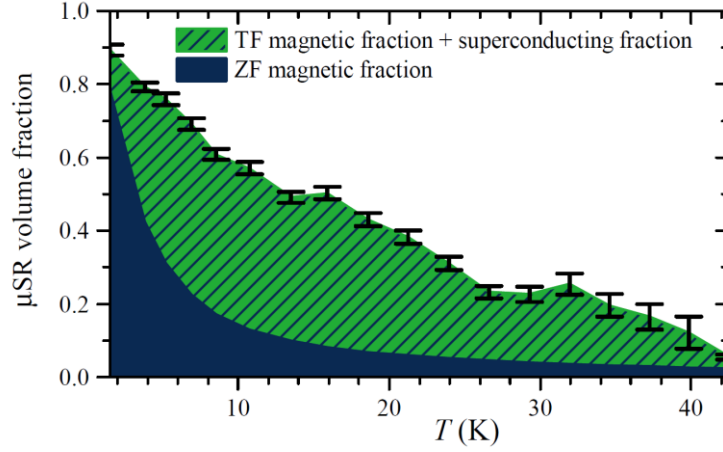


Fig. S3: Transverse field data was analyzed using a ferromagnetic fraction fixed to ZF data. The residual signal can be described by a Gaussian damping, which might include aside superconducting origin also ferromagnetic contributions. However the pinning experiment (Fig. S4) at 15 K proves this fraction indeed to be of superconducting origin.

As the situation from TF measurements was not clear we decided to perform pinning experiments. Field cooling the sample at 200 G starting from temperatures above 45 K should lead to a well established flux line lattice in the superconducting parts of the sample, which in case of sufficient amount and strength of pinning centers, should be kept in the superconducting state when the field is reduced. This indeed is the case for $\approx 40\%$ of the signal at 15 K (Fig. S4), in agreement with the TF data.

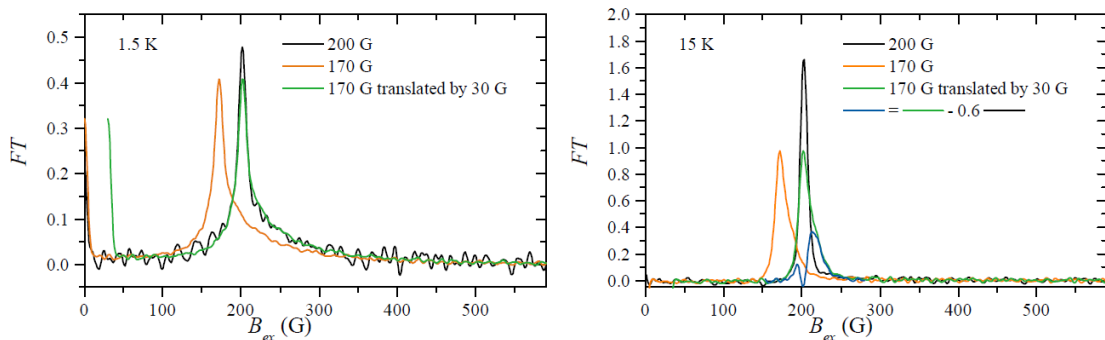


Fig. S4: The Fourier transformation FT of the time spectra of the μ SR pinning experiments prove bulk superconductivity above the Curie temperature at 15 K (right). In contrast at 1.5 K (left) pinning is absent, thus the complete suppression of superconductivity by ferromagnetism is probable.

In contrast, the pinning fails at 1.5 K. Most probably, the superconductivity is then suppressed by the ferromagnetism.

8.3 Crystallographic data of $[(\text{Li}_{0.8}\text{Fe}_{0.2})\text{OH}]\text{FeS}$

Tab. 1: Crystallographic data of $[(\text{Li}_{0.8}\text{Fe}_{0.2})\text{OH}]\text{FeS}$.

| [(Li _{0.8} Fe _{0.2})OH]FeS | | | | | | | | |
|----------------------------------------------------------|--------------|---------------------------------------------------------|--------------|-----------|------------|-----------------|------------------------|-----------------|
| Formula | | [(Li _{0.828(5)} Fe _{0.172(5)})OH]FeS | | | | | | |
| Formula weight /g mol ⁻¹ | | 120.3 | | | | | | |
| Crystal system | | Tetragonal | | | | | | |
| Space group | | P4/nmm 01 (No. 129) | | | | | | |
| a, c /pm | | 370.38(2), 888.5(1) | | | | | | |
| V /nm ³ | | 0.12189(1) | | | | | | |
| Z | | 2 | | | | | | |
| d _{calc} /g cm ⁻³ | | 3.28 | | | | | | |
| μ (Mo-K _α) /mm ⁻¹ | | 7.642 | | | | | | |
| Crystal size /μm ³ | | 30 × 20 × 5 | | | | | | |
| Temperature /K | | 293 | | | | | | |
| Radiation /pm | | Mo-K _α λ = 71.073 | | | | | | |
| θ range /deg. | | 4.6–30.4 | | | | | | |
| hkl range | | -4 → +5; -4 → +5; -11 → +12 | | | | | | |
| Tot., uniq. data, R _{int} | | 1694, 143, 0.0522 | | | | | | |
| N _{Refl} , N _{Par} | | 143, 15 | | | | | | |
| R ₁ , wR ₂ , S | | 0.0336, 0.0444, 1.21 | | | | | | |
| Δρ _{min} , Δρ _{max} /e-Å ⁻³ | | -0.50, +0.80 | | | | | | |
| Atomic positions and displacement parameters | | | | | | | | |
| Atom | Wyck. | x | y | z | occ. | U ₁₁ | U ₂₂ | U ₃₃ |
| Li | 4f | 0 | 0 | 0.061(6) | 0.828(5) | 0.023(7) | 0.023(7) | 0.08(1) |
| Fe ^a | 2a | 0 | 0 | 0 | 0.172(5) | 0.023 (7) | 0.023(7) | 0.08(1) |
| O | 2c | 0 | 1/2 | 0.0798(6) | 1.0 | 0.019(1) | 0.019(1) | 0.033(3) |
| H | 2c | 0 | 1/2 | 0.0160(9) | 1.0 | | U _{eq} = 0.02 | |
| Fe | 2b | 0 | 0 | 1/2 | 1.0 | 0.0053(2) | 0.0053(2) | 0.0238(5) |
| S | 2c | 1/2 | 0 | 0.3546(1) | 1.0 | 0.0082(4) | 0.0082(4) | 0.0194(7) |
| Selected bond lengths (/pm) and angles (/deg) | | | | | | | | |
| Li–O | 185.9(4) ×2 | | 223(3) ×2 | | | | | |
| Fe ^a –O | 198.3(1) ×4 | | | | | | | |
| Fe–S | 225.79(9) ×4 | | | | | | | |
| O–Li–O | 170(1) | | 112(1) | | 92.8(1) ×4 | | | |
| O–Fe ^a –O | 138.1(1) ×2 | | 97.3(1) ×4 | | | | | |
| S–Fe–S | 110.20(1) ×2 | | 109.11(1) ×4 | | | | | |

9 Abbreviations

| | |
|--------------------|---------------------------------------------------|
| $^{\circ}\text{C}$ | degree centigrade |
| 2G-HTS | second-generation high-temperature superconductor |
| $4\pi\chi_v$ | magnetic (e.g. superconducting) volume fraction |
| A | alkaline metal |
| $A(t)$ | asymmetry |
| a^*, b^*, c^* | reciprocal unit cell axes |
| a, b, c | unit cell axes |
| arb. units | arbitrary units |
| AC | alternating current |
| ARPES | angle resolved photoelectron spectroscopy |
| B | magnetic flux density |
| BCS | Bardeen-Cooper-Schrieffer |
| d | distance |
| DC | direct current |
| deg | degree |
| DFT | density functional theory |
| DOS | density of states |
| e^- | electron |
| EDX | energy dispersive X-ray spectroscopy |
| EELS | electron energy loss spectroscopy |
| E_F | Fermi energy |
| ESRF | European Synchrotron Radiation Facility |
| <i>et al.</i> | <i>et alii</i> (and others) |
| fc | field cooling |
| Fig. | figure |
| FT | Fourier transformation |
| GGA | generalized-gradient approximation |
| GL | Ginzburg-Landau |

| | |
|-------------|-----------------------------------------------------------|
| H | magnetic field |
| $h\ k\ l$ | Miller indices |
| H_c | critical field |
| HWHM | half width at half maximum |
| I | intensity |
| ICP-AAS | inductively coupled plasma atomic absorption spectroscopy |
| K | Kelvin |
| mol | mole |
| MSD | mean square displacements |
| N | shape-dependent demagnetizing factor |
| NMR | nuclear magnetic resonance |
| NN | nearest-neighboring |
| <i>occ.</i> | occupation |
| Oe | Oersted |
| P | probability |
| PAW | projector-augmented waves |
| ppm | parts per million |
| PSI | Paul Scherrer Institut |
| PTFE | polytetrafluoroethylene |
| PXRD | X-ray powder diffraction |
| r | radius |
| R | resistance |
| $R...$ | residual factor |
| RE | rare earth element |
| Ref. | reference |
| S | goodness of fit |
| SEM | scanning electron microscopy |
| SQUID | superconducting quantum interference device |
| T | temperature |
| T | tesla |
| t | reduced temperature |

| | |
|-------------------------|---------------------------------------------|
| Tab. | table |
| T_c | critical temperature of a superconductor |
| T_C | Curie temperature |
| TEM | transmission electron microscopy |
| TF | transverse field |
| U_{eq} | equivalent thermal displacement parameter |
| U_{ij} | anisotropic thermal displacement parameter |
| v | velocity |
| VASP | Vienna ab-initio simulation package |
| Vol | volume |
| V_{zz} | principal component of the field gradient |
| WHH | Werthamer-Helfand-Hohenberg |
| WMI | Walther-Meißner-Institut |
| $wR...$ | weighted residual factor |
| wt% | weight percent |
| Wyck. | Wyckoff position |
| X | Se, S |
| Z | number for empirical formulas per unit cell |
| Z | set of integers |
| ZF | zero field |
| zfc | zero field cooling |
| α, β, γ | unit cell angles |
| δ | isomer shift |
| $\Delta\rho$ | residual electron density |
| θ | diffraction angle |
| λ | wave length |
| μ | absorption coefficient |
| μ_B | Bohr magneton |
| μ_{eff} | effective magnetic moment in Bohr magnetons |
| μSR | muon spin rotation |
| ξ | coherence length |

| | |
|------------------------|-----------------------------------------------------------------------|
| ρ | electrical resistivity |
| σ_{LGKT} | static relaxation rate fitted with Lorentz-Gauss Kubo-Toyabe function |
| Φ_0 | flux quanta |
| χ | magnetic susceptibility |
| ω | line width |

10 Scientific contributions

10.1 Publications

Publications within this thesis

1 Coexistence of 3d-ferromagnetism and superconductivity in $[(\text{Li}_{0.8}\text{Fe}_{0.2})\text{OH}]\text{FeSe}$

U. Pachmayr, F. Nitsche, H. Luetkens, S. Kamusella, F. Brückner, R. Sarkar, H.-H. Klauss, and D. Johrendt

Angewandte Chemie International Edition **2015**, 54, 293.

For this publication, synthesis and sample preparation of $[(\text{Li}_{0.8}\text{Fe}_{0.2})\text{OH}]\text{FeSe}$, REM-EDX measurements, powder X-ray diffraction, Rietveld refinement and data analysis were performed by Ursula Pachmayr. Single crystal measurements and structure elucidation were done by Fabian Nitsche and Ursula Pachmayr. SQUID and conductivity measurements were performed by Simon Peschke, Gina Friederichs and Roman Pobel. ICP-AAS measurements were performed by Jaroslava Obel and combustion analysis (CHNS) by Bernhard Kempf. ^{57}Fe -Mössbauer studies were performed and evaluated by Sirko Kamusella and Hans-Henning Klauss (TU Dresden). Muon spin rotation spectroscopy measurements as well as data analysis and interpretation were done by Hubertus Luetkens at the Paul Scherrer Institute in Switzerland. Sirko Kamusella contributed to data analysis and discussion. ^7Li -NMR spectra were recorded and interpreted by Felix Brückner and Rajib Sarkar (TU Dresden). DFT calculations were performed by Dirk Johrendt. The manuscript was written by Dirk Johrendt in association with Ursula Pachmayr, Hubertus Luetkens, Sirko Kamusella, Rajib Sarkar and Hans-Henning Klauss.

2 $[(\text{Li}_{0.8}\text{Fe}_{0.2})\text{OH}]\text{FeS}$ and the ferromagnetic superconductors $[(\text{Li}_{0.8}\text{Fe}_{0.2})\text{OH}]\text{Fe}(\text{S}_{1-x}\text{Se}_x)$

U. Pachmayr and D. Johrendt

Chemical Communications **2015**, 51, 4689.

The syntheses of $[(\text{Li}_{0.8}\text{Fe}_{0.2})\text{OH}]\text{Fe}(\text{S}_{1-x}\text{Se}_x)$ with $0 \leq x \leq 1$, powder X-ray diffraction, Rietveld refinement, REM-EDX measurements, AC-susceptibility measurements, single crystal measurement and structure elucidation, sample preparation, data analysis, literature screening, writing the manuscript main part and picture editing were done by Ursula Pachmayr. SQUID and conductivity measurements were performed by Simon Peschke and Roman Pobel. ICP-AAS measurements were performed by Jaroslava Obel and combustion analysis (CHNS) by Bernhard Kempf. The manuscript was revised by Dirk Johrendt.

3 **Structural transition and superconductivity in hydrothermally synthesized FeX ($X = \text{S}, \text{Se}$)**

U. Pachmayr, N. Fehn, and D. Johrendt

Chemical Communications **2016**, 52, 194.

For this publication, synthesis of FeSe , and with assistance of Natalie Fehn of FeS , literature screening, sample preparation, REM-EDX measurements, powder X-ray diffraction, Rietveld refinement, AC-susceptibility measurements, single crystal measurement and structure elucidation, data analysis, writing the manuscript main part and picture editing were done by Ursula Pachmayr. Measurement of low temperature X-ray powder data was performed by Juliane Stahl and ICP-AAS by Jaroslava Obel. The manuscript was revised by Dirk Johrendt.

4 **Effect of cobalt substitution in the ferromagnetic superconductor $[(\text{Li}_{0.8}\text{Fe}_{0.2})\text{OH}]\text{FeSe}$**

U. Pachmayr, S. Kamusella, H.-H. Klauss, and D. Johrendt

Zeitschrift für anorganische und allgemeine Chemie **2016**, 642, 989.

Synthesis of cobalt substituted $[(\text{Li}_{0.8}\text{Fe}_{0.2})\text{OH}]\text{FeSe}$, powder X-ray diffraction, Rietveld refinement, REM-EDX measurements, sample preparation, data analysis, literature screening, writing the manuscript main part and picture editing were done by Ursula Pachmayr. SQUID measurements were performed by Simon Peschke and Roman Pobel. ^{57}Fe -Mössbauer studies were performed and evaluated by Sirko Kamusella and Hans-Henning Klauss (TU Dresden). The manuscript was revised by Dirk Johrendt.

5 **$\text{Na}_6(\text{H}_2\text{O})_{18}\text{Fe}_4\text{Se}_8$: a new iron-chalcogenide with $[\text{Fe}_4\text{Se}_8]^{6-}$ clusters**

U. Pachmayr, S. Datz, S. Kamusella, H.-H. Klauss, and D. Johrendt

This chapter is in preparation to be published in a scientific journal.

For this publication, synthesis and sample preparation of $\text{Na}_6(\text{H}_2\text{O})_{18}\text{Fe}_4\text{Se}_8$, REM-EDX measurements, single crystal and powder X-ray diffraction measurements and structure elucidation, Rietveld refinement, data analysis, literature screening, writing the manuscript main part and picture editing were performed by Ursula Pachmayr. SQUID measurements were performed by Simon Peschke and Roman Pobel. ICP-AAS measurements were performed by Jaroslava Obel and combustion analysis (CHNS) by Bernhard Kempf. ^{57}Fe -Mössbauer studies were performed and evaluated by Sirko Kamusella and Hans-Henning Klauss (TU Dresden). Raman spectroscopy was performed by Stefan Datz. The manuscript was revised by Dirk Johrendt.

Publications beyond this thesis

6 **Magnetic field modulated microwave spectroscopy of lithiated iron selenide hydroxide $[(\text{Li}_{1-x}\text{Fe}_x)\text{OH}]\text{FeSe}$**

C. Urban, I. Valmianski, U. Pachmayr, A. C. Basaran, D. Johrendt, and I. K. Schuller

This chapter is submitted for publication in a scientific journal.

7 **^{57}Fe Mössbauer spectroscopy on iron based pnictides and chalcogenides in applied magnetic fields**

S. Kamusella, K. T. Lai, L. Harnagea, R. Beck, U. Pachmayr, G. Thakur, and H.-H. Klauss

Physica Status Solidi (B) **2016**, doi: 10.1002/pssb.201600160.

8 **Coexistence of low-moment magnetism and superconductivity in tetragonal FeS and suppression of T_c under pressure**

S. Holenstein, U. Pachmayr, Z. Guguchia, S. Kamusella, R. Khasanov, A. Amato, C. Baines, H.-H. Klauss, E. Morenzoni, D. Johrendt, and H. Luetkens

Physical Review B **2016**, 93, 140506.

9 Short range magnetic order in overdoped $\text{Ba}_{1-x}\text{K}_x\text{Fe}_2\text{As}_2$ ($0 \leq x \leq 0.66$)

E. Wiesenmayer, G. Pascua, F. Hummel, H. Luetkens, Z. Guguchia, A. Binek, U. Pachmayr, T. Hermann, T. Goltz, Z. Shermadini, R. Khasanov, A. Amato, H. Maeter, H.-H. Klauss, and D. Johrendt.

This chapter is in preparation to be published in a scientific journal.

10 Superconductivity in $\text{Ba}_{1-x}\text{K}_x\text{Ti}_2\text{Sb}_2\text{O}$ ($0 \leq x \leq 1$) controlled by charge doping

U. Pachmayr and D. Johrendt

Solid State Sciences **2014**, 28, 31.

11 A functional triazine framework based on N-heterocyclic building blocks

S. Hug, M. E. Tauchert, S. Li, U. Pachmayr, and B. V. Lotsch

Journal of Materials Chemistry **2012**, 22, 13956.

10.2 Conference contributions**1 Effect of Cobalt Substitution in the Ferromagnetic Superconductor $[(\text{Li}_{0.8}\text{Fe}_{0.2})\text{OH}]\text{FeSe}$ (poster)**

U. Pachmayr, S. Kamusella, H.-H. Klauss, and D. Johrendt

18. Vortragstagung GDCh Fachgruppe Festkörperchemie und Materialforschung, Innsbruck, Austria, **2016**.

2 Coexistence of Ferromagnetism and Superconductivity in the Iron Chalcogenide $[(\text{Li}_{0.8}\text{Fe}_{0.2})\text{OH}]\text{FeSe}_{1-x}\text{S}_x$ ($0 \leq x \leq 1$) (poster)

U. Pachmayr, F. Nitsche, H. Luetkens, S. Kamusella, F. Brückner, R. Sarkar, H.-H. Klauss, and D. Johrendt

International workshop on iron-based superconductors, Munich, Germany, **2016**.

3 Hydrothermalsynthese von FeSe_x basierten Verbindungen (talk)

U. Pachmayr and D. Johrendt

Hirschegg-Seminar on solid-state chemistry, Hirschegg, Austria, **2016**.

- 4 **Superconductivity and Crystal Structures in Solvothermally synthesized FeX and [(Li,Fe)OH]FeX (X = Se, S) (invited talk)**
U. Pachmayr, J. Stahl, and D. Johrendt
MRS Spring Meeting & Exhibit, Phoenix, Arizona, **2016**.
- 5 **Über Hydrothermalsynthese zu FeCh (Ch = Se, S) Supraleitern (talk)**
U. Pachmayr and D. Johrendt
Obergurgl-Seminar Festkörperchemie, Obergurgl, Austria, **2016**.
- 6 **Coexistence of Ferromagnetism and Superconductivity in the iron chalcogenide [(Li_{0.8}Fe_{0.2})OH]FeSe (poster)**
U. Pachmayr, F. Nitsche, H. Luetkens, S. Kamusella, F. Brückner, R. Sarkar, H.-H. Klauss, and D. Johrendt
15th European Conference on Solid State Chemistry (ECSSC15), Vienna, Austria, **2015**.
- 7 **“Gegensätze vereint” (talk)**
U. Pachmayr and D. Johrendt
Hirschegg-Seminar on solid-state chemistry, Hirschegg, Austria, **2015**.
- 8 **Supraleitung in Ba_{1-x}K_xTi₂Sb₂O (talk)**
U. Pachmayr and D. Johrendt
Obergurgl-Seminar Festkörperchemie, Obergurgl, Austria, **2014**.

Coauthor contributions

- 9 **Coexistence of low moment magnetism and superconductivity in tetragonal FeS and suppression of T_c under pressure (poster)**
S. Holenstein, U. Pachmayr, Z. Guguchia, S. Kamusella, R. Khasanov, A. Amato, C. Baines, H.-H. Klauss, E. Morenzoni, D. Johrendt, and H. Luetkens
International workshop on iron-based superconductors, Munich, Germany, **2016**.

10 Superconducting properties of ferromagnetic lithiated iron selenide hydroxide (talk)

C. Urban, A. Basaran, U. Pachmayr, D. Johrendt, and I. K. Schuller

MMM Meeting, San Diego, USA, **2016**.

11 Probing the coexistence of superconductivity and ferromagnetism (talk)

C. Urban, A. Basaran, U. Pachmayr, D. Johrendt, and I. K. Schuller

APS March Meeting, San Antonio, USA, **2015**.

12 Optimized synthesis of $\text{Ba}_{1-x}\text{K}_x\text{Fe}_2\text{As}_2$ via mechanical alloying (poster)

E. Wiesenmayer, A. Binek, U. Pachmayr, K. Markovic, M. Dunst, and D. Johrendt

Student workshop, Bad Schandau, Germany, **2013**.

13 New synthetic route and optimized synthesis of $\text{Ba}_{1-x}\text{K}_x\text{Fe}_2\text{As}_2$ (poster)

E. Wiesenmayer, A. Binek, U. Pachmayr, K. Markovic, M. Dunst, and D. Johrendt

EUCAS European Conference on Applied Superconductivity, Genoa, Italy, **2013**.

11 Curriculum Vitae

Personal Details

Full Name: Ursula Elisabeth Pachmayr
Date of Birth: 07.02.1989
Place of Birth: Munich, Germany
Nationality: German

Education

Since 10/2013 Ph.D. thesis in inorganic solid-state chemistry in the group of Prof. Dr. Dirk Johrendt, Department Chemistry at the Ludwig-Maximilians-Universität, München; title of thesis: *Hydrothermal synthesis of layered iron-chalcogenide superconductors and related compounds*

12/2013 Römer-Award (Dr. Klaus Römer-foundation) for master thesis

02/2013 – 08/2013 Master thesis in the group of Prof. Dr. Dirk Johrendt, Department Chemistry at the Ludwig-Maximilians-Universität, München; title of thesis: *Synthesis, structure and properties of layered titanium pnictide oxide superconductors*

10/2011 – 09/2013 Master studies in chemistry at the Ludwig-Maximilians-Universität, München

10/2008 – 08/2011 Bachelor studies in chemistry and biochemistry at the Ludwig-Maximilians-Universität, München

10/2008 – 09/2013 Scholarship holder of the Max Weber-Program, Bayern

06/2008 Allgemeine Hochschulreife at the Karlsgymnasium München-Pasing

09/1999 – 06/2008 Secondary education at the Karlsgymnasium München-Pasing

09/1995 – 07/1999 Primary education at the Grundschule am Schererplatz, München